ABSTRACT

Title of Document:	Laminar Free Convection from a Vertically-Oriented Concentrated Photovoltaic Cell with Uniform Surface Heat Flux
	Jason Connolly, Kevin Fries, Sougata Biswas, Christopher Grant, Kevin Hwang, Hoyoung Kang, Donna Motabar
Directed By:	Dr. Charlie Carr, Maryland Technology Enterprise Institute

This research project uses field measurements to investigate the cooling of a triple-junction, photovoltaic cell under natural convection when subjected to various amounts of insolation. The team built an experimental apparatus consisting of a mirror and Fresnel lens to concentrate light onto a triple-junction photovoltaic cell, mounted vertically on a copper heat sink. Measurements were taken year-round to provide a wide range of ambient conditions. A surface was then generated, in MATLAB, using Sparrow's model for natural convection on a vertical plate under constant heat flux. This surface can be used to find the expected operating temperature of a cell at any location, given the ambient temperature and insolation. This research is an important contribution to the industry because it utilizes field data that represents how a cell would react under normal operation. It also extends the use of a well-known model from a one-sun environment to a multi-sun one.

Laminar Free Convection from a Vertically-Oriented Concentrated Photovoltaic Cell with Uniform Surface Heat Flux

Jason Connolly, Kevin Fries, Sougata Biswas, Christopher Grant, Kevin Hwang, Hoyoung Kang, and Donna Motabar

Mentor: Dr. Charlie Carr

Thesis submitted in partial fulfillment of the requirements of the Gemstone Program, University of Maryland, 2013

Advisory Committee:
Dr. Charlie Carr, University of Maryland, Mentor
Dr. Nibir Dhar, Army Research Laboratory
Dr. Mario Dagenais, University of Maryland
Dr. Victor Yakovenko, University of Maryland
Mr. Brian Dougherty, National Institute of Standards and Technology
Mr. Tao Cao, University of Maryland

Acknowledgements

We would like to thank our mentor, Dr. Carr, for all of his teaching and support; without him whipping us into shape, this project would have never been completed. We would also like to thank our librarian, Nevenka Zdravkovska, for her help with the extensive literature search. We would like to thank the EMCORE Corporation for their generous donation of 20 multi-layer solar cells and ReflecTech for their donation of mirror film. We would like to thank Jes Sheehan, Adam Elbaz, Dr. Bar-Cohen, and the rest of TherPES lab for their help with thermal imaging. Finally, we would like to thank the ACCIAC for their generous grant in support of our research.

Table of Contents

List of Figures

List of Tables

Nomenclature and Symbols

A - Area
c - speed of light
D - effective diffusion constant
E - energy factor
E_{ph}- energy of photon
h - Planck's constant
ħ - reduced Planck's constant
H - height of an object
i - imaginary number
I - solar flux
I_{sc}- short-circuit current
j - projection of electric current density vector onto the direction of the temperature gradient
J - current density
J_0 - dark/recombination current
J_{ph} - photocurrent
k - Boltzmann's constant
k – wave number
L - diffusion length
n - natural numbers
m - mass
P - power
p - momentum
Q - heat
q - charge
q - heat flux
R - Thermal Resistance
r - reflection coefficient
S - Seebeck Coefficient
S - length of a shadow cast by an object
T - Temperature
T_∞ - Ambient Temperature
t - time
U - potential energy
v - velocity
V - voltage
V_{oc}- open-circuit voltage
η - efficiency
λ - wavelength
τ - lifetime
x - position
θ - angle
υ - frequency
ψ-wave function

1 - Introduction

Solar energy is the next great energy source for the world, one that has many challenges but can provide so much energy at such a small environmental cost. According to the United States Energy Information Administration, eight percent of the total energy consumption in the United States in 2010 was from renewable energy sources. Of that eight percent, only one percent is harvested from solar energy sources. Since 1989, the solar energy use has increased from 55 trillion Btu (British thermal units) to 109 trillion Btu. However, this is staggeringly small compared to the 22,077 trillion Btu of energy obtained through coal. Our research aims to help make solar energy more efficient, more cost-effective, and more prevalent in our total energy consumption [1].

Due to the continually rising costs of oil and the need for sustainability, there has been an increase in the research and production of photovoltaic (PV) or solar energy. As can be seen in Figure 1, since the 1970s, efficiency of solar panels has been continually increasing from about one percent, achieved by RCA in 1976, to 43.5 percent, achieved by Solar Junction in 2011. These high efficiency solar cells consist of several layers, each absorbing its own spectrum of light. Several layers allow for the solar cells to absorb more light, which in turn, provides more energy.

Solar research encompasses such fields as concentrated photovoltaic technology (CPV), multi-junction cells, and solar-thermal energy collection. This research is typically done by using flash tests to solely study the electrical performance of the cell and is commonly put into practice at large solar collection farms, where forced cooling is used to keep the operating temperature down. To achieve large amounts of energy on small scale settings, sunlight must be concentrated onto the cell, which in turn, causes the

cell temperature to rise and efficiency to drop. Our project aims to understand this relationship, given different ambient temperatures and insolation, by examining the cooling of a concentrated, vertical, triple-junction cell, on a flat plate, subjected to natural convection.

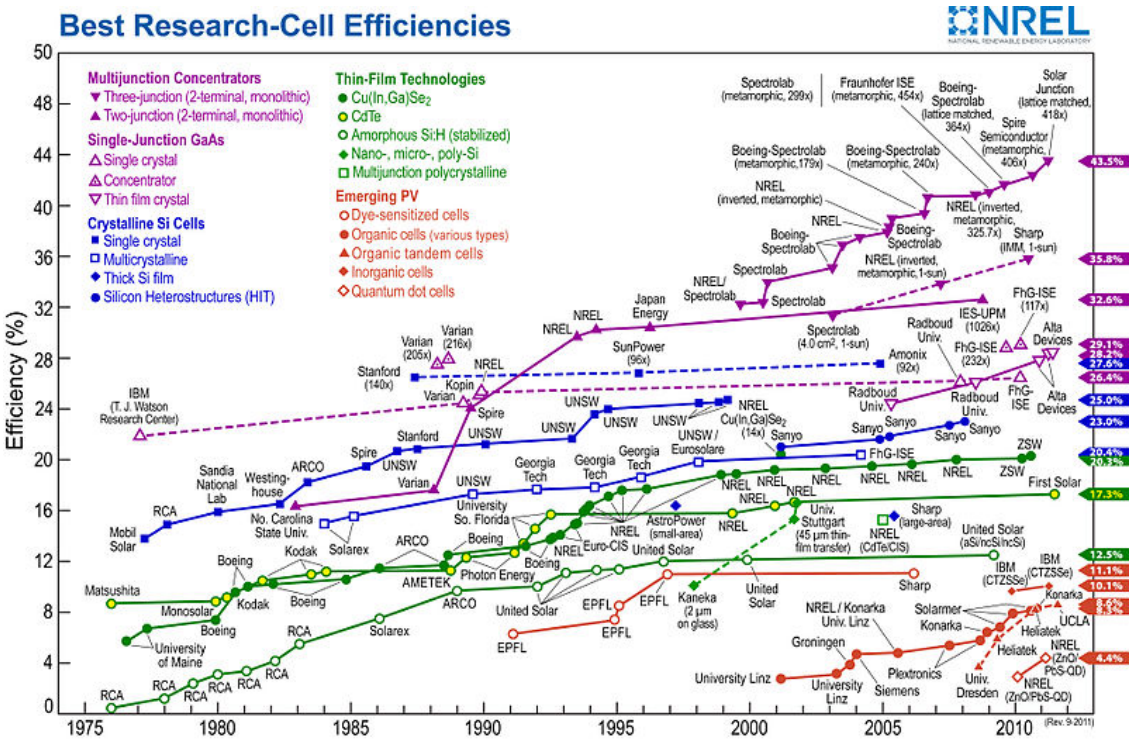

Figure 1. NREL Solar Cell Efficiency Chart [2]

2 - Literature Review

2.1 - Theory of Solar Energy

Earth's ultimate recoverable resource of oil is estimated at 3 trillion barrels and contains $1.7x10^{22}$ joules of energy. This equates to the amount of energy the sun supplies to the Earth in 1.5 days. The sun delivers the amount of energy humans use annually, approximately $4.6x10^{20}$ joules, in one hour. The sun continuously delivers $1.2x10^{5}$ terawatts (TW) to Earth, which dwarfs every other energy source. It exceeds the rate at which humans produce and use energy by 13 TW [3].

Sunlight can be converted into electricity by exciting electrons in a solar cell and into chemical fuel through photosynthesis. Biomass produced by natural photosynthesis is the largest use of solar energy. Its combustion accounts for 11% of human energy needs. But more than two-thirds is gathered unsustainably and burned in small inefficient stoves where combustion is incomplete and the pollutants are uncontrolled [3].

Solar cells, also known as photovoltaic cells, or PV cells, are semiconductor devices that change photons from the sun into a useable electric current. The photovoltaic effect was discovered by Edmund Becquerel in 1839 when he illuminated platinum (Pt) electrodes coated with silver chloride (AgCl) or silver bromide (AgBr) inserted into an acidic solution [4]. The next step in photovoltaic energy occurred in 1876 when William Grylls Adams and Richard Evans Day discovered that when Pt leads were inserted into a selenium (Se) bar, it was possible to start a current merely by the action of light [4]. This discovery eventually led to the creation of the first usable PV device, a thin-film Se solar cell, by Charles Fritts in 1883. The modern silicon (Si) solar cell was discovered in 1954

in Bell Labs by Daryl Chapin, Gerald Pearson, and Calvin Fuller [5]. This solar cell was created using a p-n junction doped with gallium and phosphorous.

A p-n junction is at the center of any semiconductor device. A p-n junction consists of two layers, an n-type layer, commonly called the emitter, and a p-type layer called the acceptor. The n-type layer is often 100 to 300 times thinner than its respective p-type layer. Semiconductor solar cells work by using the energy from the incoming photons to raise the energy level of electrons from the cell's valence band to its conduction band. When the sunlight hits the top layer of the solar cell, its photons can be reflected, absorbed, or transmitted. As the photons enter into the solar cell, they collide with the valence electrons in the silicon lattice structure transferring its energy into one of the electrons. As the energy is transferred, the valence electron gets knocked from its place in the lattice and begins to move through the semiconductor. If the energy of the photon is less than the band gap energy, the electron will recombine with another hole in the lattice structure. If the energy of the photon is greater than the band gap energy, the electron will move to the conduction band and move freely. The band gap energy is the energy difference between the lower edge of the conduction band where the electrons are free to move and the upper edge of the valence band where the electrons are bound to the atom. The holes and electrons in the semiconductor are called carriers and have very short lifetimes and are likely to recombine. If the thickness of the cell is too large, the electrons will have to travel a large distance through the cell and have more chances for recombination. To aid in lowering band gap energies and enabling easier and more efficient conduction, the p- and n-type layers are "doped". These doped layers have ions of boron and phosphorous placed within the silicon lattice structure. In silicon solar cells,

the donors are phosphorous and the acceptors are boron. The doped materials create an electrostatic potential across the cell, particularly in the depletion region near the p-n junction, known as a built-in voltage. This voltage and the depletion region restrict the electrons from moving to the p-type region and the holes from the n-type. Once electrons and holes are gathered at their respective contacts, the electrons begin to move through the connecting wire, creating an electric current. When the electrons reach the rear contact, the electrons recombine with the holes present, thus completing its cycle [6].

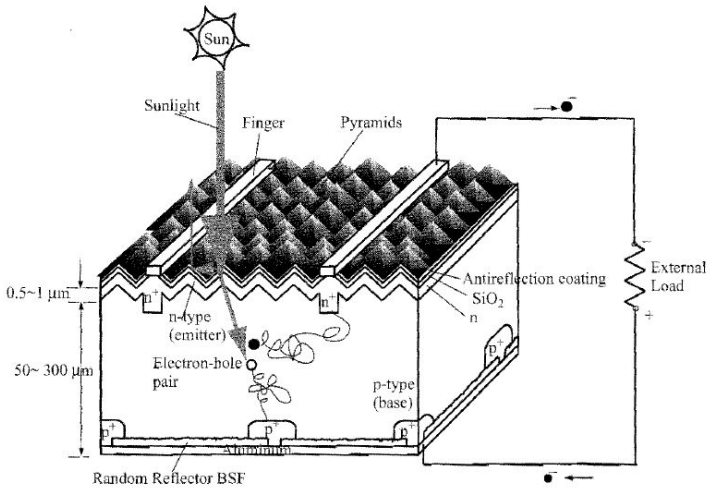

Figure 2. A typical silicon solar cell [6]

Light has a wave-particle dual nature and the incident particles of light are called photons that have no mass but quantized energy. Light not only propagates effectively through a medium or vacuum as a wave form but also behaves as particles or photons once they reach a surface. The phenomenon of light propagation is best described by the electromagnetic wave theory while the interaction of light with matter is best described as a particle phenomenon. Maxwell proved theoretically that the electrical disturbance should propagate in free space with the speed of light which means light waves are electromagnetic waves. An image of light, displaying the oscillating electric (E) and

magnetic (H) fields, perpendicular to each other and to the direction of light, is shown below.

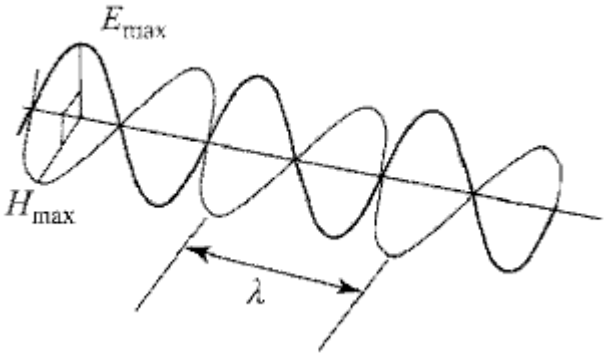

Figure 3. The Electric and Magnetic Fields of Light [6]

Hertz first observed that electrons were emitted when light strikes a metal surface. However, no matter how intense the light shined on the metal surface, if the frequency of the light was below a specific minimum value then no electron was emitted. This was controversial to the classical photoelectric effect that stated the energy associated with electromagnetic radiation depends only on the intensity and not on the frequency. In 1905, Einstein's photoelectric effect explained and corrected the controversy. His theory postulated that a beam of light consisted of small quanta of energy called photons and that an electron in the metal absorbs the incident photon's energy required to break free from the metal. The electron would get all the photon's energy or none at all. The energy of a photon, E_{ph}, can be described as $E_{ph} = h\upsilon$, where υ is the frequency, h is the Planck's constant which is $6.626 * 10^{-34}$Js. And frequency can be described as $\upsilon = c/\lambda$ where c is the speed of light which is $3.0 * 10^{8}$m/s and λ is the wavelength. Einstein's photoelectric effect with energy of photon suggested that light behaves like particles.

In 1924, de Broglie proposed that not only light but all matter, including electrons, has a wave-particle dual nature. He suggested that an electron in an atom might be associated with a circular standing wave shown below.

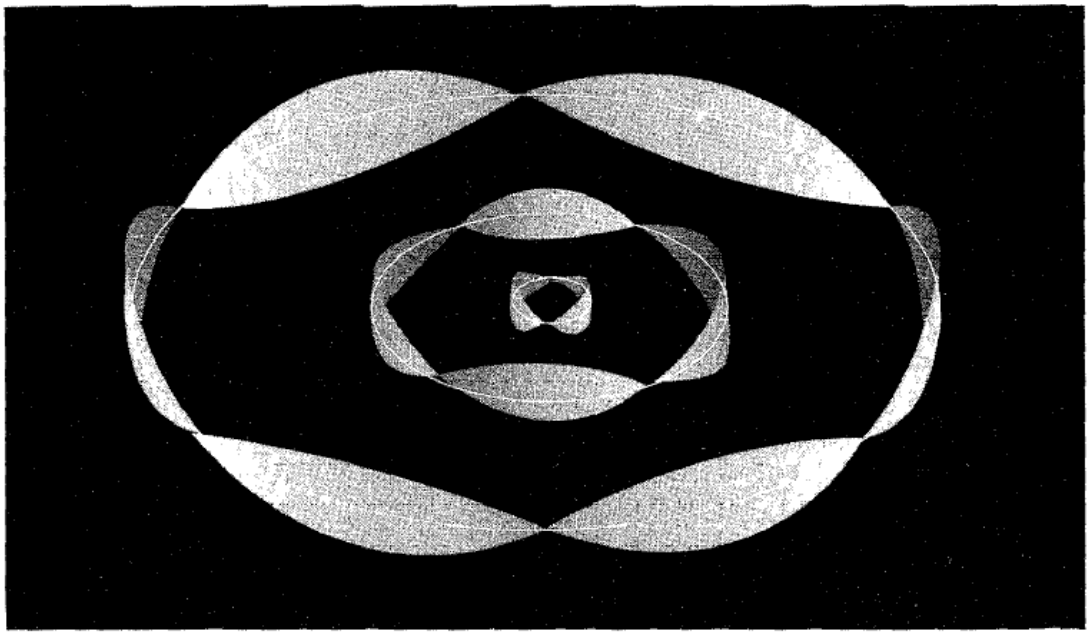

Figure 4. Circular Standing Wave [6]

The condition for the circular standing wave is $n\lambda = 2\pi r$. Combining the equation for circular standing wave and Bohr's assumption that the angular momentum is quantized and must be an integer multiple of $h/(2\pi)$, results in wavelength, $\lambda = \frac{h}{p}$, where p is momentum. As a result, the wavelength is related to the linear momentum p of the electron or a particle. De Broglie showed with the theory of relativity that the exact same relationship holds between wavelength and momentum of a photon. Thus, he proposed that any particle moving with linear momentum (p) has wavelike properties and a wavelength associated with it. Within three years, two different experiments proved his propositions. In 1927, Heisenberg stated the uncertainty principle that the position and the momentum of a particle on an atomic scale cannot be simultaneously determined with

precision. He came up with the equation that describes his principle $\Delta x \Delta p \geq h$ where h is Planck's constant and Δx is the uncertainty of the position and Δp is the uncertainty of the momentum or velocity. It can be said either momentum or velocity because momentum is proportionally related to velocity. Heisenberg said that the inability to determine both position and velocity simultaneously is due to dual nature of matter. As a result, electrons can never be found explicitly. In 1925, Erwin Schrodinger developed a differential equation, based on de Broglie's notion of dual wave-particle nature of electrons. The Schrodinger's equation, which is time-dependent, can be formulated as:

$$-\frac{\hbar^2}{2m}\nabla^2\psi + U(x,y,z)\psi = -\frac{\hbar}{i}\frac{\partial\psi}{\partial t} \tag{2.1.1}$$

where $\hbar$ is denoted as h/(2π), m the mass of the particle, ψ is the wave function, *U* the potential energy, *t* the time, and *i* the imaginary unit . When solved for the wave function, it describes the distribution of the particles in space. It is also related to the probability of finding the particle in each of various regions. Specifically, the particle is most likely to be found in regions where the wave function is large. The electron's position is measured in probability because it can never be found explicitly according to Heisenberg's uncertainty principle. Because the Schrodinger's equation is very difficult to solve due to the dual nature of a particle, time-independent Schrodinger's equation is developed using the standing wave:

$$-\frac{\hbar}{2m}\nabla^2\psi + U(x,y,z) = E\psi \tag{2.1.2}$$

where E is the total (kinetic) energy of the particle. Thus though both position and velocity of a particle in a specific state cannot be simultaneously known, the energy of a particle in a stationary state can be exactly found. To see how Schrodinger's equation

works, a simple example of a particle in one dimensional box where it is free to move in the box with momentum, p is shown below.

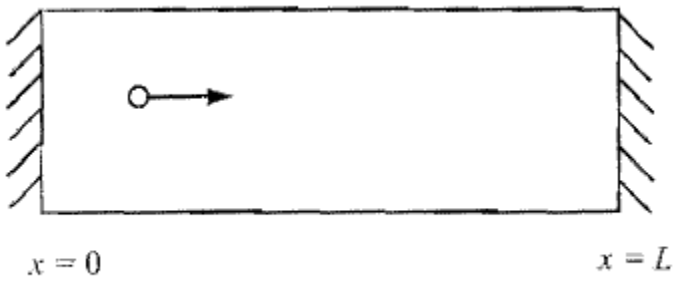

Figure 5. A particle in a one-dimensional box [6]

The solutions to the Schrodinger Equation can be shown graphically and are depicted below.

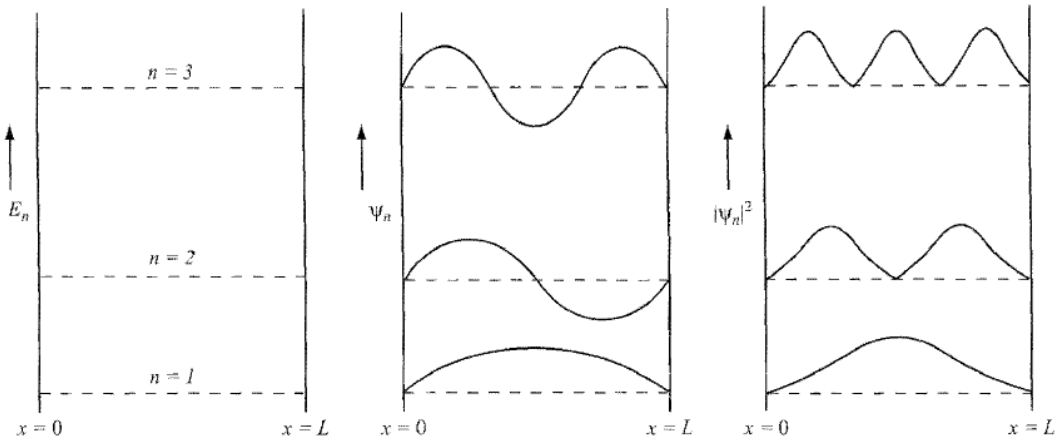

Figure 6. Graphical Solutions to the Schrodinger Equation [6]

From left to right, the graph shows the potential energy for a particle in a box of length L, wave function and the probability.

Solving the Schrodinger equation allows us to find energy and wave function that correspond to each quantum number n. These are the only allowed stationary states of the particle in the box. From the results of solving the Schrodinger's equations, we can describe and predict the behavior of electrons in many-electron atoms [6].

2.2 - Silicon Solar Cells

Silicon is used for solar cell production because of its chemical properties and crystal structure, making it one of the best semiconducting materials when doped with other atoms such as phosphorous and boron [6]. The silicon crystalline structure has four valence electrons and four open spaces which are bonded with four neighboring silicon atoms, creating a crystal lattice structure. This tetrahedral configuration occurs throughout the entire structure [7].

Pure crystalline silicon is not very conductive. To increase the conductivity of the semiconductor, it is doped with other elements. The p side of the p-n junction is typically doped with boron and the n side is typically doped with phosphorous.

Each material has a band gap which is the limit for the energy needed to excite an electron. Photons in some parts of the light spectrum do not have the energy necessary to excite the electrons and will pass through the cell, or will contain too much energy which will be lost and reduced to band gap energy by thermalization [8].

Silicon has a band gap of 1.12 electron-volts (eV), which yields a 30% efficiency. GaAs has a band gap of 1.42 eV, which closely matches the maximum possible efficiency. Increasing the band gap energy causes a decrease in the photocurrent but causes an increase in open-circuit voltage. Energy conversion efficiency is dependent on both the short-circuit current and the open-circuit voltage [6].

The development of silicon solar cells paralleled the development of silicon use in integrated circuit technology. The first silicon solar cell was created by Chapin, Pearson, and Fuller at Bell Laboratories in 1954 [5] and can be seen in Figure 7.

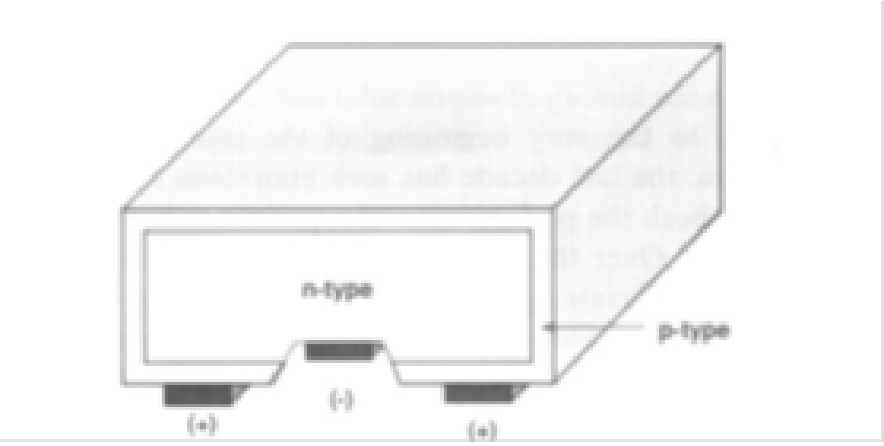

Figure 7. The first modern solar cell [9]

Improvements in the 1970s focused on the cell's ability to collect carriers generated by the incoming photons. After these improvements, further research focused on increasing the open-circuit voltage of cells. Many times, solar cells were made from silicon scraps leftover from microelectronic construction. The silicon, however, was less pure so it was less efficient but it was cheaper than the purer silicon.

Silicon solar cells can be created in many different forms. These forms are: single-crystalline, multi-crystalline, and thin-film cells. The following section will discuss each of these types and how the cells technology advanced with time.

2.2.1 - *Single-Crystalline*

The evolution of silicon solar cells can be separated into three major phases: the 1950s, which focused on the development of crystal growth and junction diffusion techniques as well as the refinement of cell design, the 1970s, which focused on the development of shallow junctions, photolithographically defined metallization, improved antireflection coatings and surface texturing, and the 1980s, which focused on surface passivation, bulk lifetimes, contact passivation, and light trapping in the cell.

In 1954, at Bell Laboratories, Daryl Chapin, Calvin Fuller, and Gerald Pearson discovered the first diffused Si p-n junction. These men were experimenting with semiconductors and accidentally found that Si doped with certain impurities was very sensitive to light [10]. Bell laboratories developed a technique for producing single crystal silicon wafers as well as a technique for doping, using high temperature diffusion of impurities. The solar cell developed at Bell Laboratories had an efficiency of 4.5% but was increased to 6% when lithium diffusion was replaced with boron diffusion [9]. Eighteen months later, the 10% efficiency mark was achieved by Hoffman Electronics.

In the 1960s, as the world raced towards space, solar cells were being developed for use in space. These developments pushed efficiencies up to about 14%. To increase the efficiency, contact grids were added to the top surface of the cell. These grids are made up of a good conductor and placed on the top surface of the cell to collect electrons.

In 1960, Hoffman Electronics created a 14% efficient solar cell. This solar cell was the first to put contact grids on the top surface and the cell was developed for use in space. The cell, as can be seen in Figure 8, became the standard cell design for at least a decade [9].

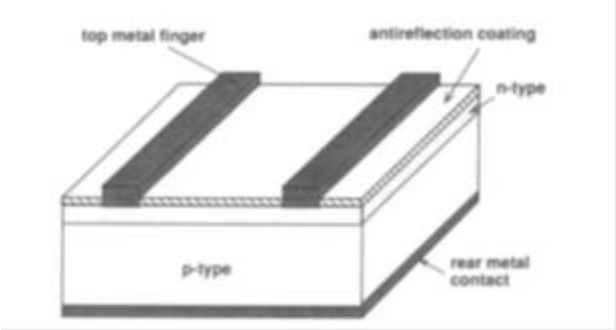

Figure 8. Design for a Space Solar Cell (1960) [9]

In 1973, *Violet*, a cell developed at COMSAT Laboratories, exceeded 14.5% efficiency. This cell improved the cell current by extending the response to shorter

wavelengths in the blue end of the light spectrum. *Violet* also had photolithographically defined top contact fingers which lead to better etching of the solar cell surface yielding a better efficiency for solar current collection. This fine geometry has the advantage of improving efficiency of solar cells in the blue-violet portion of the spectrum corresponding to 0.3 - 0.5 microns by minimizing the reverse current from the front layer to the junction of the solar cell [11].

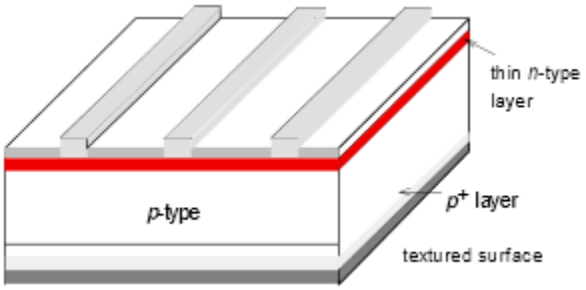

Figure 9. Shallow Junction *Violet* Cell [12]

In addition to photolithography, anti-reflective cell coatings were also a concurrent development that led to better solar cell efficiency. Increases in short-wavelength response paved the way for the initiation of coatings research, particularly of tantalum pentoxide and niobium pentoxide [13]. The cell also had an increased fill factor which led to higher efficiencies [14].

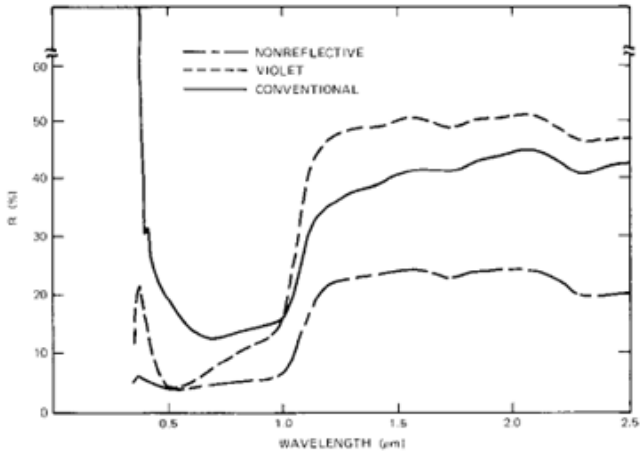

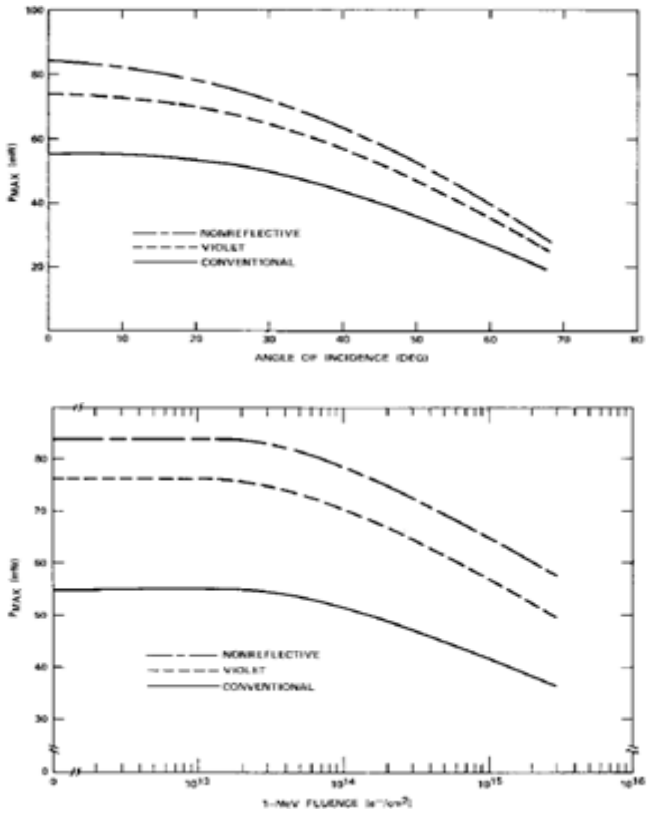

Figure 10. The three graphs above compare the reflectivity and the maximum power output of non-reflective, *Violet*, and conventional cells. Non-reflective cells perform better in both power output and reflectivity than conventional cells [13].

COMSAT then went on to develop a non-reflecting cell using textured surfaces achieving efficiencies of about 17.3%. The cells produced a higher current due to the new surface structure of the cell and improved optical properties. Anisotrophic etching was used to expose the crystal planes in the silicon, producing pyramids in random locations on the top surface of the silicon. This technique reduced reflection on the top surface of the cell and allowed light to be absorbed near the top junction of the cell, the most active region [15].

In 1983, the University of New South Wales (UNSW) developed Metal Insulator NP junction (MINP) cells that demonstrated efficiencies of 18%. These cells demonstrated high output current attributed to low optical losses and good substrate properties. There were low reflection losses across a wide range of wavelengths. These

cells performed well due to high optical efficiencies and low resistance losses. This cell introduced the modern period of cell development [16].

That same year, UNSW also created a passivated emitter solar cell (PESC). This cell improved passivation along the top surface of the cell which led to increased voltage output. Passivation is the process of adding an oxide layer to the top surface of a semiconductor in order to isolate the transistor surface from the external environment, thereby improving electrical stability by raising power dissipation and decreasing reverse current leakage. This process uses thermally-grown oxides to passify the non-contact areas of the cell. Furthermore, photolithography was used to pattern the top contact fingers and to align the fingers to the oxide openings [12]. The PESC also used a reduced area of contact with the top metal surface of the cell, leading to improved top surface qualities of the cell [15].

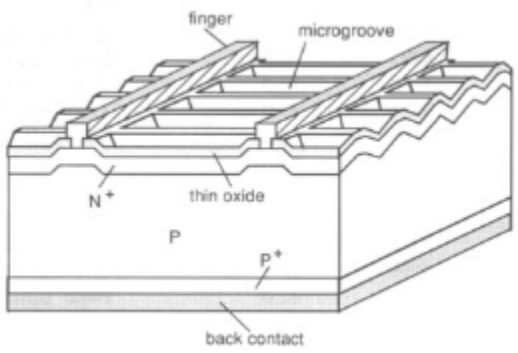

Figure 11. The passivated emitter solar cell (PESC), the first silicon solar cell to surpass efficiencies of 20% [9]

In 1985, the UNSW PESC cells surpassed efficiencies of 20%, using high quality float zone wafers that were doped with boron. Reaching above 20% efficient was a huge milestone because it had been thought that 20% was the limit for silicon solar cells [15].

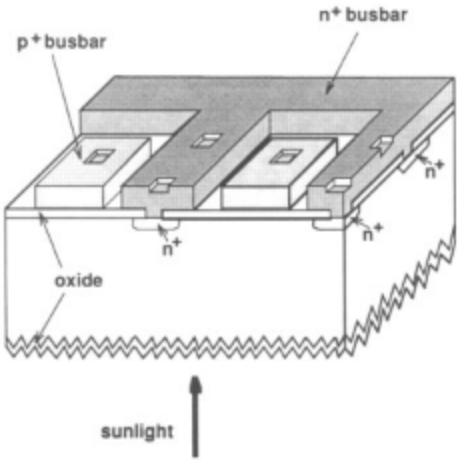

Figure 12. Point contact cell which has oxide passivation of both the top and rear surfaces [9].

In September of 1988, Stanford University created rear point-contact cells. The effectiveness of this design relied on oxide passivation occurring at both the front and rear of the cell, and the high quality bulk material of the cell. This design reduced contact recombination by making the contact points very small and locating them on the non-illuminated surface of the cell. As carriers are generated at the illuminated surface, they cross the substrate and go on to the contact regions. These cells reached 22% efficiency under terrestrial conditions and 27% efficiency under highly concentrated light [15].

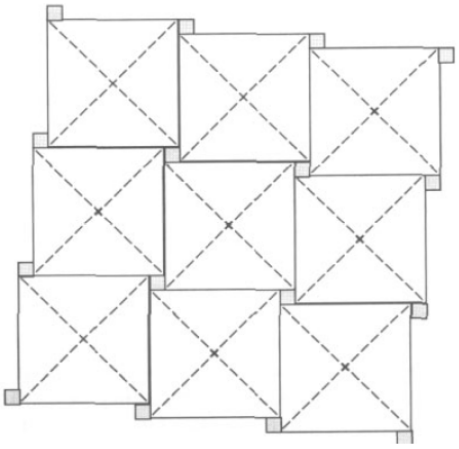

Figure 13. Staggered inverted pyramid design used for the PERL cells [9]

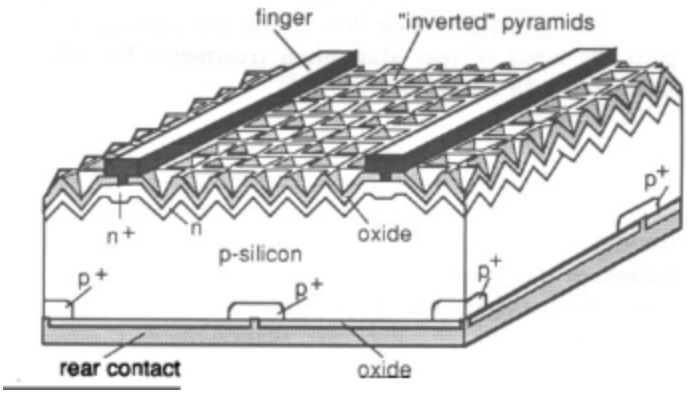

Figure 14. PERL cell which demonstrated efficiencies above 23% [9].

The UNSW created passivated emitter, rear locally diffused (PERL) cells in 1989. These cells combine the earlier USNW PESC cell design and Stanford's rear point-contact cells. The researchers at UNSW staggered inverted pyramids along the top surface of the cell to improve the optical properties and added a rear reflector, which was an oxide layer covered by an aluminum layer [15]. In this cell, when the photon hits the cell, the photons will hit one of the walls of the pyramid becoming coupled onto the cell. The light that was not absorbed will be reflected downwards, giving the photons a chance to be absorbed into the cell [15].

In 1999, "honey combed" textured mono-crystalline solar cells were developed. The cells are completely enveloped in thermally-grown oxide to reduce detrimental electronic activity. These cells also have an isotropic etching to form a hexagonally symmetric "honeycomb" surface pattern. This pattern reduces losses from reflection and increases the optical thickness of the cell by trapping light in the cell by internal reflection [17].

2.2.2 - *Multi-Crystalline Cells*

The development of multi-crystalline cells parallels the development of single crystalline cells. Multi-crystalline, or polycrystalline (p-Si), silicon solar cells are cheaper and less efficient than single crystalline cells. Instead of the very controlled crystal growth process used in single-crystalline cells, a casting of molten silicon into the desired form may be used to produce the multi-crystalline substrate. The faster the silicon cools, the smaller the crystals form within the mold. The performance of multi-crystalline solar cells is degraded due to defects. Defects such as dislocations, impurities, and precipitates exist at high concentrations. The most important issue with multi-crystalline cells is grain boundary defects, which caused efficiencies to level off at 20.4% in 2004. Grain boundaries are internal interfaces that separate neighboring disoriented single crystals in a polycrystalline solid. Grain boundary defects result in the degradation of the minority carrier lifetime and the diffusion length [18].

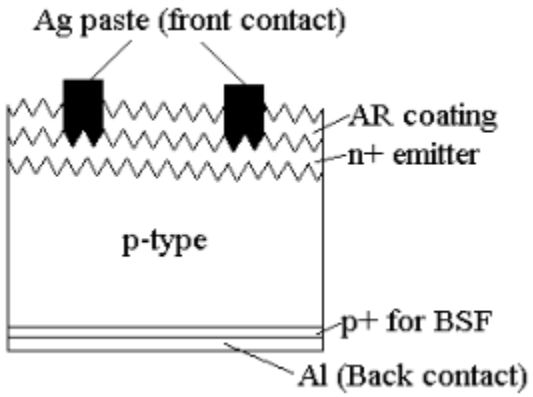

Figure 15. Schematic view of a multi-crystalline solar cell [18]

In 1976, the modern approach to multi-crystalline cells was developed. Lindmayer studied the effect of grain size on efficiency to estimate the best performance of a cell. If the grain size in the cell is highly ordered, then the efficiency is a linear

function of grain size. He concluded that semi-crystalline silicon of less than semiconductor grade purity may be an important raw material for use in inexpensive silicon photovoltaic systems [19].

Fischer and Pschunder experimented with unconventional non-single crystalline silicon, which has a controlled size and structure of the individual grains. They used modified processing that was optimized with respect to the unique structure of the material. They concluded that unconventional non-single crystalline has potential to be a low cost application to silicon solar cells [20].

Using both methods described by Lindmayer and Fischer and Pschunder, Solarex achieved 10% efficiency in 1984. Later, Solarex was able to improve the efficiency to 16%. In 1990, the UNSW PESC cell achieved an efficiency of 17.8%. The team at UNSW discovered that the presence of grain boundaries causes the gap in efficiency between multi-crystalline and mono-crystalline cells. They incorporated phosphorous pretreatment and rear aluminum treatments into the PESC sequence to lessen the effects of the grain boundaries [21]. The phosphorus pretreatment resulted in the improvement of the diffusion length and cell parameters [21]. M.A. Green was able to increase efficiency by 1% by incorporating buried contact technology in their cell. They also used a laser technique for texturing which reduced stress concentration during oxidation [18].

In 1994, Georgia Tech developed plasma-enhanced chemical vapor deposition (PECVD) passivation which involves a low temperature PECVD of silicon oxide (SiO_2) and silicon nitride (SiN) followed by a photoassisted anneal. This is effective for use in both surface and bulk defect passivation in multi-crystalline Si materials. The effective recombination lifetime increased by a factor of two to ten depending on the multi-

crystalline material [22]. In 1995, they received a United States Patent for low temperature plasma-enhanced chemical vapor deposition. PECVD of SiN and SiO_2 creates an effective double layer coating used for anti-reflection [23].

The next year, Georgia Tech created a heat-exchanger method (HEM) multi-crystalline material. Rohatgi et. al. increased the impact of back surface recombination velocity of solar cell performance. This involved impurity gettering and effective back surface passivation of multi-crystalline silicon grown by the heat-exchanger method. This lowered the velocity which resulted in higher efficiencies. The effect of the grain boundary can be neglected with this method because of large grain size [24].

In 1999, Zhao developed "honey-combed" textured multi-crystalline solar cells. The cells were completely enveloped in thermally grown oxide to reduce detrimental electronic activity and had isotropic etching to form hexagonally symmetric "honeycomb" surface pattern. This pattern reduced loses from reflection and increased the optical thickness of the cell, causing light to be trapped due to internal reflection [17].

In 2004, Shultz et. al. created an FhG-ISE Laser PERC cell which reached about 20.4% efficiency. This has been the highest efficiency reported thus far in multi-crystalline solar cells. They wanted to create a cell design with good light confinement and highly quality surface passivation. The best performance that has been reported was on a cell with oxide-passivated rear surface with locally defined contacts. Thermal oxidation is the most promising technique to create high efficiency multi-crystalline cells. The rear contact pattern was fired through the oxide by an LFC laser because Schultz et. al. needed to create a contact pattern with closely spaced contacts. The application of a

wet oxidation for rear surface passivation reduces the process temperature and thus prevents degradation of the minority carrier lifetime [25].

2.2.3 - *Silicon Heterostructures (HIT)*

Silicon HITs are Heterojunctions with an Intrinsic Thin layer, an amorphous-Si:H (a-Si:H) layer, between the p- and n-type materials.

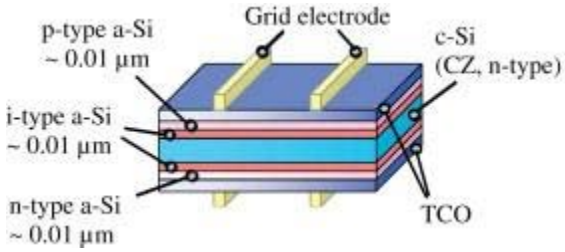

Figure 16. Structure of a Silicon HIT [26]

In the figure above, a typical structure of a Silicon HIT is displayed. An intrinsic a-Si layer, a doped a-Si layer, and a TCO layer are deposited on both sides of a crystalline Si substrate. Transparent conducting oxides (TCO) are degenerate semiconductors with good electrical conductivity and high transparency in the visible light spectrum, which is why they are often used in thin film solar cells [27]. Grid electronics are fabricated on both sides of the amorphous-Si layer. A high-quality intrinsic a-Si layer can effectively passivate the surface dangling bonds of the crystalline substrate. An HIT solar cell has a symmetrical structure and does not use high-hardness alloy metals as electrodes. It achieves a stress-free cell structure which is well suited to thinner substrate solar cells [26].

In 1992, Sanyo developed HIT cells. The intrinsic a-Si layer was introduced which allowed for better passivation of silicon wafers. These cells has a maximum

conversion efficiency of 14.8% [28]. In 2001, an application of a textured substrate and back surface field (BSF) increased conversion efficiency to 20%.

In 2008, improvements to the HIT were made by enhancing the conversion efficiency, utilizing a thin wafer for the HIT cell, improving the temperature coefficient, and applying HIT solar cells to bifacial solar modules. Furthermore, a high potential for use on thinner c-Si wafers was discovered and a high conversion efficiency of 21.4% was reached [29]. Tsunomura et. al. achieved a 22% efficiency was reached by improving the a-Si/c-Si heterojunction, improving the grid electrode and reducing the absorption in the a-Si:H and TCO layers [30].

Sanyo created a 23% efficient HIT cell in 2009. There are three key technologies necessary for improving the conversion efficiency of HIT solar cells: improving the HIT structure, optimizing the grid electrode, and improving the optical confinement structure [26].

2.2.4 - *Amorphous/Thin-Film Cells*

Thin-film cells were developed concurrently with crystalline silicon solar cells. Thin-film cells use less silicon and shorten the paths on which the free electrons have to travel. This reduces the probability of recombination, which can lead to an increase in efficiency [6]. There are many features of thin film technologies that are advantageous for solar cells. Thin films offer a wide variety of shapes, sizes, and substrates that can be used. Furthermore, surfaces of thin films can be modified to obtain the optical reflectance and optical trapping effects that are needed [27]. Amorphous silicon solar cells are more cost effective and simpler to produce than crystalline cells [7]. Thin-film solar cells

encompass a considerable thickness range, varying from only a few nanometers to approximately 50 µm [6]. Thus, it is best to define thin film technologies in terms of the process by which they were created rather than by thickness.

	a-Si/SiGe	c-Si *
Grain Size (µm)	Amorphous	Single Crystal
Sub. Temp. (•C)	< 300	1000-1400
Typical Growth Methods	CVD	epitaxy + "epi-lift," "smart-cut"
Rates (µm/m)	0.01-0.1	1-10
Efficiencies (%)	8-13	~18
Cell Thk. (µm)	0.3-0.7	5-50
Cell Type	drift, stacked	diffusion
Pros	very high absorption, E_g tailoring	infrastructure, synergy with IC industry
Cons	instable (SWE), poor red collection	3-step processes, large area difficult

Figure 17. A general comparison of amorphous silicon to crystalline silicon summarizing its properties and advantages [7]

Thin-film silicon solar cells are usually amorphous, meaning non-crystalline. The bonding of silicon atoms is essentially the same as in crystals, however, the variation in the bond angles create an irregular lattice structure. The conductivity of amorphous crystalline structures would increase dramatically when mixed with phosphine (PH_3) gas or diborane (B_2H_6) gas, analogous to the doping in crystalline cells. It was discovered that plasma-deposited amorphous silicon has an efficiency of up to 14.6% due to a high percentage of hydrogen atoms bonded with the silicon, making them more conductive (hydrogenated). a-Si layers absorb more energy than c-Si layers which means that less material is needed [7].

a-Si panels are formed by vapor-depositing a thin layer of silicon material, about 1 µm thick, on a substrate material such as glass or metal. a-Si can also be deposited at very low temperatures, as low as 75ºC, which allows for deposition on plastic as well. In

its simplest form, the cell structure has a single sequence of p-i-n layers. However, single layer cells suffer from significant degradation in their power output when exposed to the sun. The mechanism of degradation is called the Staebler-Wronski effect. Better stability requires the use of thinner layers in order to increase the electric field strength across the material. However, this reduces light absorption, and hence, cell efficiency. This has led the industry to develop tandem and triple-layer devices that contain p-i-n cells stacked one on top of the other [7].

The first amorphous silicon layers were deposited by R. Chittick. He was working with silane plasmas and unintentionally attained amorphous silicon layers in parts of his plasma reactor. Chittick's findings were then furthered explored by W.E. Spear at Dundee University. Spear and coworkers published the first study on plasma-enhanced chemical vapor deposition (PECVD) with silane and other doping gases. Spear's study showed that it is possible to dope amorphous silicon layers, which enables semiconductor devices to be built. However, p-n type diodes should not be used as the solar cell structure for amorphous silicon. This is because amorphous silicon has poor doping capability and doping also has a detrimental effect on the amorphous silicon layer quality. The quality of this layer decreases because it creates numerous silicon dangling bonds which are the recombination centers for this material [31].

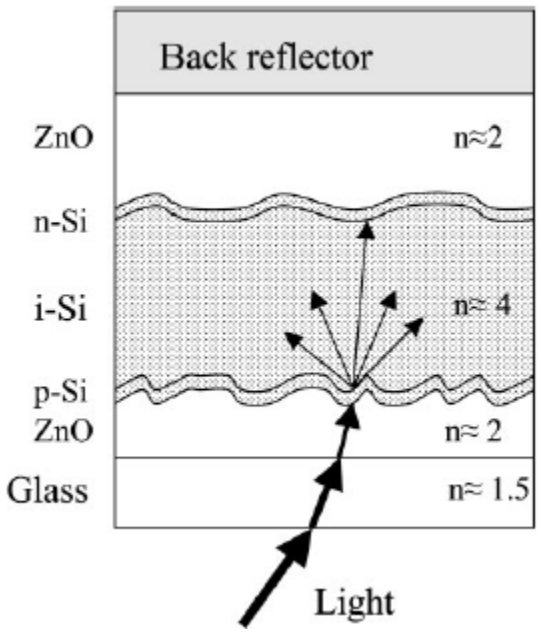

Figure 18. Sketch of a p-i-n thin silicon solar cell, as used of amorphous silicon. The indicated n values give the value for the index of refraction, a parameter for light trapping [31]

As a result of the ineffectiveness of the p-n type diodes, the p-i-n diodes are used for amorphous silicon cells. In 1976, David Carlson and Christopher Wronski of RCA Laboratories created the first amorphous silicon PV cells using p-i-n diodes. These cells had an efficiency of 1.1%. The p-i-n structure consisted of a p-type doped layer, central i-type, photovoltaically active, layer, and an n-type doped layer. They created solar calls ~1 μm thick from amorphous silicon deposited from a glow discharge in saline. A year later the Staebler-Wronski effect (SWE) was discovered [31]. The discovery of the SWE led to many studies on the origin of the effect and how to eliminate its detrimental effects. Progress has been made in understanding how the effect works and making changes in materials in order to enhance cell performance [32]. Light degradation caused by the SWE has been decreased by reducing the thickness of the amorphous silicon layer so that carriers move a shorter distance before they reach the electrode. However, the thinning of

this layer results in lower light absorption which causes fewer photons to be absorbed [27].

RCA Laboratories achieved initial efficiencies of 10% in 1982. The main problem with a-Si is the Staebler-Wronski effect, which is a light induced degradation. The cells can only stabilize to lower efficiencies after ~1000 hours of illumination. This occurs due to the creation of new defects that act as recombination centers [33].

In 1986, Solarex created a method for developing superlattice doped layers for a-Si. The superlattice has a number of first and second lattices of amorphous silicon alternatingly formed on one another. Each first lattice has an optical band gap and each second lattice has a different optical band gap [34].

In 1992, United Solar created double-junction a-Si based solar cells. They achieved 11% efficiency and used a profile band gap a-SiGe alloy in the bottom of the cell. From 1992-1995, United Solar made improvements to their design. They used hydrogen dilution to improve cell stability; they optimized the p- and n-type layers, doping them to have high conductivity. United Solar achieved 9.3% efficiency with a single-junction cell and 10.1% efficiency with a double-junction cell, using the same band gap. The double-junction cell incorporated Ge in the bottom layer of the cell. They achieved 12.4% efficiency in a double-junction, dual band gap cell and 13.0% efficiency in a triple-junction, multi-band gap cell. A triple-junction a-Si cell can reduce the effects of the Staebler-Wronski effect [35].

United Solar improved on their triple-junction a-Si alloy solar cell in 1997. They achieved 13% stable efficiency with an a-Si-based alloy in a spectrum-splitting, triple-junction structure. United Solar made improvements to the low band gap a-SiGe alloy

cell, the p-n tunnel junction between the component cells, and the top conducting oxide [36].

In 2009, United Solar achieved 12.5% efficiency with a triple-junction amorphous/nano-crystalline silicon device (a-Si/nc-Si/nc-Si). United Solar pushed research-level performance higher by producing a triple-junction a-Si/nc-Si/nc-Si sub-module with an efficiency of 12.5% on a stainless steel foil. The initial cell performances of a-Si:H/nc-Si:H double-junction and an a-Si:H/nc-Si:H/nc-Si:H triple-junction solar cells are very similar. However, the light-induced degradation is significantly different. For the double-junction cells, the light-induced degradation is ~15% while it is less that 5% for the triple-junction solar cells. Compared to a-Si:H and a-SiGe:H materials, nc-Si:H materials have two major advantages in solar cell applications. First, the nc-Si:H material is a mixture of nanometer-sized grains and amorphous tissues. The carrier transport is mainly through the crystalline paths, where the carrier mobility is much higher. This allows the solar cell to be thick enough for high photocurrent. In addition, the amorphous phase in nc-Si:H absorbs the short wavelength light more efficiently than c-Si:H, while the nanocrystallites absorb the long wavelength light. Second, nc-Si:H solar cells are more stable against light soaking than a-Si:H and a-SiGe:H solar cells, which can lead to high efficiency solar modules [37].

2.2.5 - *CIS*

In 1976, the University of Maine developed thin-film p-$CuInSe_2$/n-CdS heterojunction solar cells. They reported efficiencies around 4-5% and suggested that a $CuInSe_2$/CdS solar cell can be a viable alternative to other thin-film technologies.

$CuInSe_2$ is a direct band gap semiconductor which minimizes the requirements for minority-carrier diffusion lengths. The lattice match between $CuInSe_2$ and hexagonal CdS is exceptionally good. P- or n-type layers of $CuInSe_2$ can be produced by vacuum deposition. The energy gap of $CuInSe_2$ is 1.04 eV, and is near an optimal value for terrestrial conditions. The electron affinities of $CuInSe_2$ and CdS are close enough to minimize any potential barriers to the photoinduced carriers [38].

In 1982, Boeing demonstrated 10% efficiency with a Mo/$CuInSe_2$/CdS/Ar Coating structure. The 3 μm-thick $CuInSe_2$ was formed by thermal evaporation of the elemental constituents onto a Mo-coated aluminum substrate. The deposition consisted of two stages in which the elemental fluxes were adjusted to be Cu-rich during the initial stage of deposition at a substrate temperature of 350ºC, forming a Cu-rich $CuInSe_2$ base film. In the final state, the substrate temperature was raised to 450ºC and the Cu:In flux ratio was reduced to less than one. The stoichiometry of the completed $CuInSe_2$ film was Cu deficient. To complete the device structure, the In-doped CdS layer was then evaporated directly from the compound in a resistively-heated Knudsen cell at a substrate temperature of 175ºC [39].

2.3 - Multi-junction Cells

Thus far, we have mostly focused on the theoretical and practical applications of Si photovoltaic cells. Our device, however, utilizes a stack of three cells of different materials placed in parallel. This system of triple-junction cells has the ability to greatly increase the amount of sunlight which can be converted into electrical power. Thus, it is

necessary to discuss the theoretical background of multi-junction cells and how their theoretical efficiencies compare with those of single-junction Si cells.

There are two common methods used to calculate the theoretical efficiency of multi-junction cells, the “Detailed Balance” approach and the more common one-dimensional-transport model which is commonly called the “Standard Model” [40]. In this section, we will discuss each method in detail.

Many previous studies have presented the efficiencies of multi-junction cells as functions of the materials’ band gap. However, because different studies use different assumptions, the range of theoretical efficiencies varies. The calculations are dependent on the temperature of the cell, the concentration, and the light spectrum used. By changing the spectrum, for example, there can be a 1% to 4% change in efficiency. The maximum value of sunlight possible is approximately 46,000 suns and concentrating the light to this level leads to efficiencies that are 10-20% higher than corresponding one-sun efficiencies [40].

Marti *et. al.* compared two models for calculating theoretical efficiencies, the “Standard Model” and the “Detailed Balance” model. The Standard Model uses Shockley’s diode equation to model a one-dimensional p-n junction. This equation requires the use of appropriate values for variables including layer thickness and recombination. The Detailed Balance approach, while using a similar diode equation, calculates the recombination current from surface radiative losses. The main difference between the two methods is that while the “Detailed Balance” model accounts for photon recycling (self-excitation), the “Standard Model” does not. Because many publications

commonly use the “Standard Model”, photon recycling is often ignored, although its effects are well-known [40].

The “Detailed Balance” model for calculating theoretical efficiency allows for an upper bound which is not dependent on device design or material parameters. The diode equation that is used in both methods is:

$$J(V) = J_0 * e^{\frac{qv}{kT}-1} - J_{ph} \quad (2.3.1)$$

where J is the current density as a function of voltage, J_0 is the recombination current, q is the charge, kT is the thermal energy, and J_{ph} is the photocurrent. This equation assumes that there is no series resistance but that there is an infinite shunt resistance. Additionally, the diode-quality factor is at unity. Another major assumption in calculating the ideal value of J_{ph} is that the photovoltaic cell has no reflectance, such that there is a 1:1 ratio for every absorbed photon and resulting electron in the external circuit. Finally, absorbance is also assumed to be zero if the photon energies are less than the band gap plus unity for higher energies [40].

In general, multi-junction efficiency calculations for both methods are made by taking the product of current and voltage at the maximum power point, and dividing this value by the power of the incident spectrum. The difference between the two models comes from the different assumptions for the recombination current, J_0. The recombination current can be measured empirically or simply be estimated based on known material properties. The “Detailed Balanced” method yields a smaller value for J_0 than the “Standard Model”, resulting in a higher efficiency. Ultimately, only the “Detailed Balance” model is truly accurate when calculating theoretical efficiencies, as it takes into account the important factor of photon recycling.

2.3.1 - *"Detailed Balance" Method*

The "Detailed Balance" method for calculating efficiencies is dependent on the density of the conduction band and valence band states and takes into account transition probabilities between these two bands [40]. There are three main types of interaction between the two bands. First, absorption occurs when the p-n junction absorbs a photon. In cases where the layers are close enough and the top junction has absorbed more photons than lower junctions, the "Detailed Balance" model assumes that excess current is transferred radiatively to the lower junctions. Thus, these lower junctions can absorb light that has been reemitted by the top junction. Second, spontaneous emission occurs when an electron spontaneously drops to a lower energy level and emits a photon. Third, stimulated emission occurs when an electromagnetic field passes through and causes an electron to drop in energy level. In this case, the electron takes on all properties of the field, such as frequency, polarization, and phase [41]. By taking these cases into account, the density can be written as a function of quasi-Fermi energies which make the material properties besides the band gap irrelevant [40]. This allows for the calculation of a value for J_0 that is independent of the specific device parameters, such as the doping and thickness of the p-n junction, a great advantage over the "Standard Model" [40]. Instead, the "Detailed Balance" approach uses Planck's Law, which is used to describe the radiation emitted by an ideal black body which absorbs all radiation. Planck's Law requires only the temperature of the cell, the radiating area, and the emissivity of the cell, which is the ability to release absorbed heat [42, 43]. Thus, given a particular cell

temperature, the recombination current J_0 is simply a measure of the emission of a non-ideal blackbody.

Other factors which affect the "Detailed Balance" model are the number of junctions, the absorption edge, and the crystalline structure of the cell. Different trends are observed for single crystal, polycrystalline, and amorphous materials. In general, the highest efficiencies are found with single crystal materials. This is confirmed in the following figures, which compare the various empirical efficiencies to the theoretical efficiency found using the "Detailed Balance" approach for both one sun and concentrated light:

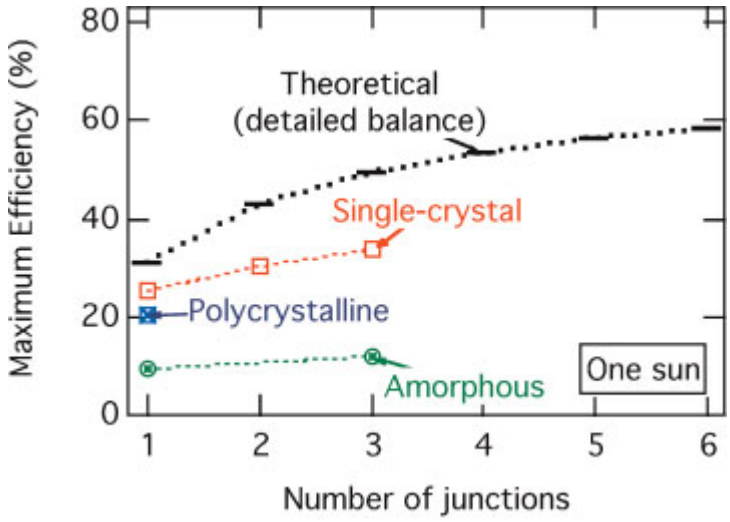

Figure 19. Maximum Efficiency (One Sun) [40]

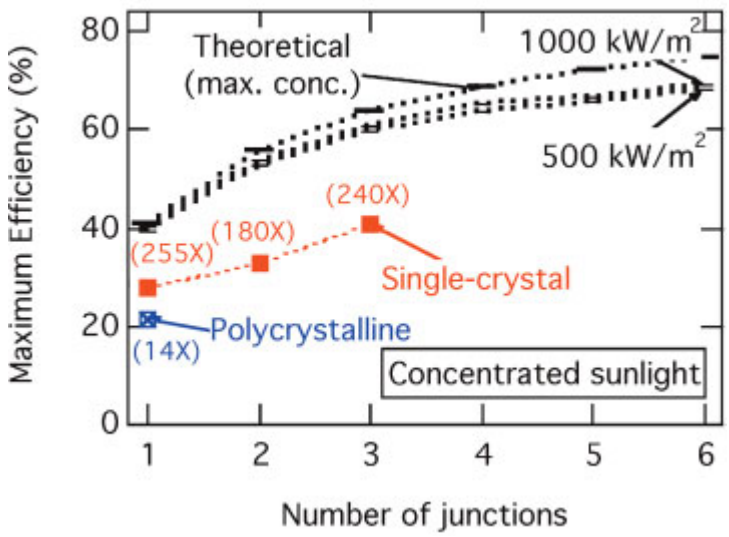

Figure 20. Maximum Efficiency (Concentrated Sunlight) [40]

A final observation from the graphs is that adding junctions to the cell increases the differences between the theoretical and experimental efficiencies, especially for cells with polycrystalline and amorphous structures.

2.3.2 - *"Standard Model" – One-Dimensional-Transport Model*

While the "Detailed Balance" method is gaining traction due to its perceived advantages in calculating efficiency, the "One-Dimensional Transport Model" is still the most commonly used approach in literature, explaining its designation as the "Standard Model". A p-n junction can be modeled in one dimension by assuming two uniform p-type and n-type layers. The relevant parameters for these layers are carrier mobility and lifetime, thickness, surface recombination rate, and the absorption coefficient. The absorption coefficient of this p-n junction and the incident spectrum are then used to calculate the rate of electron-hole pair generation. Conversely, the results from the one-dimensional approach can be matched with experimental data by using relevant values

for the thickness and absorption coefficient. This presents the ability to iteratively determine surface recombination rates and the minority carrier mobility and lifetime for actual devices.

Beyond its application in experimental analysis, the “Standard Model” is also often used for calculating ideal efficiencies. In this case, the recombination current J_0 depends on the minority carrier lifetime, the doping type for each of the two layers, intrinsic carrier concentration, thickness, and the diffusion length. However, as discussed earlier, the “Standard Model” ignores photon recycling, and thus yields lower ideal efficiency calculations than the “Detailed Balance” method [40]. Additionally, rather than assuming that lower junctions absorb reemitted light from the top junction like the “Detailed Balance” approach, the “Standard Model” simply accounts for this variable by assuming the top layer is thinner than the others. This leads to an overall lower recombination current J_0.

Altogether, the “Standard Model” and the “Detailed Balance” model take very different approaches to calculating efficiency. While the “Standard Model” does not account for self-excitation, the “Detailed Balance” model does not account for specific device parameters. Thus, it is clear that these models must be considered carefully when conducting a study, as they can yield very different efficiencies from the same data set. However, both models are critical to research in the field because they provide a standardized set of tools for researchers from various backgrounds to model both theoretical and practical multi-junction cell efficiencies.

2.3.3 - *Methods of Cell Stacking*

We have thus far discussed the theoretical efficiencies of multi-junction photovoltaic cells and described how these efficiencies are calculated. However, the application of these calculations to non-controlled environments has only been briefly discussed. It is very important that multi-junction cell efficiencies be considered in the context of real-world situations. As discussed earlier, practical efficiencies are usually recorded to be between 75% and 80% of the corresponding theoretical efficiencies. For triple-junction solar cells, recent experimental work by R.R. King of Spectrolab has yielded an experimental efficiency beyond 40%. This record is an important benchmark that researchers in the field have been eager to reach for several years. King's high experimental efficiency was achieved using lattice-mismatched cells, which are also called metamorphic cells. The lattice-mismatched method is one of two major means by which different cells are stacked together. The other method is known as the lattice-matched method[44]. The science behind these two styles of cell stacking will be described in the following section [44].

Due to the limited amount of possible crystalline substrate materials, it is difficult to create multi-junction designs which utilize lattice-matched architectures [45]. However, the metamorphic method allows for significant flexibility in semiconductor design. Generally, a crystalline cell structure is described by its lattice constants. These are the parameters which designate the size of an individual unit cell in a crystal structure, and they are thus necessary to calculate the distance between unit cells, and hence the atoms making up the cell structure [46]. The great advantage of the lattice-

mismatched approach to stacking cell layers is that the lattice constraints of the individual substrates do not matter. Because the lattices of adjoining cells do not need to match up, unique semiconductor designs become possible. This additionally allows for a wider range of variation in the band gap used [44].

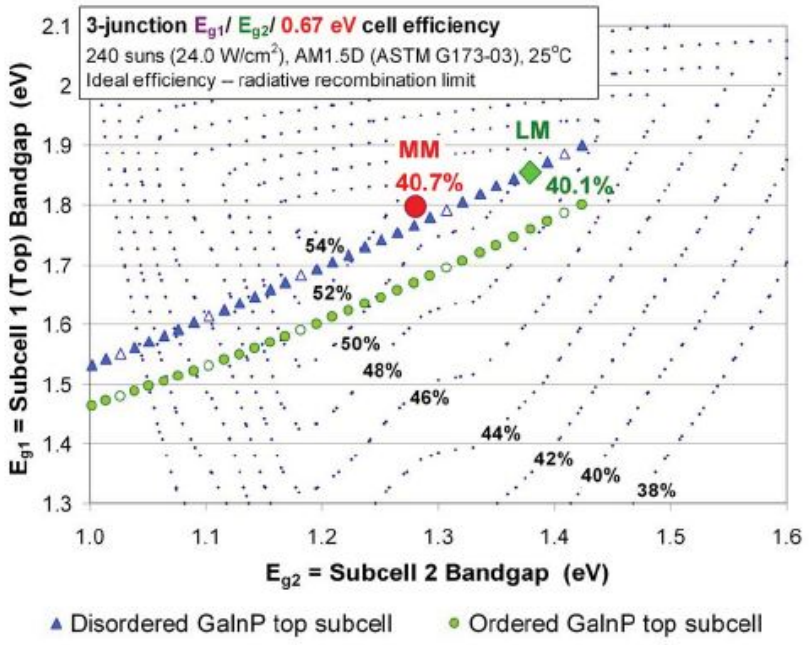

Figure 21. Isoefficiency Contours for Triple-Junction Cells at 240 Suns [47]

The above figure plots the isoefficiency contours for lattice-mismatched and lattice-matched cells at a concentration of 240 suns, where isoefficiency is a method of quantifying efficiency so that it can be scaled and applied to parallel systems such as multi-junction cells [47, 48]. The plot is taken as a function of the top and middle band gaps of the triple-junction system. As can be seen in the figure, the theoretical metamorphic efficiency, represented by the blue line, is 54% while the theoretical lattice-matched efficiency, represented by the green line, is 52% [44]. The red dot denotes the metamorphic experimental efficiency of 40.7% and the green mark notes the lattice-matched experimental efficiency of 40.1%. Thus, the figure confirms that practical

efficiencies of above 40% have been reached, with the metamorphic design having a higher overall efficiency than the lattice-matched design.

Although the lattice-mismatched nature of metamorphic cells provides for flexibility and increased efficiency, there are several types of losses that can occur with this design. These losses can be seen in the following figure and share some similarities with the losses faced by metamorphic cells.

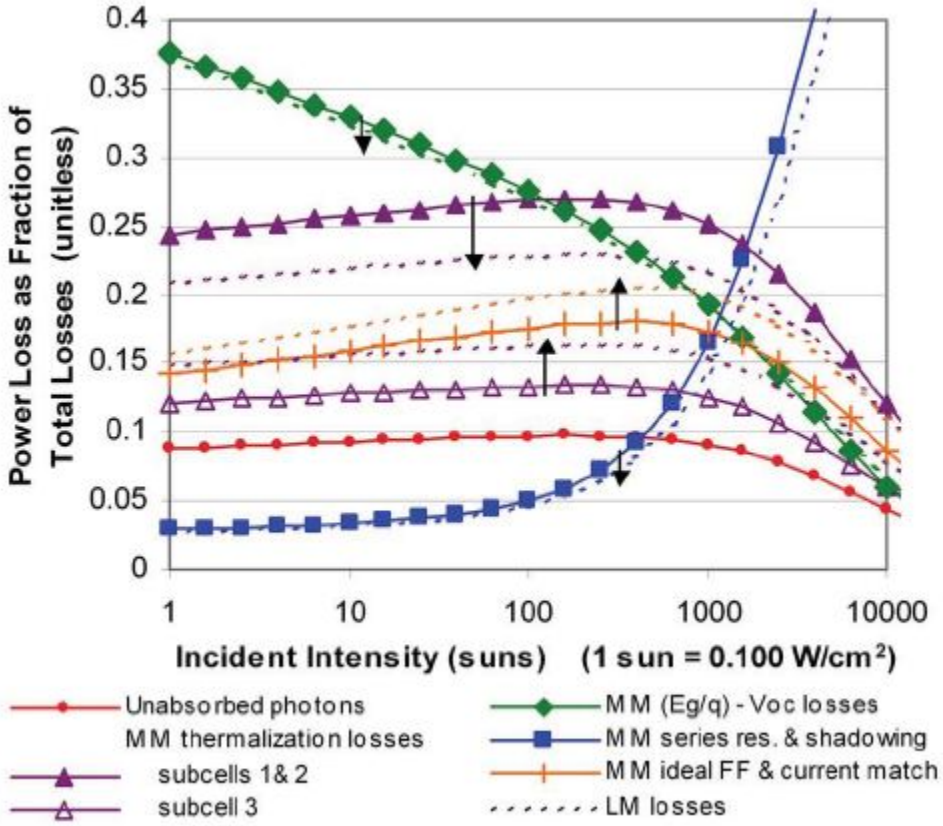

Figure 22. Reasons for Power Losses in Metamorphic Cells [44]

For instance, unabsorbed photons cause the same amount of loss in both metamorphic and lattice-matched cells. However, losses in the top two layers from carrier thermalization are higher for metamorphic devices than for lattice-matched devices because they generally have higher band gaps. Conversely, losses in the third layer of

metamorphic cells are lower because less overall photon energy reaches the cell [44]. Another type of loss present in metamorphic and lattice-matched cells can be found in the band gap-voltage offset, which can be seen in Figure 23.

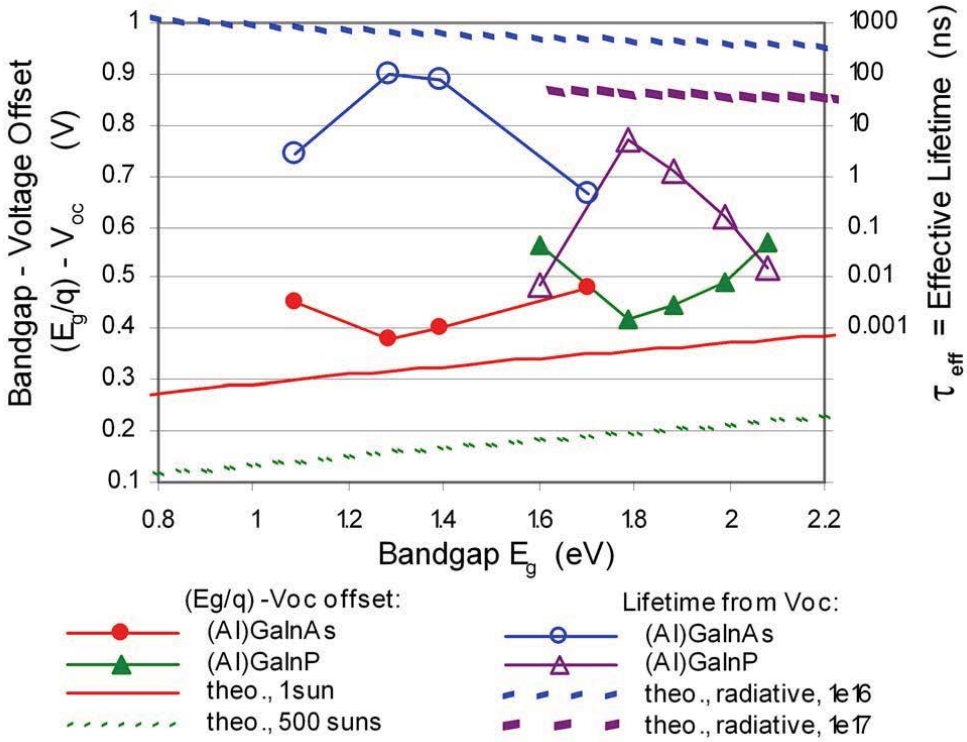

Figure 23. Band gap voltage offset in metamorphic and lattice-matched cells [49]

These losses are due to radiative recombination, which is the action of a photon being released when an electron falls to a lower energy level [49]. Radiative recombination is thus another term for the previously discussed spontaneous emission. In general, however, these losses steadily decrease as light intensity increases. This occurs as hole and electron quasi-Fermi levels in each layer of the multi-junction cell approach their corresponding band edges [44]. Thus, as the concentration of light increases, power losses decrease, signaling an overall increase in efficiency. Despite these losses, metamorphic cells retain the overall advantage in efficiency over lattice-matched cells

due to lower current match losses. This is despite the fact that power losses and metal grid shadowing are greater for metamorphic cells than for lattice-matched cells [44].

Manufacturers face some disadvantages in producing metamorphic cells due to their mismatched structure. These include rough surface morphologies, bowing of the wafer, and cracking of the epitaxial layer [45]. In particular, cell growth that is lattice-mismatched can cause crystal dislocation because the lattice constants of the layers do not match. This dislocation in turn causes energy levels which mediate Shockley-Read-Hall recombination. In order to account for and fix these dislocations, a composition-graded buffer is used. This buffer allows for the layers of the device to be grown at the new lattice constant with a relatively low dislocation density [44].

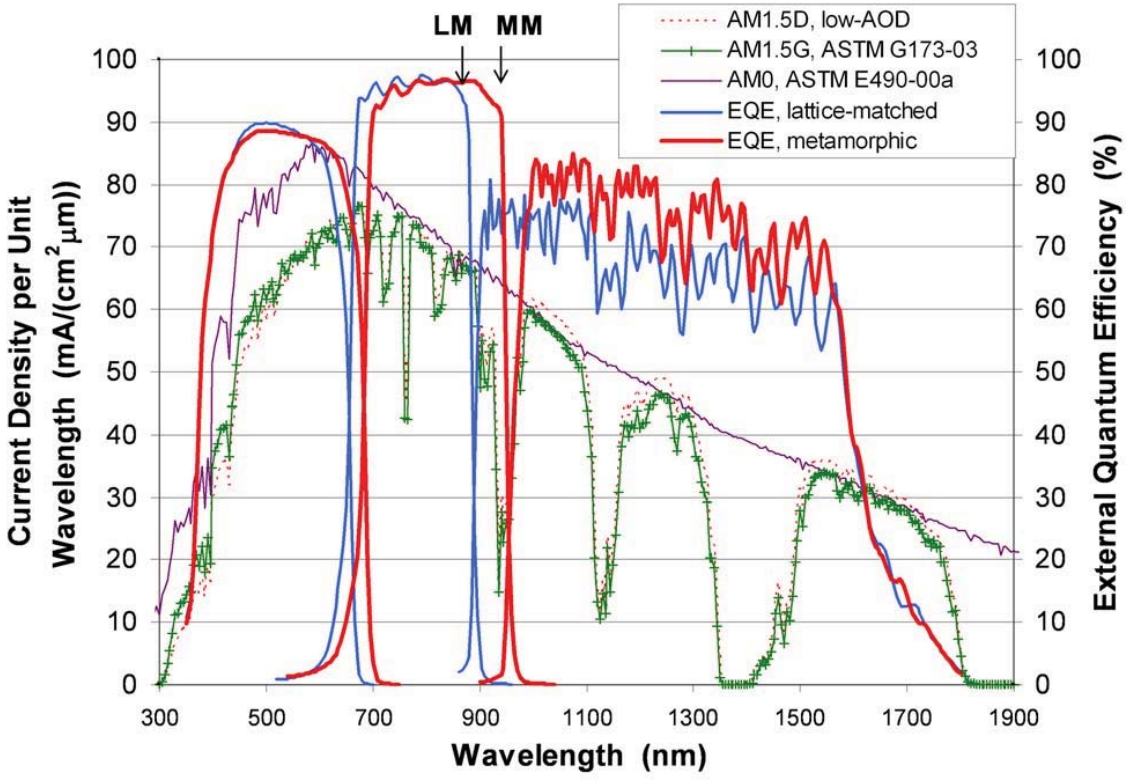

Figure 24. External Quantum Efficiencies for all Three Subcells (GaInP, GaInAs, Ge) [44]

Taking the losses and manufacturing issues into account, the above figure gives an overall view of the quantum efficiencies for all three layers in a multi-junction cell. Specifically, these sub cells are GaInP, GaInAs, and Ge from top to bottom. An important note here is that the top two sub cells have a downward shift in the band gap which allows these layers to absorb a greater part of the light spectrum [44]. Based on these efficiencies, the figure below shows the measured current and voltage (I-V) curve for the experiment conducted by King, which successfully yielded the 40.7% practical efficiency [44].

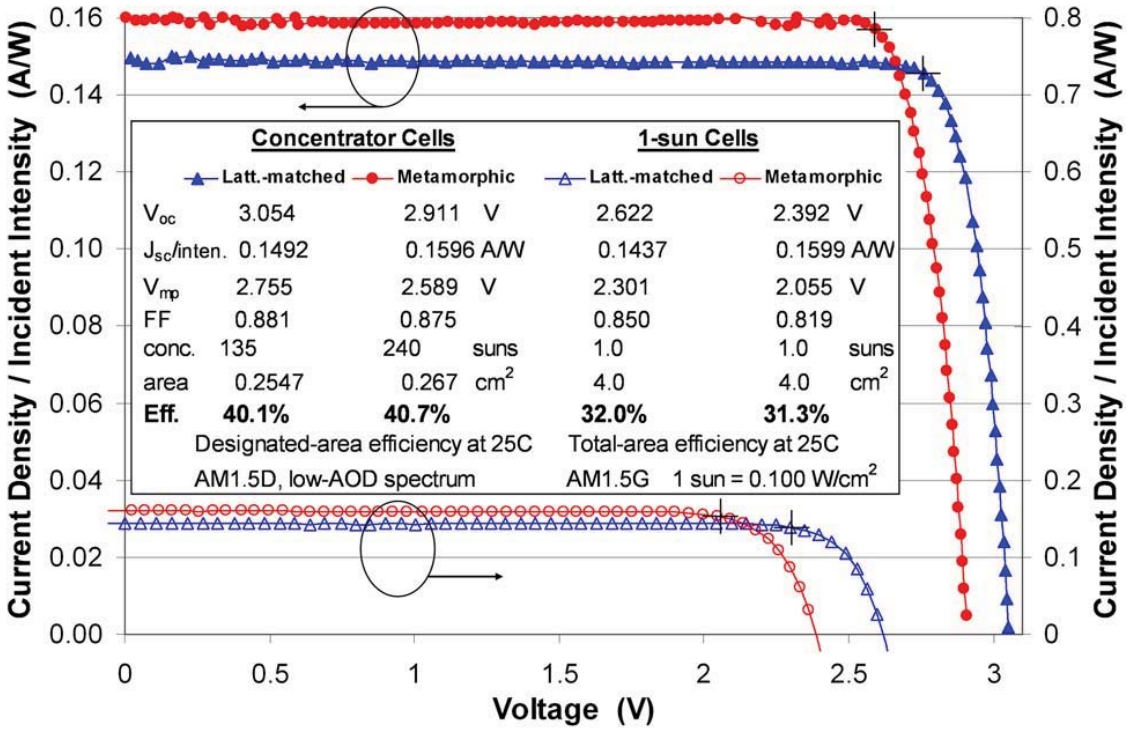

Figure 25. IV Curve [44]

Altogether, it is thus clear that the metamorphic or lattice-mismatched approach to stacking multi-junction cell layers provides a novel method for increasing photovoltaic cell efficiencies beyond previously unreachable levels. Prior to King's experiment, the previous efficiency records had been 39.3% for a metamorphic cell and 39% for a lattice-

matched cell. Despite issues due to losses and manufacturing difficulty, it is clear that industry will continue to develop this technique, potentially in lieu of lattice-matched design. A reasonable argument can thus be made that practical efficiencies of between 45% to 50% may be attained in the near future by utilizing metamorphic multi-junction cells, especially by those which maximize the mismatched effects by having more than the three junctions commonly found in multi-junction cells today [44].

2.3.4 - *Digital Cameras*

Our previous discussion of photovoltaic technology has focused primarily on its applications to electrical energy conversion. However, the technology that has led to increases in solar cell efficiency has also led to advances in other fields, most notably, digital cameras. Digital cameras are ubiquitous today and are found in mobile phones, stand-alone point-and-shoot and digital single-lens reflex (DSLR) cameras, tablet computers, and other devices. In a relatively short time, digital cameras have essentially replaced the film-based cameras which were previously used.

The first digital camera prototype was developed in 1975 by Eastman Kodak scientist Steve Sasson [50], 21 years after the development of the first practical photovoltaic cell at Bell Laboratories [51]. This camera used a charge-coupled device image sensor. Digital cameras take photographs by recording images on an electric image sensor. Image sensors convert optical images to discrete electrical signals that can be immediately displayed on a screen or stored in memory for later use. There are two types of sensors: digital charge-coupled device (CCD) and complementary metal-oxide-semiconductor (CMOS) active pixel sensors.

A CCD is an analog device. Incoming photons are held as small electric charges by the chip. The charge is converted into voltage, pixel by pixel, as they are read off the photo sensor. The additional camera circuitry converts this voltage into digital information. The CCD was invented in 1969 at Bell Laboratories by Willard Boyle and George Smith. It was originally designed to be used as a memory device. In 1971, Bell researcher Michael Tompsett used the CCD to capture images using simple linear devices [52].

The image is projected onto a photoactive epitaxial layer of lightly p-doped Si, using a dopant such as Boron. The transmission region contains an array of capacitors, each of which accumulates a charge. This charge is proportional to the light intensity and is transferred to the closest neighboring capacitor. Finally, the last capacitor of the array transfers all the charge into a charge amplifier. The amplifier converts the charge into voltage, and this process is repeated for the entire array into a series of voltages which are then stored for future use.

A CCD captures 70% of the incident light as compared to the 2% captured by photographic film. CCDs are sensitive to near-infrared light, allowing them to be used for infrared photography and night-vision devices. They also have many uses in astronomy and image scanning. However, the CCD is vulnerable to blooming and vertical smearing.

The CMOS Active Pixel Sensor (APS) was developed by Olympus employee Tsutomu Nakamura and improved upon by American engineer Eric Fossum [53, 54]. In 1995, the technology took off when engineers from the Jet Propulsion Lab in Pasadena, CA founded a company that commercialized APS technology. CMOS Active Pixel Sensor technology is easier to manufacture, has less image lag, and most importantly

consumes less power than CCDs. APS uses the same integrated circuit to bundle sensor and processor functionality, resulting in the need for fewer components. This technology is useful for situations where power management, on-chip processing, and the type of packaging are important. It is also less expensive than CCD technology. CMOS APS technology is not affected by the blooming of light. However, the CMOS APS captures one row of light at a time at a rate of 50-60 times per second. This leads to a rolling shutter effect causing the image to skew. The CCD captures the entire image at once and is also a higher quality image. Altogether, we can see that the same processes which are used for electrical energy conversion in photovoltaic cells are used in the field of digital photography as well.

2.4 - Concentrated Photovoltaic (CPV) Technology

In this section, we will discuss the history and current research of concentrated photovoltaic (CPV) technology. We will discuss the different methods of concentrating light and their effect on CPV systems.

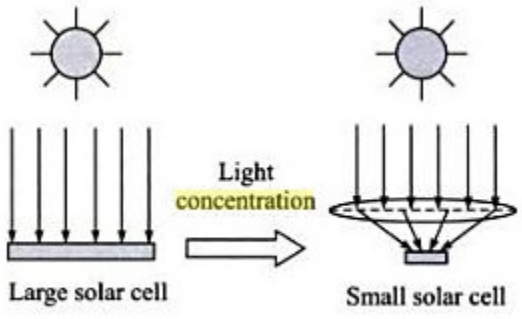

Figure 26. Comparing Non-concentrating cells and Concentrating Cells [55]

By concentrating light onto a smaller surface area, the light intensity incident on a solar cell changes all solar cell parameters, including the short-circuit current, the open-circuit voltage, the fill factor, the efficiency, and the impact of series and shunt

resistances. The light intensity on a solar cell is referred to as the number of suns, where 1 sun is equal to standard illumination at AM1.5, or 1 kW/m^2. For example a system with 50 kW/m^2 incident on the solar cell operates at 50 suns.

In 1975, the United States Department of Energy budgeted $1.25 million for CPV systems research [56]. Sandia National Laboratories began research of CPV technology at the National Solar-Thermal Test Facility at Kirtland Air Force Base in Albuquerque, NM, with the construction of a 1 kW array, known as Sandia I and Sandia II in 1976 and 1977 respectively [57]. The Sandia II array was the first modern photovoltaic concentrator consisting of 5 cm diameter silicon (Si) cells operating on two axes under cast acrylic Fresnel lenses at 32 suns with passive cooling [57]. This research spurred many private and public institutions to work on concentrating systems.

Researchers tried a variety of concentrators, including reflective, refractive, and luminescent concentrators. Researchers as Motorola, RCA, GE, Martin Marietta, E-Systems (later Entech), Boeing, Acurex, and Spectrolab, developed concentrating systems while universities, such as Stanford University, Arizona State University, and Purdue University, were working on fundamental research [56]. In Austin, Texas Entech's 300kW system atop a 3M parking structure proved to be a remarkable demonstration project which applied concentration principles in the United States.

The most notable large-scale CPV project during the 1970s was the 350 kW Soleras Project in Saudi Arabia. Known as the Solar Village Project, this project was designed to provide electricity to remote villages that were not served by an electric power grid. This system proved that a CPV system is capable of completely automatic operation and is designed with stand-alone and cogeneration modes of operation [58].

During the 1980s, there was a boom in oil and natural gas production. Oil prices decreased and concentrator research programs were scaled back [56]. Federal funds became scarce in the 1980s, so in 1990, the Department of Energy (DOE) created the Concentrator Initiative, which comprised of four cell manufacturers – AESC, Spectrolab, SunPower, and Solarex – and four module manufacturers – Entech, Solar Kinetics, Alpha Solarco, and SEA Corp – in order to promote the development of CPV systems to meet the DOE near-term goal of 12 cents per kWh [59]. Gee states that "the continued progress in collector and cell performance and in development of cost-effective designs gives us confidence that photovoltaic concentrator collectors will be the first photovoltaic technology to become cost-effective for utility-scale power plant applications" [59]. However, the Concentrator Initiative was terminated two years after its inception and to this date, concentrated photovoltaic systems have fallen short of prior expectations [56]. Richard Swanson of SunPower Corporation cites that low natural gas prices, the lack of political will, and the inability of the concentrator community to gather sufficient resources to convincingly demonstrate complete system reliability as reasons for the limited commercial success of CPV systems [56]. The success of flat-plate PV modules also gives strong insight into the lack of growth of CPV technology [60].

CPV technology is quite different from flat-plate PV modules which have found a ready market for small, remote power sources. Flat-plate PV applications thrive in circumstances where high reliability and near zero maintenance is necessary [56]. In contrast, CPV units typically come in large module sizes, track the sun during the day, and are suitable for large installations [60].

Concentrators allow a large amount of sunlight to be focused onto a specific surface area. Focusing the sunlight reduces the area of solar cells or modules needed and increases the cell's efficiency [61]. A solar cell's photocurrent increases linearly with the intensity of the light. Simultaneously, photovoltage increases logarithmically with light intensity. Thus, the efficiency of a solar cell increases logarithmically with light intensity, as can be seen in the figure below, until the current increases to the point at which series-resistance losses dominate [62]. As the efficiency is driven upwards, the cost per unit of energy is driven down.

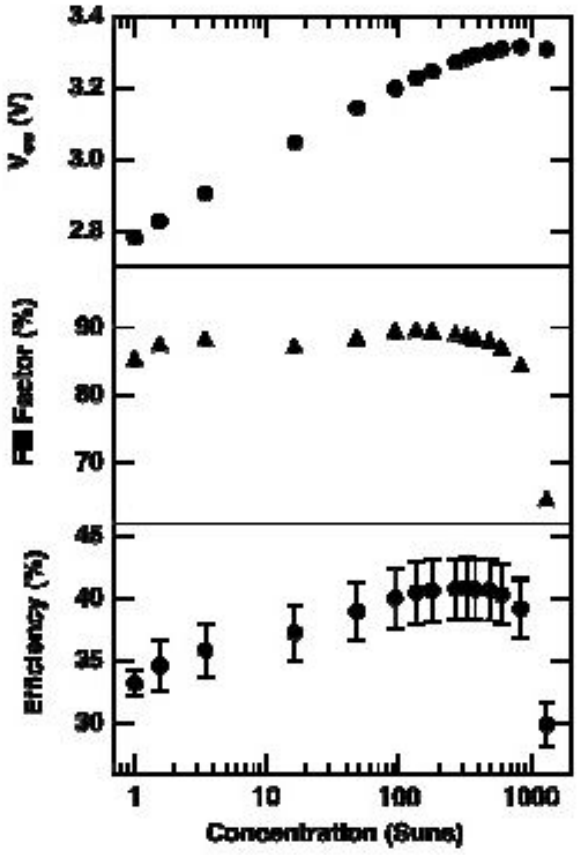

Figure 27. Effect of Concentration on the Open Circuit Voltage (V_{OC}), Fill Factor, and the Efficiency [62]

Typical CPV systems consist of several elements including an optical system, concentrator solar cells, a thermal dissipation system, a casing, and a tracking

mechanism. These elements are typical for CPV systems, but the overall performance of the system depends on how effective each of these elements performs individually and collectively [61]. The optical concentrator, which allows for the sun's energy to be harnessed onto a specific surface area, could come in the form of many different materials, including Fresnel lenses, parabolic troughs or dishes, v-groove mirrors, refractive prisms, luminescent glass, compound parabolic concentrators, or some other optical system.

The Fresnel lens has a plethora of attractive features when used for solar concentration applications. Linear Fresnel lenses may be produced in large sizes; their aspect ratio can be designed to be small, leading to a compact concentrating system; they may be very thin to minimize the cost of optical material and reduce the mechanical load on the supporting structure; and they may be made of reliable and durable material [63]. With advantages like small-volume, light-weight, mass production at low costs and the opportunity to effectively increase the energy density, Fresnel lenses have been used on concentrated solar energy applications since their invention by Augustin Jean Fresnel in 1822 as collimators in lighthouses [64]. This product comes in glass form, polymethlymethacrylate (PMMA) form, or pressure-molded, injection-molded, cut or extruded from a variety of plastics [64]. Fundamentally, a Fresnel lens is nothing but essentially a chain of prisms with each representing the slope of the lens surface without the material of the full body of the conventional singlet [64]. Since the 1960s, Fresnel lens research has focused around imaging and non-imaging Fresnel lens systems. In contrast to a conventional lens, an imaging Fresnel lens refracts light from an object and forms an image in the focal plane which is impacted by aberrations because of the

inaccurate manufacturing of prism tips and grooves. Non-imaging concentrators however have been more widely used because the concentration of solar energy does not demand imaging qualities; Fresnel lenses of non-imaging design are usually of convex shape in order to get a high concentration ratio and flux distribution with a short focal length.

The effect of the chromatic aberration becomes important when using Fresnel lenses. Chromatic aberration is a common optical problem that occurs when a lens is unable to bring all wavelengths of color to the same focal plane, and/or when wavelengths of color are focused at different positions in the focal plane. A perfect lens would focus all wavelengths into a single focal point, yet the refractive index for each wavelength is different in lenses and this fact causes chromatic aberration. Due to the existence of chromatic aberration, degradation of the thermodynamic quality of concentrators is inherent in the quality of concentrated solar energy applications using Fresnel lenses. Lorenzo's research which defined parameters to estimate the degradation by experimenting with different Fresnel concentrators concluded that a concentrator was forced to cast some of the incident energy outside the collector in order to obtain the maximum power. This information on chromatic aberration will be pertinent in the subsequent discussion of concentration.

Parabolic troughs can be used to provide heat for desalination, cooling and electricity generation. This type of collector is built in one dimension and curved as a parabola in the other two dimensions then lined with a polished metal mirror. To construct this system a large financial, structural and materials investment is necessary. In the REACt project, a concrete foundation with ground screws, red pipe mounted for

absorber reflection tests, a light differential sensor, and a plethora of other materials are necessary to set up a system using a parabolic trough collector [65].

The concept for parabolic dishes is an extension of previous work on optimized solar parabolic trough collectors, using elastic bands and compliant bands, in the case of the Harbin Institute of Technology's research on new design approaches for solar concentrating parabolic dishes based on optimized flexible petals [66]. The band shape is optimized by varying its width so that it forms a parabola when its ends are pulled together to a known distance. In this design, the optimized flexible petal concentrator is formed from several optimal-shaped thin flat metal petals through varying petal thicknesses rather than varying petal widths. Since the final result cannot have any gaps between each petal, this idea involves layering the petals of different thicknesses to optimize the parabola. The following graphic demonstrates the concept of optimized flexible petals by illustrating how the different thicknesses of the petal's layers are built to form a parabola.

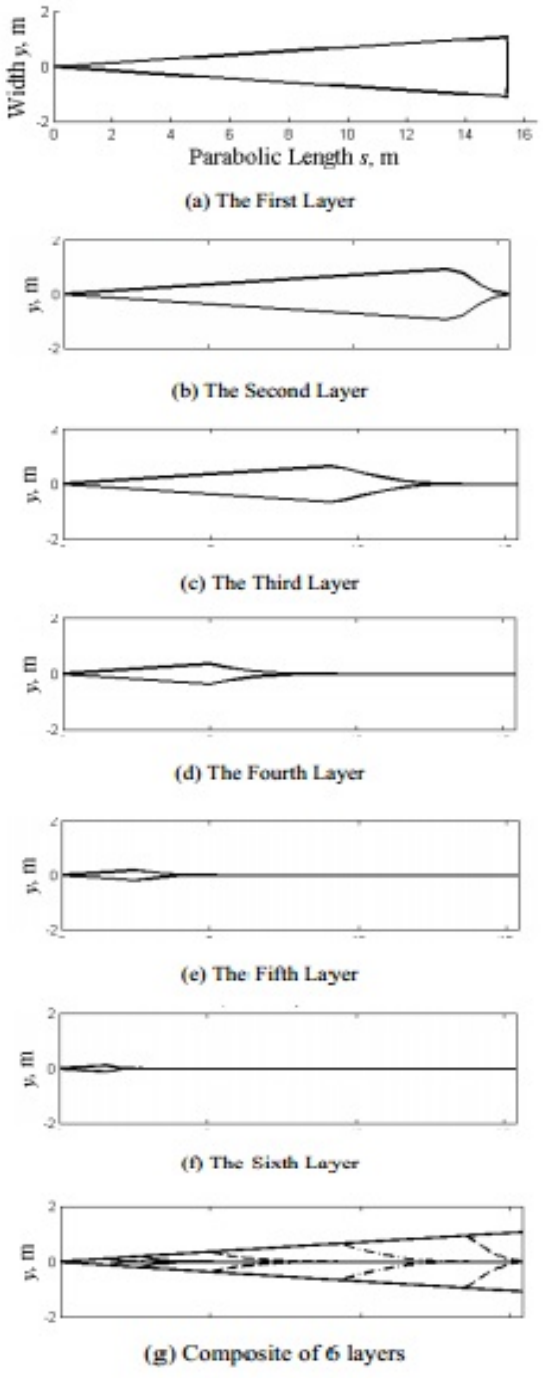

Figure 28. Diagram of Flexible Petals [66]

The design above presented each layer of a six-layered petal separately and then as a composite. With finite element analysis the subsequent figure gives a better view of

the six different layers in the particular optimized flexible petal concentrator discussed in the Harbin Institute of Technology's study.

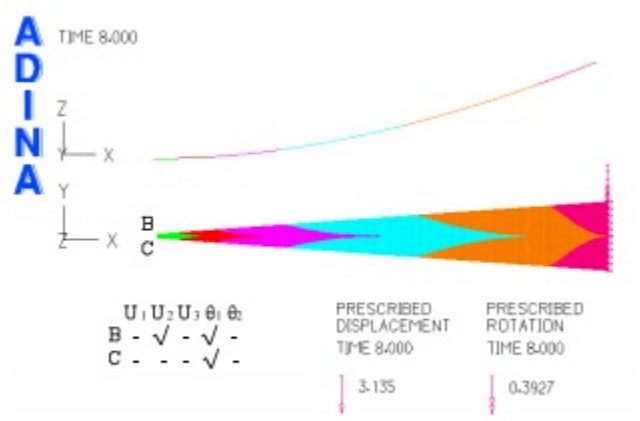

Figure 29. Finite Element Analysis of the Flexible Petal Concentrator [66]

Dishes used to concentrate solar energy reflect the sun's rays onto a solar cell. The concave shape of a dish allows for extreme rays to be reflected back towards a single point known as the focus. Dishes can be created out of many different types of materials and then lined with a mirror film. After the parabolic mirror is created, it directs energy arriving all over its surface to a 'hot spot' at the focus. Parabolic dish concentrators offer the highest thermal and optical efficiencies of all the current concentrator **options**. These systems consist of a parabolic-shaped dish concentrator that reflects solar radiation onto a receiver mounted at the focal point. To be most effective, the parabolic-shaped concentrator needs to focus the sunlight on the receiver and hence the shape of the parabola needs to be relatively precise [66].

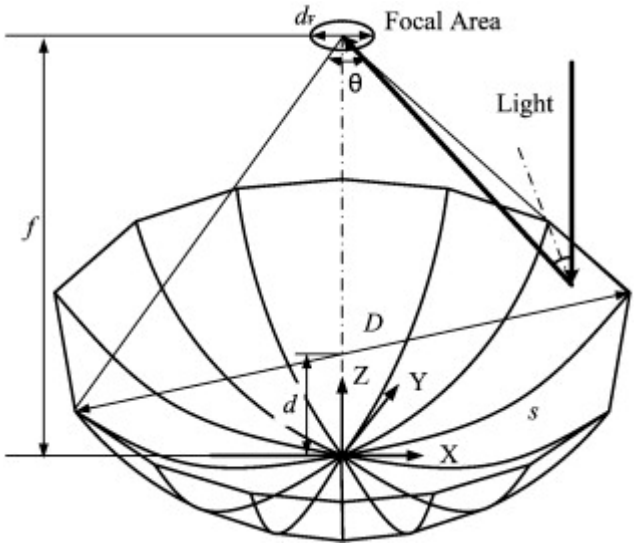

Figure 30. Diagram of a Parabolic Mirror [66]

Luminescent solar concentrators, which can be seen in the figure below, consist of a highly transparent plastic, in which luminescent species, usually organic dye molecules, are dispersed. These dyes absorb incident light and emit it at a red-shifted wavelength, with high quantum efficiency. The figure below shows a schematic 3D view of a luminescent concentrator where AM1.5 light is absorbed by the luminescent particle, and results in luminescence randomly emitted. While some emission falls within the escape cone and is lost, the other emission is guided to the solar cell by the total internal reflection. In some instances, luminescent glass is used instead of plastic which generally consists of transparent polymer sheets doped with luminescent species. LSCs offer potentially lower cost per watt[67] than some other solar concentrators. Unlike standard solar concentrators, luminescent concentrators are able to concentrate both direct and diffused light, without the need for expensive tracking [67].

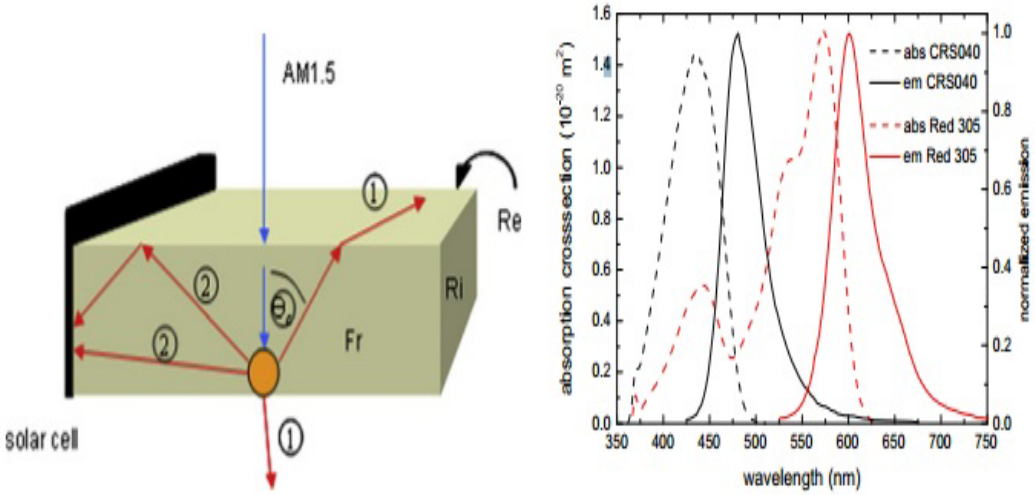

Figure 31. Luminescent Solar Concentrator [67]

Compound parabolic concentrators are an interesting type of concentrator where many companies have already invested into creating models for commercial purchase. This is a non-imaging concentrator that concentrates lights that are not necessarily parallel nor aligned with the axis of the concentrator. Compound parabolic concentrators are made up of two parabolic mirror segments with different focal points.

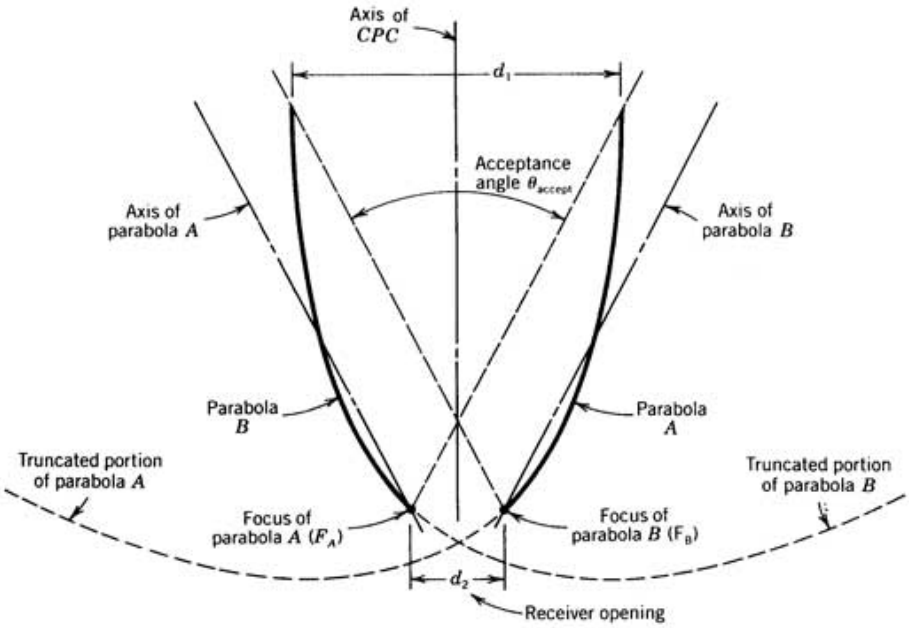

Figure 32. Compound Parabolic Concentrator [65]

The focal point for parabola *A* *(F_A)* lies on parabola *B*, while the focal point of parabola *B* *(FB)* lies on parabola *A*. The two parabolic surfaces are symmetrical with respect to reflection through the axis of the CPC.

The axis of parabola *A* is also shown in the figure above, and this passes through the focal point of parabola *A* while the axis of parabola *B* likewise passes through the focal point of parabola *B*. The angle that the axes of the parabola *A* and *B* make with the axis of the CPC defines the acceptance angle of the CPC. The acceptance angle plays a major role in the concentrating ability of the CPC. While our project does not focus on a compound photovoltaic concentrator, the angle of the light is an integral aspect of concentration.

As previously mentioned, concentrators make it possible to focus large amounts of sunlight onto a smaller surface area. The solar cells used with applied concentration are different from one-sun cells in several ways. The high concentration of solar energy resulting from CPV systems creates advantages including a reduced area of expensive solar cells and increases efficiency. However, solar cells undergo a series of losses as a result of CPV technology.

In each CPV system, there will be a number of losses in the amount of sunlight that will be turned into electricity. These losses are due to the reflection losses in the concentrator and the solar cell, the concentrator geometry, the non-uniform illumination produced by the concentrator, cell temperature, the spectral response of the cell, the cell stringing, the wiring resistance, and the tracking losses. This series of losses can be seen in the figure below.

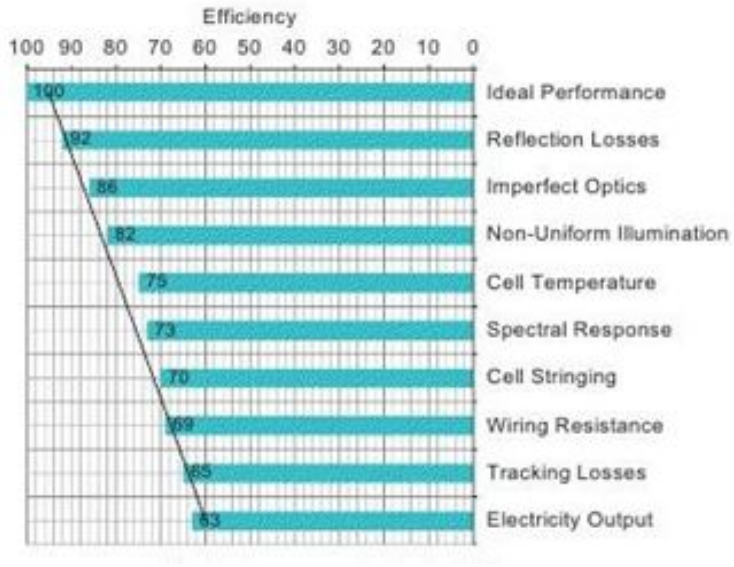

Figure 33. Losses in a CPV System [61]

Ideally a solar cell would have no energy losses; however, ideal performance is reduced by reflection losses from the concentrator and the solar cell initially. While the optical system's objective is to concentrate sunlight and direct it to the solar cell uniformly, some portions of the solar cell are exposed to more light than other portions. This causes a non-uniform flux distribution which is shown in the figure below.

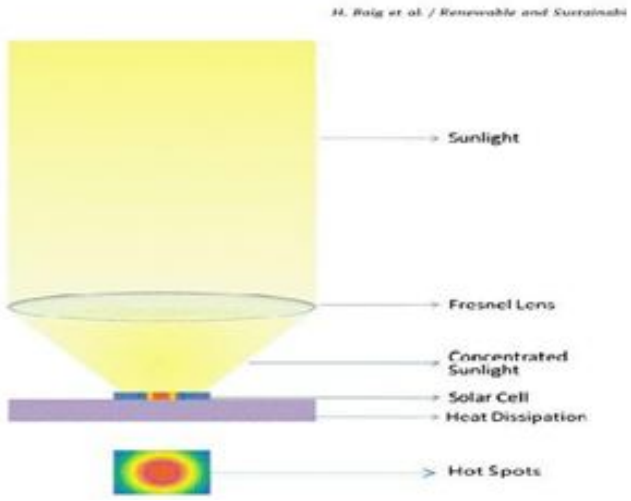

Figure 34. Non-uniform Illumination of a Solar Cell [61]

The non-uniform illumination increases the cell's temperature, cell's resistance, and lowers the efficiency. As a result, when the concentration ratio of the system increases, it becomes more and more difficult to maintain uniformity of the incident flux on the solar cells. In multi-junction cells, almost 37% of the energy absorbed in a solar cell is used for generating electric power and the remaining 63% dissipates in the form of heat. Non-uniformity arises due to reasons related to the concentrator design, the relative position of the solar cell and the sun, and external factors like shading. More specifically, concentrator optics, shape errors in concentrator profile, improper tracking, misaligning of concentrators, mechanical failures and spectral response can result in non-uniformity [61].

2.5 - Thermal Properties of Photovoltaic Cells

In this section, we will discuss the thermal properties of solar cells including the basics of heat transfer and the effects of heat in CPV applications.

There are three different kinds of heat transfer: 1) radiation, 2) conduction and 3) convection. Radiation is the method of heat transfer where matter emits heat in the form of electromagnetic waves or photons. Unlike the following two methods of heat transfer, radiation does not require a medium to propagate the heat transfer [68]. We will not be addressing radiation in this paper because the heat transfer due to conduction and convection far outweighs the heat transfer due to radiation, making it negligible [69].

Conduction is the transfer of energy through matter and in this form of heat transfer, the heat is what is "flowing", not the matter itself. In solids, the heat transfer is due to the vibrations throughout the structure of the material. Conduction works best in

solids for the molecules are rigid and unmoving with respect to the other atoms in the structure, unlike those in liquids or gasses which are free to move. All heat transfer changes dynamically until it reaches its steady-state which is determined by the material itself and the thermal properties of its surroundings. At the steady-state, the temperature gradient across the material is linear, with the hottest point located at the point of transfer. The system can be modeled with the equation:

$$\frac{dQ}{dt} = -k * A * \frac{dT}{dx} \tag{2.5.1}$$

where $\frac{dQ}{dt}$ is the rate of heat transfer, k is the thermal conductivity of the material, A is the cross sectional area of the material, and $\frac{dT}{dx}$ is the temperature gradient oriented in the direction of interest [68].

As can be seen in figure below, in CPV applications, the size of heat sinks should be generally be equal to the amount of concentration being applied to the cell, i.e. a cell with 50x concentration should have a heat sink 50x the area of the cell itself [69].

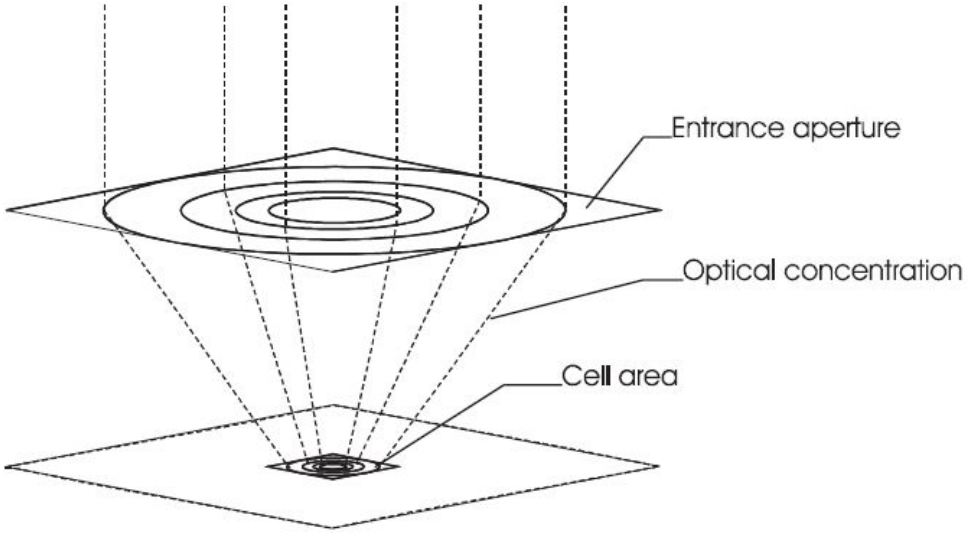

Figure 35. Solar Cell with heat sink [69]

An important aspect of any thermodynamic analysis is the heat transfer coefficient given by the equation $h = q/(T_s - T_\infty)$ (2.5.2) where h is the heat transfer constant, q is the heat flux, T_s is the cell surface temperature, and T_∞ is the ambient temperature. The thermal resistance, R, when used per unit area, is the inverse of h [69].

The last method of heat transfer to be discussed is convection, which is the transfer of heat through random Brownian motion (diffusion) and currents in a fluid, also known as advection. There are two types of convection typically studied and utilized in solar applications. They are natural convection and forced convection. Natural convection relies solely on the buoyant properties of air to cool the cell. As air passes by the surface of the hot cell or heat sink, the heat gets transferred into the air, making the air less dense. This causes the air to flow upwards, allowing it to be replaced by cooler, denser air, which continues the cycle of convection. However, natural convection is most efficient when the surface is oriented vertically and least efficient when the surface is oriented horizontally [70]. The rate of heat transfer can be modeled by the equation $\dot{Q} = hA(T_s - T_\infty)$ (2.5.3) [68].

As can be seen in the figure below, a concentrator cell uses both conduction and convection to cool itself. It is necessary to cool a solar cell for temperature is one of the main limiting factors on performance.

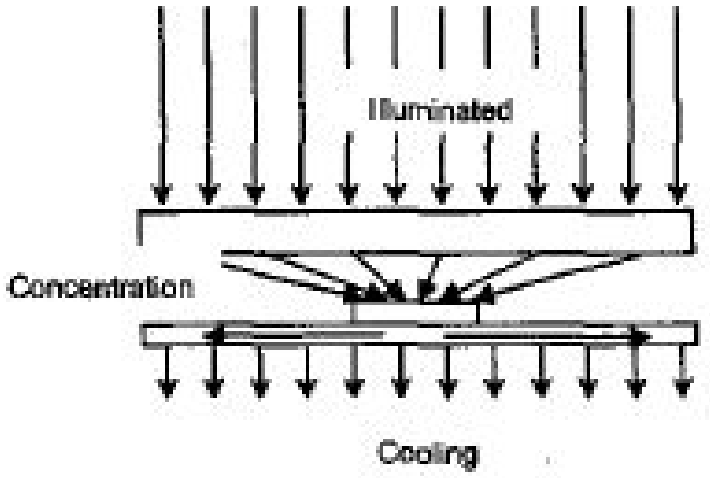

Figure 36. Cooling of a Concentrator Solar Cell [69]

High cell temperatures, as in most technology, are detrimental to the performance of CPV cells, especially when dealing with the conversion efficiency of the cell. The Arrhenius Equation, $t = C * e^{E_a/kT}$ (2.5.4), states that the reaction time of the solar cell depends on the band gap energy, the temperature, and the Boltzmann constant, where E_a is the activation energy, T is the temperature, k is the Boltzmann constant, and C is a constant with units of time. By this relationship, we can conclude that the reaction time, and therefore the degradation time, will be shorter at higher temperatures and lower band gaps. Since the band gaps remain constant in a particular solar cell, higher temperatures directly cause a decrease in the degradation time of the cell [71].

In Padovani's experiment, after a simulated 20 years of testing, the solar cells' short circuit current dropped between 2% and 15% at a temperature of 140ºC [71]. But only six of nineteen cells experienced a drop in voltage. The manufacturer set the maximum operating temperature at 100ºC [71], but by this experiment, it can be concluded that the cells can generally handle more than the maximum set temperature. For every degree Celsius increase in temperature, there is a .3% drop in efficiency [72].

Temperature dependence of the short circuit current is due to the diffusion lengths of the cell. These lengths can be calculated with $L = \sqrt{Dr}$ (2.5.5) where L is the diffusion length, D is the effective diffusion constant, and r is the reflection coefficient of the front face of the cell. The diffusion constant is affected by $T^{1/2}$ so the net effect on L is small. The recombination in the n-type region affected by temperature can be described by $\tau = \tau_{po}[1 + e^{(E_T - E_f)/kT}]$ (2.5.6) where τ is the electron lifetime, τ_{po} is the hole lifetime in a cell where all traps are full, E_T is the energy level of traps, E_P is the Fermi energy level, k is Boltzmann's constant, and T is the temperature. This equation shows that at higher temperatures, the lifetime of an electron is longer so recombination decreases. The recombination in the p-type region affected by temperature can be modeled by $\tau = \tau_{no} + \tau_{po} e^{\frac{E_T + E_F - 2E_i}{kT}}$ (2.5.7) where τ is the hole lifetime, τ_{no} is the electron lifetime, and E_i is the intrinsic energy level. This shows that at higher temperatures, the lifetime of the hole is also longer so recombination decreases further. The band gap decreases as temperature increases, but the change is negligible at temperatures below a few hundred degrees Celsius [73].

The relationship between cell temperature and efficiency is typically linear [69] and can be seen in Figures 37 and 38.

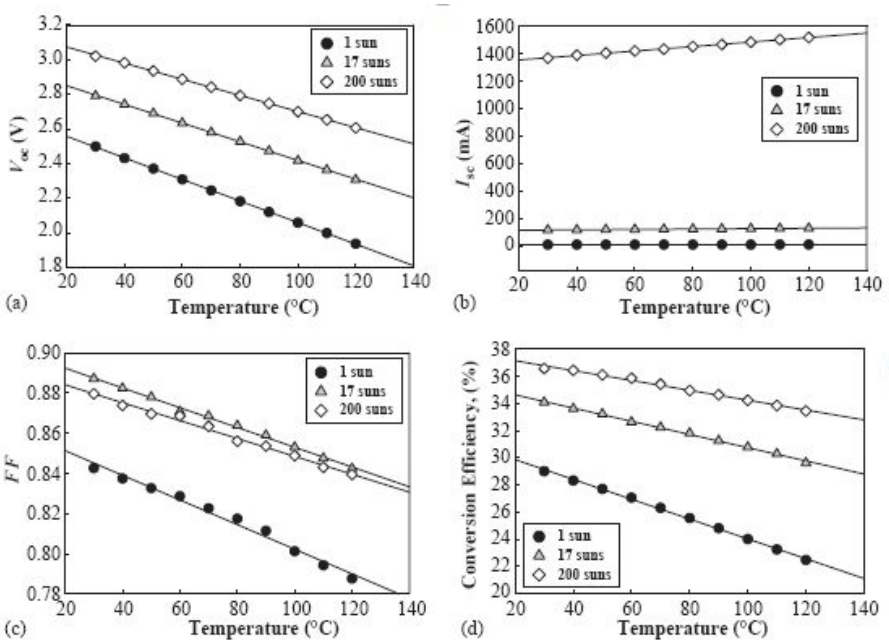

Figure 37. Temperature dependence of characteristics ((a) V_{OC}, (b) I_{SC}, (c) FF and (d) conversion efficiency) of InGaP/InGaAs/Ge triple-junction solar cell [74].

	1 sun	17 suns	200 suns
$\frac{dV_{oc}}{dT}$ [V/°C]	−0.0062	−0.0054	−0.0046
$\frac{1}{V_{oc(25°C)}}\frac{dV_{oc}}{dT}\times 100$ [%/°C]	−0.245	−0.191	−0.151
$\frac{dI_{sc}}{dT}$ [mA/°C]	0.005	0.139	1.637
$\frac{1}{I_{sc(25°C)}}\frac{dI_{sc}}{dT}\times 100$ [%/°C]	7.42×10^{-2}	12.28×10^{-2}	12.02×10^{-2}
$\frac{dFF}{dT}$ [/°C]	−0.0006	−0.0005	−0.0004
$\frac{1}{FF_{(25°C)}}\frac{dFF}{dT}\times 100$ [%/°C]	-7.07×10^{-2}	-5.62×10^{-2}	-4.53×10^{-2}
$\frac{d\eta}{dT}$ [%/°C]	−0.073	−0.0486	−0.0363
$\frac{1}{\eta_{(25°C)}}\frac{d\eta}{dT}\times 100$ [%/°C]	−0.248	−0.141	−0.098

Figure 38. Temperature coefficients of InGaP/InGaAs/Ge triple-junction cell's characteristics (dX/dT: X means V_{OC}, I_{SC}, FF, and η) and temperature coefficients normalized by the same parameter at 25ºC ((dX/dT)/$X_{(25ºC)}$ x 100)) [74]

As can be seen in Figures 37 and 38, efficiency drops as the temperature increases. This is due to the effect that the temperature has on the open-circuit voltage and the short-circuit current. However, this has been shown to be incorrect based on the field data taken by Lee, Ekins-Daukes, et. al. They state that the open-circuit voltage and short-circuit current remain essentially constant no matter the temperature [75]. This claim is contradictory to what most studies have found, either in the field or with empirical studies.

As concentration increases, the rate at which open-circuit voltage decreases with respect to temperature decreases, i.e. as the concentration increases, the temperature has less of an effect on the open-circuit voltage. The rate at which the short circuit current increases in relation to temperature increases, i.e. at higher concentration, the temperature has a greater effect on short circuit current than at lower temperatures [74]. This is because the absorption coefficient increases with higher temperatures. In addition, as the concentration increases, the rate at which the efficiency decreases in relation to temperature decreases, i.e. at a higher concentration, increasing temperature has less of an effect on efficiency. This is because the temperature dependence of the open-circuit voltage is greater than the temperature dependence of the short-circuit current. As can be seen in Figure 38, the normalized short-circuit current dependence is 3 times larger than the normalized open-circuit voltage at 1 sun, but then only about 1.4 times larger at 17 and 200 suns. From the above findings, it can be concluded that it is best to operate a CPV system at a low temperature and a high concentration. However, temperature increases with heat flux because whatever is not converted into electrical energy is given off as heat.

The equation $I - \dot{q}_{rad} - \dot{q}_{conv} - \dot{q}_{cond} - P_{el} = 0$ (2.5.8) states that the solar flux absorbed (I) minus each of the types of heat transfer minus the electrical output must be equal to zero [69].

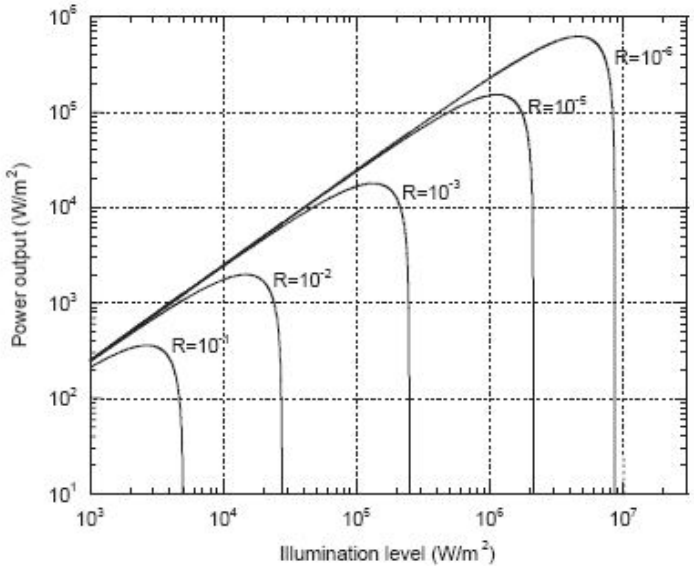

Figure 39. Illumination Level vs. Power Output with varying thermal resistance R [69].

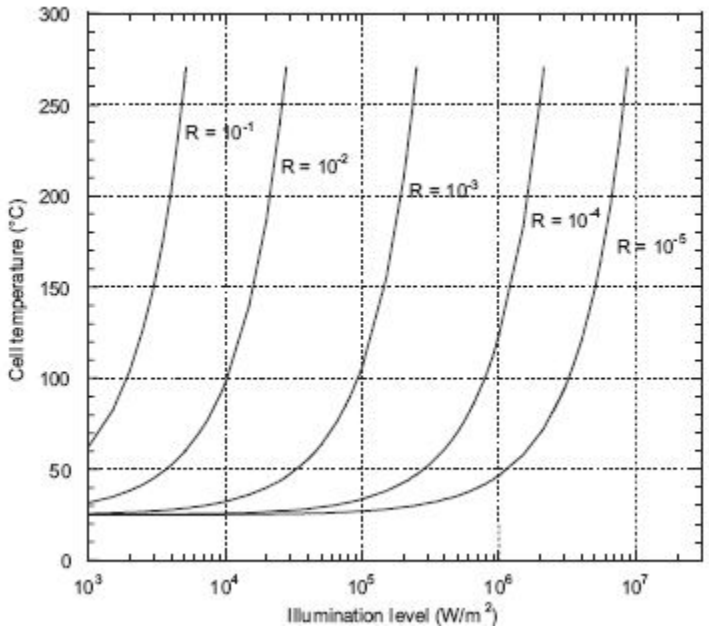

Figure 40. Illumination vs. Cell Temperature with varying thermal resistances [69].

As can be seen in the above figures, the maximum power output occurs at extremely high temperatures, higher than the typical operating temperature of solar cells. It is also necessary to have a low thermal resistance to allow the cell to sufficiently cool.

The Thomson Effect plays a very important role in the operation of a solar cell. The Thomson Effect is where, depending on the direction of the electrical current and temperature gradient, heat is converted into electrical energy of vice-versa. The thermal power per unit volume generated within the cell due to this phenomenon is: $-T\frac{dS}{dT}\nabla Tj$ (2.5.9) where T is the temperature, j is the projection of the electric current density vector onto the direction of the temperature gradient, and S is the Seebeck coefficient of thermoelectric power. If the thermal power per unit volume is positive, the electrical energy of the cell is dissipated into heat. In typical solar cells where the n-type layer is on top of the p-type layer, $\nabla Tj < 0$. Therefore, the sign of $\frac{dS}{dT}$, which is typically a function of the cell material, determines if the term is positive or negative [76].

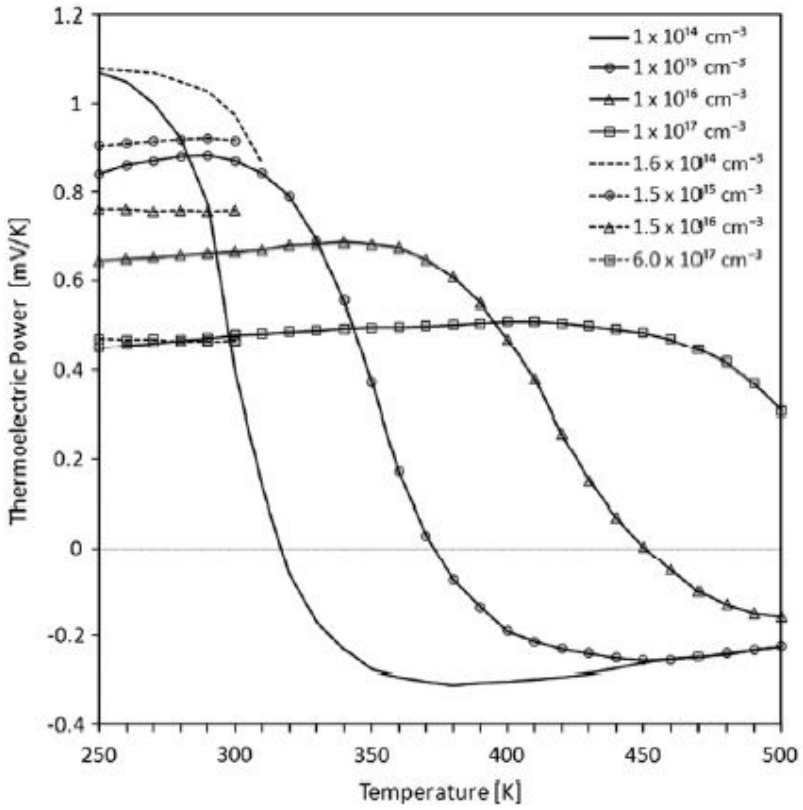

Figure 41. Variation of the Seebeck coefficient of Ge with temperature for several doping levels [76].

The figure above shows that for most temperatures, $\frac{dS}{dT}$ is negative and therefore the thermal power per unit volume would be negative. Since the thermal power per unit volume is negative, heat is actually being converted into electrical energy. However, the Thomson effect is greatest when there is no convective heat transfer. In our experiment, our primary method of cooling is by convective heat transfer. As you can see in the figure below, the Thomson effect has little effect on the efficiency of the cell even when the effect is large [76].

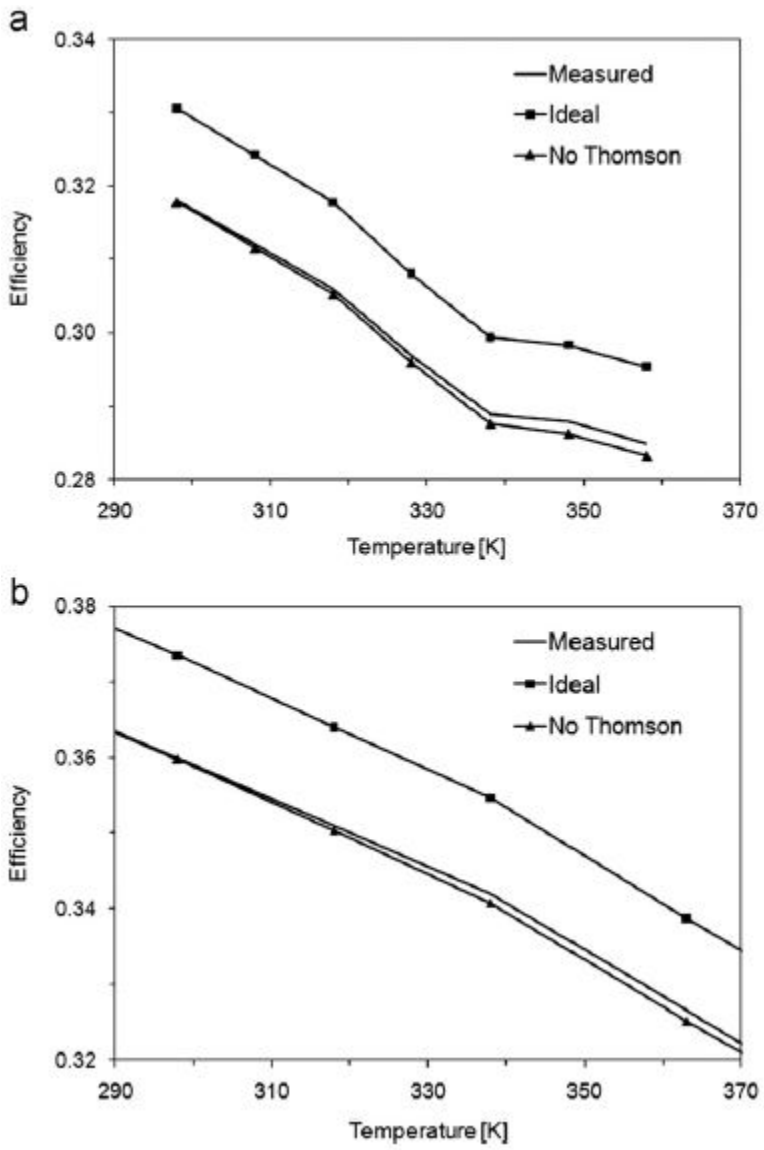

Figure 42. Cell efficiencies vs. temperature: Measured Efficiency, Ideal Efficiency, Hypothetical *No Thomson Effect* Efficiency if the Thomson effect was absent [76].

The Peltier Effect plays another important role in the operation of a solar cell. When a current is passing from one material to another, heat is generated. This heat-generation phenomenon can have an adverse effect in CPV technology because CPV cells are triple-junction cells that allow for multiple locations of heat generation. As can be seen in Figure 43, as the temperature and concentration increases, the changes in the temperature gradient become smaller and smaller. Our experiment is done with

convective heat transfer as our main method of cooling and at high concentrations so the Peltier effect has little effect on our system [77].

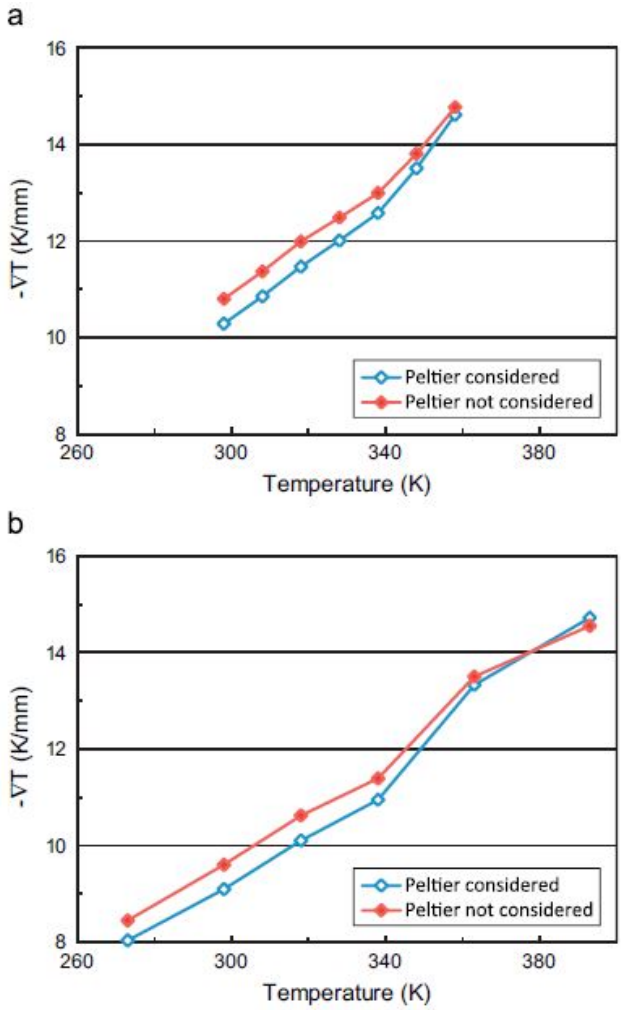

Figure 43. Temperature gradient vs. average cell temperature with the Peltier effect considered and omitted. a) Concentration: 950; b) Concentration: 1000 [77].

In "Temperature Dependence of the IV Parameters from Triple Junction GaInP/GaInAs/Ge Concentrator Solar Cells", the authors examine how the IV parameters (open circuit voltage, short circuit current, etc.) are affected by temperature changes in an outdoor environment. Short circuit current will normally increase slightly with an increase in temperature due to an increase in base diffusion length and a decrease in

absorption band edge energy. However, as can be seen in Figure 44, open circuit voltage will decrease with an increase in dark saturation current, which increases with increasing temperature and decreasing band gap energy. The change of each IV parameter of a multi-junction cell depends on the IV characteristic of each sub cell layer in the stack (i.e. the Ge layer, the InGaP layer, etc. [78])

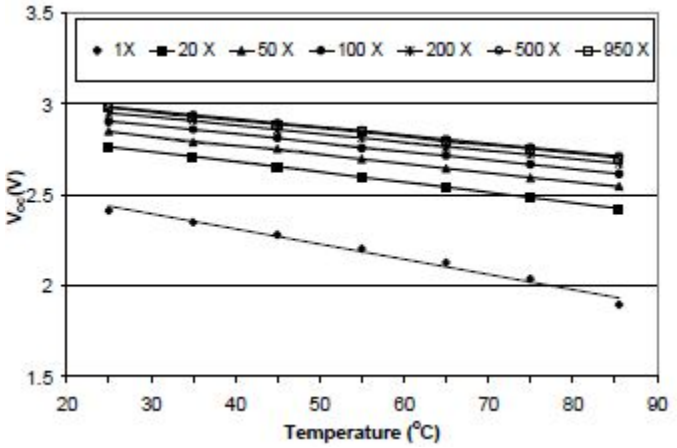

Figure 44. Open Circuit Voltage (V_{OC}) vs. Temperature at Different Concentrations [78]

3 - Methodology

In this section, we will describe our methodology for the construction of our experiment, our data collection set-up, and our data collection procedure.

When our team chose to perform research on concentrated photovoltaic energy, we hoped to understand the relationship between ambient temperature, operating temperature, and insolation. Most current research is done under “flash testing,” where the insolation and operating temperature are controlled and the cell is only exposed to the light for a split second. In this situation, the cell is not tested for a long enough period of time for a differential between ambient temperature and cell temperature to occur. Therefore, the results for the power output, efficiency, and other data are not 100% comparable to operation in an outside environment. We decided to look at the relationship through field testing, the procedure for which will be discussed later. We decided to look at this relationship when the cell was under natural convection. CPV systems often use active cooling systems but these cause parasitic power consumption which reduces overall efficiency [69]. Rather than have the electricity generated be used completely for distribution, some of the electricity goes back into the system for circulating cooling fluid or powering large fans. If natural convection is utilized, then these losses do not occur. We want to find how far you can “push” a cell before it reaches its maximum operating temperature, generally around 100ºC [79].

As an undergraduate research team with limited experience and resources, it was necessary for us to narrow our parameters so that we could achieve meaningful results while still contributing to the field of CPV. To do this, we had to control a number of

variables: the method of heat transfer, the pitch of the solar cell, the concentration, and the number of solar cells used [69].

To control the method of heat transfer, we made sure to utilize only natural convection. This was done by firstly ensuring that the data was collected when wind speeds were minimal, in addition to collecting in an area where wind is often deadened by surrounding buildings. Secondly, we used a sufficiently large heat sink so that the area of the heat sink was equivalent to the maximum concentration. For instance, our cell was 1 cm x 1 cm (.397 in. x .397 in.) and our lens was 11 in. x 11 in. These dimensions mean that the maximum concentration that could be generated was 780 suns. Therefore, the heat sink had to be at least 780 cm^2 or the same size as the lens.

Natural convection functions differently depending on the angle of inclination because the pitch affects the Reynold's Number. Therefore, it is necessary to control the pitch of our heat sink. We decided to take measurements at only one defined position. Because heat transfer is least efficient on a horizontal plate [70], we chose to study convection on a vertical plate. By knowing the cell cools in one setting, we can alter the Reynold's number to get an idea of how the cell would be cooled in other inclinations.

When studying the relationship between ambient temperature, operating temperature, and insolation, it is clear which variables will be independent and which will be dependent. For our research, the ambient temperature and insolation were the independent variables and the operating temperature was the dependent variable. The ambient temperature could not be directly controlled so we had to take measurements year round to get a large range of temperatures. The insolation was controlled by using a

lens to produce a range of concentrations and by knowing the ambient insolation at our location.

Before any data collection could take place, we needed to construct a test rig for our data collection. We decided to collect data in a real-world environment. Most current testing of CPV cells is performed indoors under controlled conditions, and the cell is normally only exposed to light for a fraction of a second, meaning there is no time for the cell to heat up due to the intense light. By taking data outside, we believed that more realistic data points would be collected. The cell is exposed to varying levels of insolation, humidity, ambient temperature, etc. Because each of these factors is out of our control, it was necessary to record data year-round under as many conditions as possible. The only conditions we would not collect in were windy, cloudy, or rainy weather because these conditions would not aid in our understanding of the relationship between ambient temperature, insolation, and operating temperature of the cell under natural convection.

3.1 - Design of Our Apparatus

When designing our apparatus, we first needed to decide how we would mount the cell. Araki et. al. connected their cell to a copper plate using epoxy [70]. We, however, chose to use screws and plastic washers to mount our cell so that the ceramic backing and the copper plate would be in direct contact to maximize the heat transfer between the ceramic and the copper plate.

Secondly, we needed to decide how big our heat sink needed to be. As mentioned above, the heat sink should be sized proportional to the concentration. This allows for the

heat to conduct outwards from the cell to a point where the temperature of the plate is not influenced by the light being concentrated on the cell. Therefore, all heat is eventually dissipated through convection. The lens we chose to use was 11 in. x 11 in. so our copper plate must be at least 11 in. x 11 in.

Thirdly, we needed to figure out how we were going to track the sun so that the concentrated light is always pointed at the cell. To get the most accurate readings, the light had to be normal to the cell. Any error beyond 10º would result in a significant drop in efficiency [6]. Firstly, we considered a design in which hundreds of tiny mirrors would be directed at the cell. This design, however, has a number of flaws. First, those mirrors on the furthest reaches of the mirror array would be greater than 10º off from normal. Second, the array would have to be continually adjusted, and there is no simple way to adjust hundreds of tiny mirrors at once without installing a servo motor on each mirror, which would be far too expensive for an undergraduate project.

Next, we considered using a parabolic mirror. This posed a problem because installing the mirror film inside the dish without creases in the film would be very difficult to do. Those creases would have led to a decrease in the efficiency of the mirror. We then decided to use a lens to concentrate the light onto the cell. In order to keep the cell vertically mounted, we needed a way to direct the light through the lens, normal to the cell. We discovered that the best way to do this was by using an inclined mirror.

The sun needed to be tracked manually and accuracy was not difficult to achieve because the mirror could be tilted up and down to redirect the light in the vertical axis, and the apparatus could be rotated on the ground to redirect the light in the horizontal axis. The light was very easily seen on the plate and by reading the voltmeter, it was

possible to determine when the light was shining directly on the cell. When the voltage reached a maximum, the light was normal to the cell, and therefore, efficiency was at its highest point.

An important factor to consider when constructing the apparatus was that the concentration of the cell must be easily measured. For this reason, we chose a lens with a long focal length. Small changes in the position of a lens with a long focal length will have smaller changes in the concentration than a lens with a shorter focal length. The lens needed to be easily moved and we placed it on tracks so it could slide to the different positions.

Figure 45. Our Test Rig

After construction, we needed to mount the cell and wire the circuit. We chose to use a simple circuit with a cell and a resistor. By knowing the resistance and measuring the voltage, we are able to calculate the current and the power output of the cell.

When calculating the necessary resistance for our circuit, we needed to consider the fill factor of the solar cell.

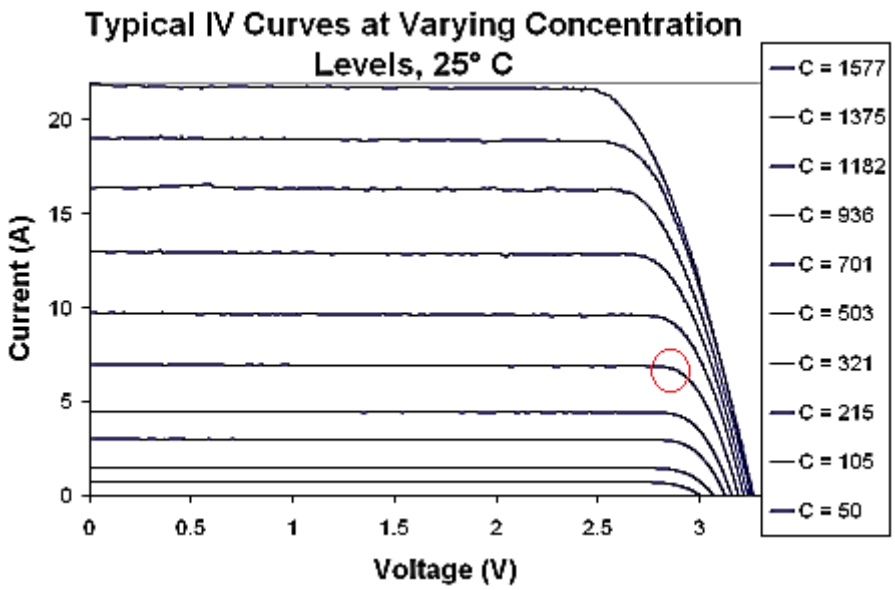

Figure 46. IV Curve of the Emcore Cell [79]

One of the most critical parameters in measuring a photovoltaic cell's performance is the fill factor (FF). This is a ratio comparing the actual maximum power output of a cell to its theoretical maximum power output. The theoretical output is calculated by taking the product of the open-circuit voltage (V_{OC}) and the short circuit current (I_{SC}). Because the power output at both of these points is zero, the actual output of the cell will always be less than the theoretical output and is dependent on the product of the maximum voltage (V_{mp}) and maximum current (I_{mp}) applied. Hence, the fill factor is a ratio less than one which is equal to:

$$FF = \frac{V_{mp} I_{mp}}{V_{OC} I_{SC}} \tag{3.1.1}$$

Figure 46 shows the current versus voltage (IV) curves for the Emcore cell at several different levels of concentration. In this graph, the fill factor can be viewed as the ratio of the area of the largest rectangle which will fit within a given IV curve to the area of the rectangle formed when calculating V_{oc}*I_{sc}. The maximum (top right) point of the rectangle for actual power output falls along the "knee" of the curve, circled in red in

Figure 46, whereas the maximum theoretical point falls above and to the right of the curve.

In our data collection, our average maximum concentration was roughly 500 suns. With two 1Ω resistors in parallel, we worked with a resistance of .5Ω. Given the maximum voltage of 3.2V that we usually achieved, the current for the Emcore cell was thus close to 6.4A, depending on the specific level of concentration. This falls between the fourth (321 suns) and fifth (503 suns) lines from the bottom, corroborating our data collection.

3.2 - Data Collection

The data collection process had to be uniform so that, no matter which team member was recording the data, consistent and valid points would be collected. To establish any sort of protocol, we needed to define which measurements were necessary.

The three key variables we investigated were insolation, ambient temperature, and operating (or cell) temperature. Ambient temperature is necessary for it provides a baseline for the cell to increase from. A cell under the same exact incident solar radiation and concentration will operate at a higher temperature when it is 90ºF outside than when it is 20ºF. Ambient temperature was determined solely by looking at weather.com at the time of the measurement. We considered using an infrared thermometer for this, but depending on the surface, we found vastly different temperatures could be found.

We measured cell temperature with a Fluke 566 infrared thermometer. We chose this method because we believed that any instrument attached to the cell itself would be detrimental to the power output of the cell because some of the cell area would be

blocked. To measure the cell temperature, we pointed the infrared thermometer at the cell and moved the head of the thermometer in the vicinity of the cell. We recorded the maximum temperature as the cell temperature for our analysis.

The final important measurement was the insolation. We measured this by using an MP-100 series pyranometer by Apogee Instruments by pointing the sensor directly at the sun. A pyranometer is an instrument that measures solar radiation flux in watts per square meter. Due to the scale of our apparatus, it was not possible to measure the insolation directly on the cell. Therefore, to calculate the insolation on the cell, we measured the ambient insolation and multiplied by the concentration.

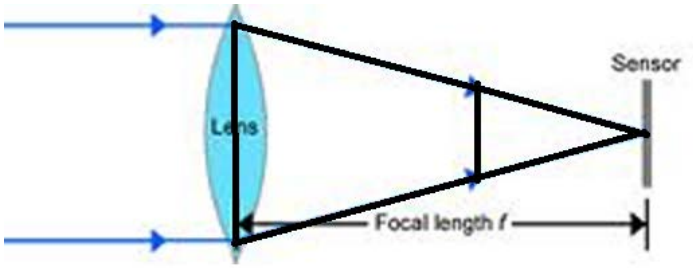

Figure 47. Similar Triangles [80]

Therefore, a fourth measurement was needed to calculate the concentration. This could not be directly measured but could be calculated by knowing the focal length of the lens and the distance the lens was from the cell. As seen in the figure above, the concentration at any point can be calculated using similar triangles and understanding the optics. With a 24 in. focal length and an 11 in. x 11 in. (121 in^2) lens, the image produced at 12 inches would have sides of 5.5 in. x 5.5 in. or an area of 30.25 $in.^2$. Therefore, the concentration would be 4. This process can be used for any position of the lens. The concentration increases exponentially with increasing distance, as shown in the figure below.

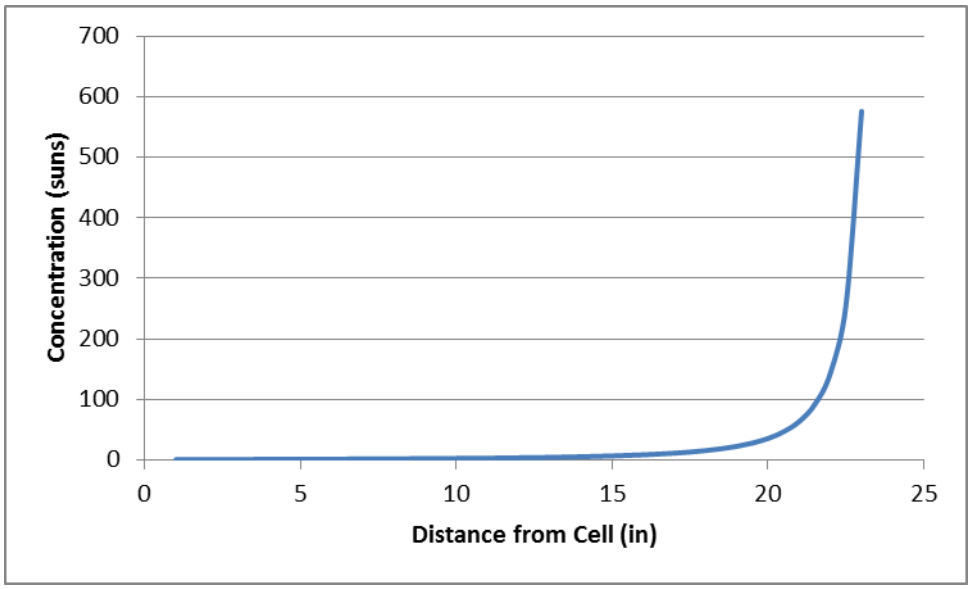

Figure 48. Concentration vs. Distance of the Lens from the Cell

Due to this exponential relationship, it is difficult to be accurate with our calculation of concentration when the cell is beyond 23 inches from the cell. Therefore, the maximum concentration the cell was tested at was 576 suns. Even at 23 inches, there is the possibility for experimental error. A distance of 23.1 inches would produce a concentration of 711 suns, an increase of over 23%. However, we decided to measure at 23 inches so that high concentration measurements could be made.

To calculate the heat flux, which is necessary for our data analysis, we needed to know the power output of the cell. We recorded the voltage and resistance of the cell at each point. The resistance was set at 0.5 ohms for the majority of the data points but the voltage had to be measured with a multimeter.

In addition to these measurements, we made sure to record the date and time of the data collection to ensure we were allowing enough time for the cell to heat up and to ensure we were taking data at various times throughout the year. We also made sure to notice the wind speed for any wind would affect our model of natural convection.

4 - Data Analysis and Results

To analyze our data, we chose to compare our data to a model for heat transfer from a vertical plate by natural convection set out by E.M. Sparrow of the Lewis Flight Propulsion Laboratory, National Advisory Committee for Aeronautics (NACA). His method holds true for laminar free convection from a vertical plate under a constant heat-flux. We chose a constant heat-flux model because a CPV system is operated at a specific concentration and insolation, indicating that there is a constant heat-flux on the cell. The other model used for natural convection is a constant temperature model. Since a CPV system is operated in a variety of different ambient and cell temperatures, a constant temperature heat transfer model would not fit the operational scenario of a CPV system.

4.1 - Fluid Mechanics

To fully understand the properties and equations of convective heat transfer, we must understand the basic concepts of fluid mechanics and the Navier-Stokes equations first. The following equations come from *Fundamentals of Aerodynamics* by John D. Anderson, Jr. unless otherwise cited [81].

The Navier-Stokes equations are equations derived from Newton's Second Law and the conservation of energy, momentum, and mass equations. The equations can be applied to any type of airflow, including both incompressible and compressible flow, as well as steady and unsteady flow. The Navier-Stokes equations are a group of three equations for each direction of airflow. The following equation is for the x-direction and can be changed to obtain the equations for the y- and z-directions:

$$\rho\frac{\partial u}{\partial t}+\rho u\frac{\partial u}{\partial x}+\rho v\frac{\partial u}{\partial y}+\rho w\frac{\partial u}{\partial z}$$

$$=-\frac{\partial p}{\partial x}+\frac{\partial}{\partial x}\left(\lambda\nabla\cdot\boldsymbol{V}+2\mu\frac{\partial u}{\partial x}\right)+\frac{\partial}{\partial y}\left[\left(\mu\left(\frac{\partial v}{\partial x}+\frac{\partial u}{\partial y}\right)\right]\right. \quad (4.1.1)$$

$$\left.+\frac{\partial}{\partial z}\left[\mu\left(\frac{\partial u}{\partial z}+\frac{\partial w}{\partial x}\right)\right]\right.$$

The Navier-Stokes equations are applicable to any type of airflow, but since our model deals with steady, laminar, incompressible flow, some simplifying assumptions can be made. The equation can be simplified to:

$$\rho(\boldsymbol{v}\cdot\nabla\boldsymbol{v})=\nabla p-\mu\nabla^2\boldsymbol{v}\ [82] \quad (4.1.2)$$

With the above equation, as well as information on the boundary conditions, a proper analysis on the airflow can be done.

In fluid dynamics, the stream function, $\psi(x,y)=constant$ (4.1.3), can represent the equation of a streamline. The stream function can be differentiated so that $\frac{\partial\psi}{\partial y}=u$ (4.1.4) and $-\frac{\partial\psi}{\partial y}=v$ (4.1.5) where u and v are the velocity components of the airflow. Sparrow uses this theory in his analysis of laminar free convection

4.2 - “Laminar Free Convection from a Vertical Plate with Uniform Surface Heat Flux”

All equations and information in this section come from E.M. Sparrow’s paper “Laminar Free Convection from a Vertical Plate with Uniform Surface Heat Flux” unless otherwise cited [83].

For his model, Sparrow assumes that a constant heat-flux is supplied to the wall. There are a few boundary conditions that stem from the assumptions made regarding the

fluid dynamics of the system. Due to the viscous nature of air, Sparrow assumed that the velocity at the wall (y = 0) was zero. This is called the “no-slip” condition. As a result of the “no-slip” condition, a boundary layer of thickness δ is created, within which there is a velocity and temperature gradient.

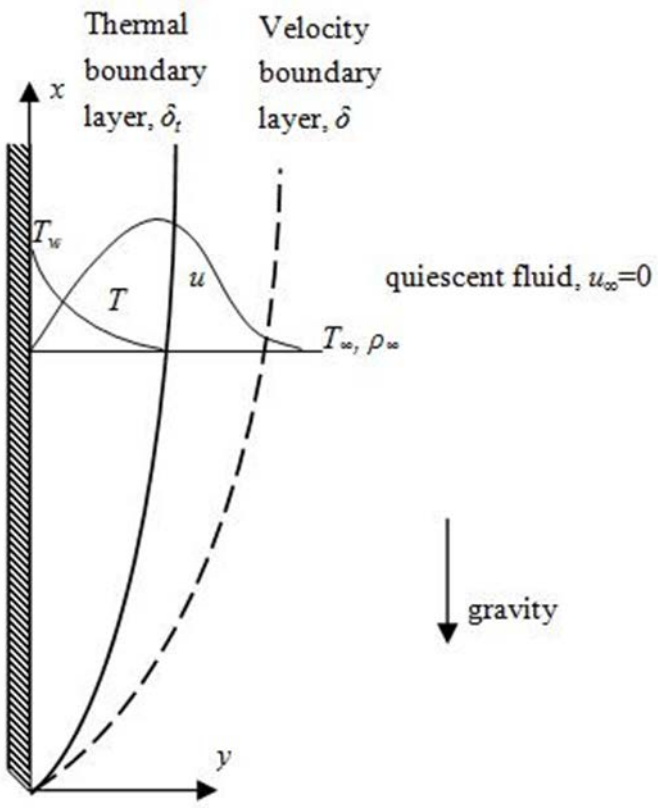

Figure 49. Model of Natural Convection on a Vertical Plate [84]

The above figure displays the heat transfer on a vertical plate while subjected to natural convection. At the wall, the velocity is zero to achieve the “no-slip” condition. The velocity increases along thickness of the boundary layer before returning to zero at the edge of the boundary layer. In a natural convection system, the free stream must be at rest. This system is also laminar due to the small Reynolds number of the airflow. This ensures that there are no turbulent eddies within the boundary layer.

The equations for the conservation of mass, momentum, and energy that Sparrow used in his analysis, are shown below, respectively.

$$\frac{\partial u}{\partial x}+\frac{\partial v}{\partial y}=0 \tag{4.2.1}$$

$$u\frac{\partial u}{\partial x}+v\frac{\partial v}{\partial y}=g\beta(t-t_\infty)+v\frac{\partial^2 u}{\partial y^2} \tag{4.2.2}$$

$$u\frac{\partial t}{\partial x}+v\frac{\partial t}{\partial y}=\alpha\frac{\partial^2 t}{\partial y^2} \tag{4.2.3}$$

Equation 4.2.1 can be solved in terms of the stream function ψ.

$$u=\frac{\partial \psi}{\partial y}, v=\frac{\partial \psi}{\partial y} \tag{4.2.4}$$

Equations 4.2.2 and 4.2.3 can be solved by changing their coordinate system from (x,y) to (x,η) through the following substitutions:

$$\eta=C_1\frac{y}{x^{1/5}} \tag{4.2.5}$$

$$F(\eta)=\frac{\psi}{C_2 x^{\frac{4}{5}}} \tag{4.2.6}$$

$$\theta(\eta)=\frac{C_1(t_\infty-t)}{\frac{x^{\frac{1}{5}}q}{k}} \tag{4.2.7}$$

Where:

$$C_1=\left[\frac{g\beta q}{5kv^2}\right]^{1/5} \; and \; C_2=\left[\frac{5^4 g\beta q v^3}{k}\right]^{1/5} \tag{4.2.8}$$

By combining equations 4.2.4, 4.2.5, and 4.2.6, the velocity components can be derived,

$$u = C_1 C_2 x^{3/5} F'(\eta) \tag{4.2.9}$$

$$v = \frac{C_2}{5x^{1/5}} [\eta F'(\eta) - 4F(\eta)] \tag{4.2.10}$$

where primes indicate differentiation with respect to η.

By evaluating equations 4.2.2 and 4.2.3, Sparrow obtains two differential equations that must be solved simultaneously.

$$F''' - 3(F')^2 + 4FF''' - \theta = 0 \tag{4.2.11}$$

$$\theta'' + \Pr[4\theta' F - \theta F'] = 0 \tag{4.2.12}$$

At the surface, y=0, the horizontal and vertical components of the velocity are zero and at y=∞, the horizontal component of the velocity is zero. The condition of uniform heat-flux at the plate surface, y=0, is imposed by taking $-k(\frac{\partial t}{\partial y})_{y=0} = q$ (4.2.13) where q is a given constant. At y=∞, the temperature must be T_∞, or ambient temperature.

Using equations 4.2.5, 4.2.7, 4.2.9, and 4.2.10, the boundary conditions can be written as the following:

At η=0:

F = 0

F’ = 0

Θ’ = 1

At η=∞:

F’ = 0

Θ = 0

Sparrow used an iterative method to solve for the two remaining boundary conditions, θ(0) and F"(0), until a solution yielded F'(∞) = 0 and θ(∞) = 0. These values are dependent on the Prandtl number of the air.

By evaluating equation 4.2.7 at the surface, η = 0, Sparrow derived the following equation:

$$t_w - t_\infty = -5^{\frac{1}{5}}\theta(0)\frac{qx}{k}\left[\frac{g\beta q x^4}{\nu^2 k}\right]^{-\frac{1}{5}} \tag{4.2.14a}$$

$$t_w - t_\infty = -5^{\frac{1}{5}}\theta(0)\frac{qx}{k}\left[G_{r_x}\right]^{-\frac{1}{5}} \tag{4.2.14b}$$

The term inside the bracket is called the modified Grashof number, which plays a similar role to the Grashof number that is used in the constant wall temperature model of natural convection. The modified Grashof number has been shown to be within 8% of the Grashof number in the constant temperature model. Equation 4.2.14 is the equation that we used to validate our data.

4.3 - Data Analysis

To validate our data, we needed to calculate the expected cell temperature that Sparrow's equation would give us and compare it to our collected value for the cell temperature. We calculated the theoretical cell temperature for the recorded ambient conditions. To do so, we had to make several calculations, including concentration, total radiation at the cell, and total heat flux to the cell.

The first calculation necessary was the calculation to find the concentration of the light at the cell. We were using an 11" x 11" non-imaging Fresnel lens with a 24" focal

length. To calculate the concentration, we used the ratio of similar triangles and derived the equation:

$$Concentration = (\frac{24}{24 - x})^2 \quad (4.3.1)$$

where x is the distance the lens is from the cell. By using this number, we were then able to calculate the total radiation at the cell, in $\frac{W}{m^2}$, by multiplying the incident solar radiation by the concentration and the efficiencies of both the lens and the mirror.

$$Total\ Radiation = Incident\ Radiation\ x\ Concentration\ x\ .93\ x\ .92 \quad (4.3.2)$$

The next parameter we need is the area of the beam. By using the equation $(12 - \frac{x}{2})^2$ we can calculate the area of the beam at the cell. This is necessary because we are assuming that the distance x, the effective length of heat transfer, in equation 4.2.14 is the height of the beam.

The next parameter that we need to calculate is the amount of energy that the system needs to dissipate as heat. To calculate this value, we multiplied the total radiation at the cell by the area of the cell to find the total energy being supplied to the cell. We then subtracted out the energy that was being turned into electricity by the solar cell. The value obtained from this calculation is our assumed heat, Q. To compute the heat-flux, q, we needed to divide Q by the area of the beam. However, since our model has convection on two surfaces instead of one like Sparrow's model, and to account for other modes of heat transfer and discrepancies in our assumed effective length of heat transfer, we needed to reduce q by some factor, r. To optimize this factor, we computed the residual sum of squares of t_{cell} minus the recorded cell temperature and conducted a goal seek analysis to find the value of r that minimized the residual sum of squares. That value was found to be 6.668.

To continue our analysis, we needed to calculate the Prandtl number, Pr, θ(0), the air conductivity, k, and the kinematic viscosity, v, for each data point. Those were computed using the following equations from Holman [85]:

$$\mathrm{Pr} = 0.0000002 * CellTemp - .0002 * CellTemp + .7191 \quad (4.3.3)$$

$$\theta(0) = .3233 * \ln(2.2 * \mathrm{Pr}) - 1.7076 + .0952 \quad (4.3.4)$$

$$k = -0.000000006 * CellTemp^2 + .00003 * CellTemp + 0.0131 \quad (4.3.5)$$

$$\mu = \frac{(0.000001 * CellTemp + 0.0018 * CellTemp + 0.4541)}{3600} \quad (4.3.6)$$

Next, the modified Grashof number needs to be calculated using the following equation:

$$G_{r_x} = \frac{g\beta q x^4}{v^2 k} \quad (4.3.7)$$

The modified Grashof number is calculated for every data point and is used in equation 4.2.14b to calculate the theoretical cell temperature, t_{cell}, under the recorded operating ambient temperature, incident insolation, and lens position.

After calculating the theoretical cell temperature for every set of ambient conditions, we generated a 3-dimensional scatter of Ambient Temperature, On Cell Radiation, and Cell Temperature for both the theoretical model and our collected data points. To calculate the theoretical cell temperature, we used the same ambient conditions we measured in the field. So for each set of ambient conditions, ambient temperature and on cell radiation, we had two cell temperatures, our measured value and the theoretical value corresponding to those conditions. Therefore, we were only concerned with the vertical distance between the two sets of data. That graph can be seen in the Figure 50.

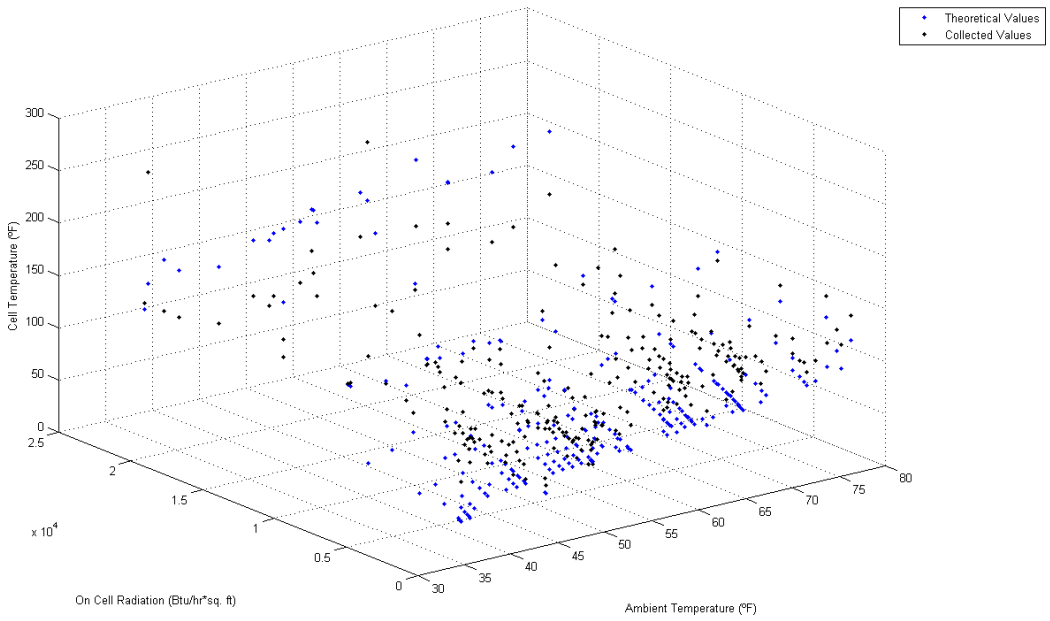

Figure 50. Scatter of Ambient Temperature vs. On Cell Radiation vs. Cell Temperature for both Theoretical and Collected Values

By applying a linear regression to the theoretical data points, a surface can be created that displays the correlation between the ambient temperature, the on cell radiation, and the cell temperature of laminar free convection of a concentrated photovoltaic cell under constant heat flux. The surface can be seen in the Figure 51.

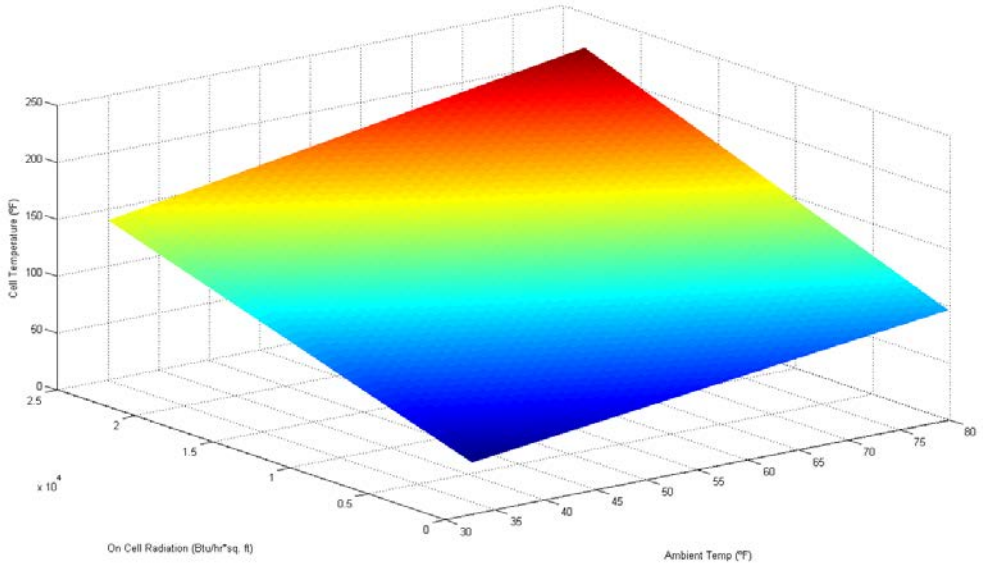

Figure 51. Surface Created from a Linear Regression of the Theoretical Cell Temperature Data Points

4.4 - Discussion of Experimental Error

As can be seen from the above charts, our empirical data does not match our model very closely. This could be due to a number of factors, which will be discussed later. For now, we will discuss how we improved our model so as to fit the data more closely. The primary issue the team had was that the model predicted significantly higher cell temperatures at nearly all concentrations. Looking at Sparrow's equation, any number of variables could be affecting this. θ remains relatively constant for our circumstances, so we deemed it best to leave that be. The thermal conductivity and kinematic viscosity are both well-established properties of air, so changing these values would have been erroneous. The gravitational acceleration and beta are also well-established, so changing these would have been erroneous as well. The value of x we concluded was equivalent to the vertical dimension of the area of concentrated light on the vertical plate. This, based on both the thermal images we captured, was deemed a

close enough approximation. Therefore the heat flux is the only remaining variable that may be altered.

Sparrow's model only deals with laminar free convection on one side of a plate. Our system, however, is convecting on both sides. Therefore, the effective heat flux can, approximately, be divided by a factor of two. This improves how well the model fits our data, but there is still significant error. The team ran a sensitivity analysis on this factor, seeking to optimize the ratio at which the error between our data and the model was smallest. The error was evaluated as the residual sum of squares. The results are outlined in the table below.

Table 1. Optimizing q factor

Factor	Residual Sum of Squares	Average Difference in Temperature (°F)
1	7588347	173.53
2	1975112	88.53
3	956978	61.62
4	652980	50.90
5	548137	46.64
6	515061	45.21
7	511542	45.05
8	520982	45.47
9	536107	46.12
6.668	510731	45.02

As can be seen in the above table, the minimum RSS we achieve is when we divide by a factor of roughly 7. Using the Microsoft Excel Solver Toolkit, the team found that the RSS is minimized when the factor is 6.668. For the rest of the analysis, this value was used.

As can also be seen in the Table 1, this value may have minimized RSS, but the team still experienced an average difference between measured and theoretical values of roughly 45 degrees Fahrenheit. This error could be explained by a number of factors. Firstly, as discussed in the methodology, the concentration was calculated by knowing the focal length of our lens (24 inches) and the distance the lens was from the cell. Using similar triangles, the vertical dimension of the concentrated area could be found, and squaring this number would give the effective area. This results in an exponential relationship between the distance and the concentration, as discussed in the methodology. This opened the team up to the potential for a significant amount of experimental error.

Table 2. Changes in concentration at distances between 22 and 23 in.

Distance (in.)	Concentration	% Change
22	144.00	-
22.1	159.56	10.80
22.2	177.78	11.42
22.3	199.31	12.11
22.4	225.00	12.89
22.5	256.00	13.78
22.6	293.88	14.80
22.7	340.83	15.98
22.8	400.00	17.36
22.9	476.03	19.01
23	576.00	21.00

As can be seen in the above table, when taking measurements at a distance of 22.5 inches from the cell, the concentration is supposed to be 256. If the lens was not perfectly placed, though, the concentration could fluctuate quite a bit. An error of only a tenth of an inch in either direction, between 22 and 23 inches, could result in 13-15% error in the concentration calculation. This type of experimental error may explain the variance in our data at higher concentrations, as well as the efficiency readings that were well above the

39% the Emcore cells are rated for. The efficiency was calculated by dividing the energy output as electricity by the total amount of energy hitting the solar cell.

Another potential cause of experimental error is that the spectral response of the pyranometer did not quite match the spectral response of the solar cell. This would result in differences in the amount of energy we were recording and the actual energy the cell was absorbing.

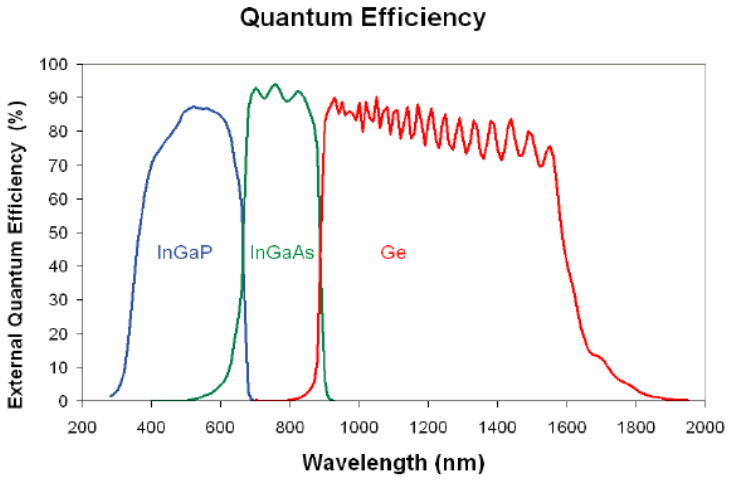

Figure 52. Quantum Efficiency of our Solar Cell [79]

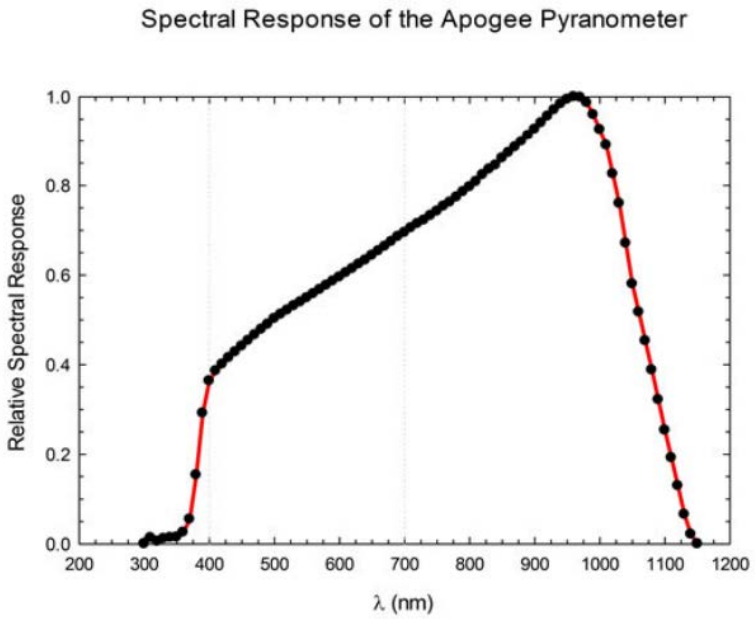

Figure 53. Spectral Response of the Apogee Pyranometer (insert citation) [86]

As can be seen in Figures 49 and 50, the spectral response for the Emcore cell is between about 300nm and 1600nm. The spectral response of the Apogee Pyranometer, though, was about 400nm to about 1100nm. This means that the cell was absorbing light in a range roughly 600nm larger than that of the pyranometer, which would mean the cell was receiving more radiation and functioning at a lower efficiency than we would have determined. This would explain why, especially at higher concentrations, our measured values for the cell temperature tended to be much lower than the modeled values. It is important to recognize, though, that the vast majority of light that is incident on the earth's surface is below 1100nm, as can be seen in the figure below.

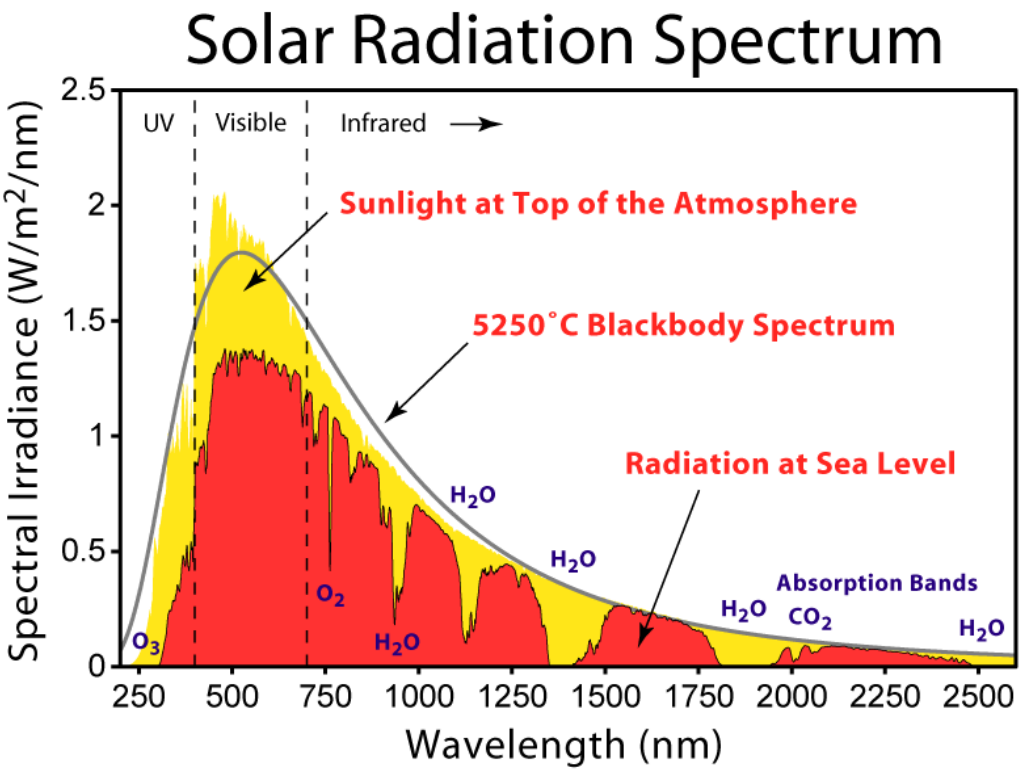

Figure 54. Solar Radiation Spectrum [87]

The pyranometer was able to absorb a significant majority of the light incident on the earth's surface so we can assume that the error due to the difference in spectral

response did not completely explain all error in our measurements, though it may have contributed some error.

Another potential reason for any experimental error was wind. Our project dealt with laminar free convection. Free convection assumes that the air velocity at the boundary layer is zero. Our project, however, took field measurements, causing wind to become a confounding variable. The team tried to minimize the effect of wind by taking measurements only on days that had minimal wind and by performing testing in an area that is generally protected from wind by surrounding buildings. However, this still may not have been enough to completely meet the criteria for “free convection”. This would have contributed to lower temperatures across the board, which is consistent with our data.

We were very fortunate to have Emcore donate 20 triple-junction solar cells. Upon receiving the cells, we decided to study them under a microscope to better understand the cell geometry. What we saw was slightly disconcerting. On the majority of the cells, it appeared that there were score marks across the top layer. We believe that this was most likely a manufacturing defect where solder droplets landed on the cell and were later removed in some fashion. Therefore our cells may not have been operating at their rated efficiency.

However, this should not have contributed to the experimental error much, if at all, because we calculated the actual efficiency that the cell was operating at for each data point. If we had made the assumption that the cell would always operate at the rated 39% efficiency, then there would be an issue, because, as can be seen by our data, the cell rarely ran anywhere close to this value.

Another reason for experimental error is that the team was not sure what the effective heat flux on the cell was. The team was able to measure the insolation and then approximate to the best of our ability the concentration. From that we could calculate the total effective radiation flux on the cell. Multiplying that value by .93 to account for the efficiency of the ReflecTech mirror film and again by .92 to account for the efficiency of the Edmund Optics Fresnel lens better estimates the total effective radiation flux on the cell. The total effective radiation flux can be reduced by the efficiency of the cell to determine the heat flux that must be dissipated. This value, though, is still too high in terms of our model due to reasons outlined earlier, so the flux must be reduced further. Any of these reductions in the effective radiation flux on the cell could have been cause for experimental error.

As stated earlier in this analysis, the effective area over which heat transfer occurred was estimated based on the thermal images we took, as shown below.

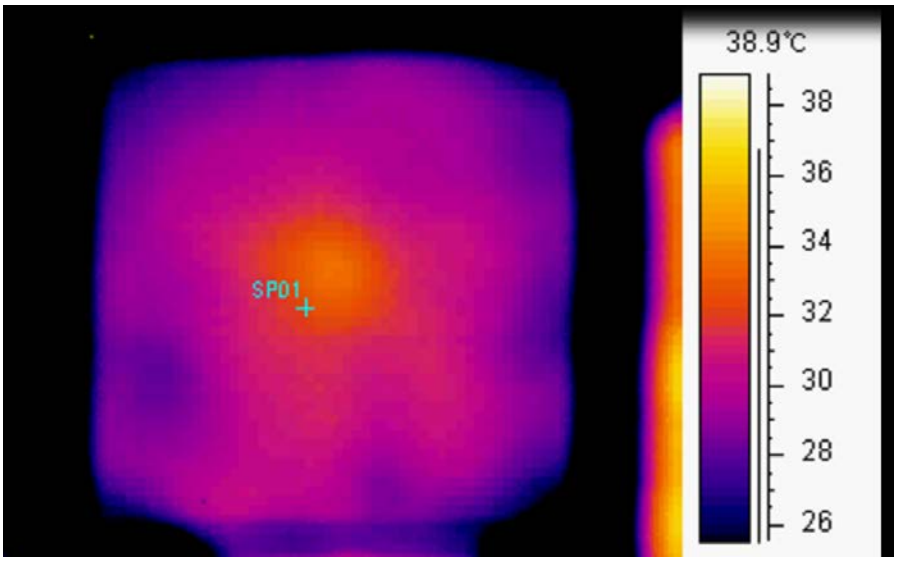

Figure 55. Infrared Image of the Back Side of the Heat Sink

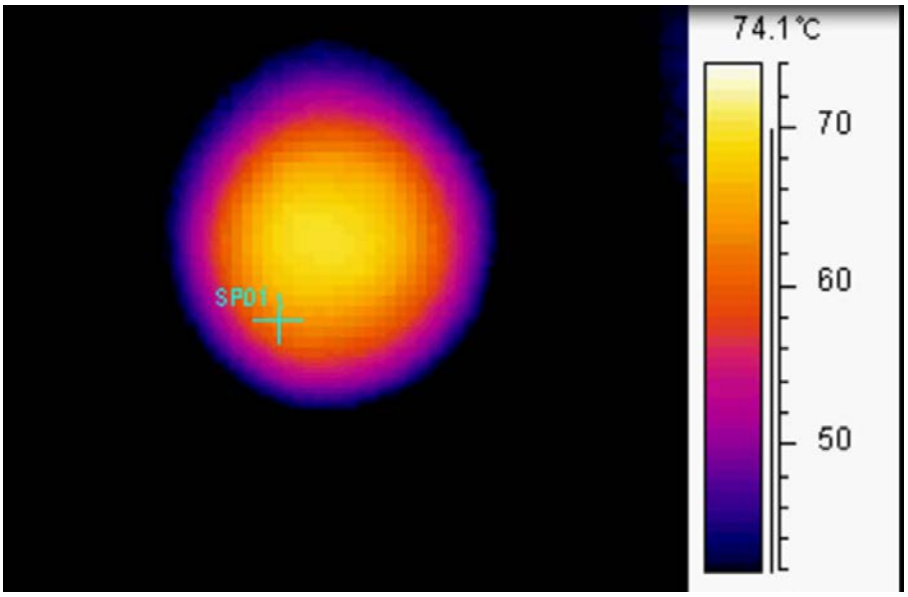

Figure 56. Infrared Image of the Solar Cell

As can be seen in the Figures 55 and 56, the area over which convection occurs is relatively small compared to the size of the plate. Given that the plate is 12in x 12in, we estimated at this concentration that the vertical dimension was roughly 2in x 2in. This, however, was taken at maximum concentration, so the area over which convection occurred would increase as the concentration decreased since light would be contacting the plate over a greater surface area. Using this information and the thermal images above, we estimated that the value for *x* should be equivalent to the vertical dimension of the area over which the light contacts the plate.

This assumption may not have been accurate, though. It may have been invalid to assume that the ratio between area of convection and the area of incident light remained constant for all concentrations; there may have been a non-linear relationship between these two variables. This, therefore, may have been another cause for any error in our experimental data.

5 - Conclusions

The field of concentrated photovoltaic energy is rapidly growing, and it has the potential to make major impacts on the generation of power as our fossil fuels become depleted. However, for CPV to be a feasible alternative in smaller scale applications, further research is necessary on passive cooling techniques. Our paper seeks to add to the body of knowledge in this area by studying free convection on cells. Because of the nature of convection, the angle at which the cell is mounted will affect how well heat convects off the plate. However, convective heat transfer models remain essentially the same for all angles, only being affected by the Reynolds number. Therefore, our model can be extrapolated to be used for any solar cell's pitch. We opted to use a vertical orientation because it is at this pitch that convective heat transfer is most efficient. Therefore, the irradiance on the cell we reach is an absolute maximum, no matter the pitch.

It is our hope that this model can make a significant impact on the body of knowledge of CPV technology. However, this is not to say that our research was perfect. We did have a number of challenges and, in hindsight, there are many things we could have done differently; part of this being due to the limitations on an undergraduate research team.

5.1 - Challenges and Limitations

One area in which our team struggled was the data collection process. Much of this could have run more smoothly, which may have resulted in less variant results. Firstly, our measurement of the cell temperature may not have been accurate for a

number of reasons. The team measured the cell temperature using an infrared thermometer with a laser guide, but at high levels of concentration the laser was not visible. Therefore the team had to approximate the temperature by taking temperature measurements in a line passing through the cell, with the maximum reading being the value that was used. This most likely was not accurate because, as discussed in our model derivation, the temperature increases in the vertical direction. The maximum temperature reading may not have actually been on the cell but above it on the copper plate. It most likely would have been better to use a thermocouple so that the exact location of the temperature reading would be known. Another assumption our model makes is that the heat flux is concentrated on the cell and nothing else. This, however, was only the case at maximum concentration. At lower concentrations, the heat flux is also incident on the copper plate. This would have increased the temperature on the heat sink beyond ambient temperature, affecting the dissipation. The team attempted to counteract this in the model by varying the x value with the concentration, but this is not completely accurate. It would have been better for the team to use something to shield the copper plate from being illuminated, thereby making the cell the only location where the heat flux was incident.

Another area where the team found issue was in making sure all measurements remained consistent. Our testing procedure was as robust as we deemed necessary, but anomalies still arose. The most prominent one was that early on in the data collection our team actually melted a cell off of the ceramic it was soldered to. This was not standard solder, either; the solder used for attaching these cells to the module are normally an alloy made up of copper and silver, which melt at temperatures well over 400 °F. The team had

not done anything differently, yet vastly higher temperatures were being recorded. Only after the cell melted off of the ceramic did we try to figure out the problem. What the team discovered was that the ceramic was not pressed tightly enough against the copper heat sink; therefore the heat was not dissipating, resulting in a much smaller surface area of only the size of the cell for heat to convect. The rate at which heat could be dissipated into the surrounding air was clearly not fast enough to counteract the incoming heat flux. The team also had many instances where procedures may not have been followed perfectly. For instance, on many occasions data measurements were taken in windier conditions, and there were many times where the time between measurements may not have been long enough to achieve equilibrium.

Our team also encountered a number of challenges that realistically had no remedy due to our limitations as an undergraduate research team with minimal resources. Firstly, as has been discussed before, wind was a very important confounding variable. The team had no means to completely eliminate wind without having a lab space that could simulate the various insolations with the same spectrum as the sun. This in no way was within the budget of our team. Secondly, we made the assumption early on that the vast majority of heat transfer would be a result of convection, but in reality a more than insignificant amount of heat dissipation was probably due to radiative heat transfer because we were dealing with such high concentrations. The team, however, had no means of measuring this. The team may have also benefited from an automated tracking system, since manual tracking is not completely accurate. The team did look into purchasing a tracking system, but the prices were well beyond the budget of our team even with an ACCIAC grant.

The team also had challenges when attempting to choose a model. Firstly, there are two separate analyses that could be used: constant plate temperature and constant heat flux. As mentioned before, most papers assume a constant temperature for the cell, so our team opted to focus on a constant heat flux model which would most likely be more appropriate. From there, the team had to determine which model would be best suited for our uses. Sparrow's work, though from the 1950's, has stood the test of time and is the foundation for many other heat transfer models. The team therefore opted to use this model as a basis for our analysis. From there, though, matters became tricky.

Alterations had to be made to the model to fit our uses. As discussed earlier, some of these alterations may have been valid whereas for others, the assumptions made may have been incorrect. This included alterations to the heat flux value. It would have been best for our team if we could have measured the actual heat flux incident on the solar cell, but our pyranometer would have burnt out trying to measure the irradiance on the cell. Even if we did have a pyranometer that could handle such massive irradiances, to measure that would have required blocking the cell. Another assumption we made was in the x value. To know the exact dimension for this variable, we would have needed to be able to perform thermal imaging of the cell, which the team did not have the means of doing. It took significant effort and coordination to perform one session of thermal imaging; to perform over 200 sessions would have been impossible. The x value also could have been validated by placing the plate in a dyed fluid and studying the streamlines, but it would have been impossible to concentrate light onto the cell in this fashion, not to mention that the cell would be destroyed upon submersion.

5.2 - Contributions to Concentrated Photovoltaic Technology

Our research looks at the natural convection cooling of a triple-junction solar cell. In many large CPV systems, cooling mechanisms are used to keep the cells at a low temperature so that the efficiency is not lowered. However, this type of cooling cannot be achieved on a small scale, and doing so would severely hinder the electrical production of the cell. Our research shows how a small scale CPV system would be cooled and that it can be cooled effectively by natural convection.

Our research shows the relationship between the ambient temperature, the on cell radiation, and the cell operating temperature, in an outdoor environment. In the lab, these three key components of a CPV system can be controlled and set to specific conditions. However, this control is not able to be replicated in the field, and so the results of this type of research cannot be considered an accurate model of a real world CPV system. Our research shows how a CPV system would operate in a real world environment.

After showing that Sparrow's model fits the heat transfer of a vertically oriented CPV system, we can make several conclusions about the performance of a similar system under any given ambient conditions and operating conditions. Spectrolab and EMCORE, two of the major concentrator cell manufacturers, list the highest operating temperature of the cell to be 180ºC or 356ºF. If we want to operate the cell at the maximum temperature, which would result in the greatest electrical output, we can back solve Sparrow's model and find the size of lens necessary to operate the cell at the maximum temperature. For our analysis, we assumed a 1 cm^2 area, InGaP/InGaAs/Ge cell and an efficiency of 35%.

For our analysis, we looked at three different regions of the United States, Maryland, New England, and the Southwest, over a range of ambient temperatures, using average maximum insolation values for these areas. In Maryland, the average insolation is 1000 W/m^2, in New England the average insolation is 850 W/m^2, and in the Southwest the average insolation is 1450 W/m^2.

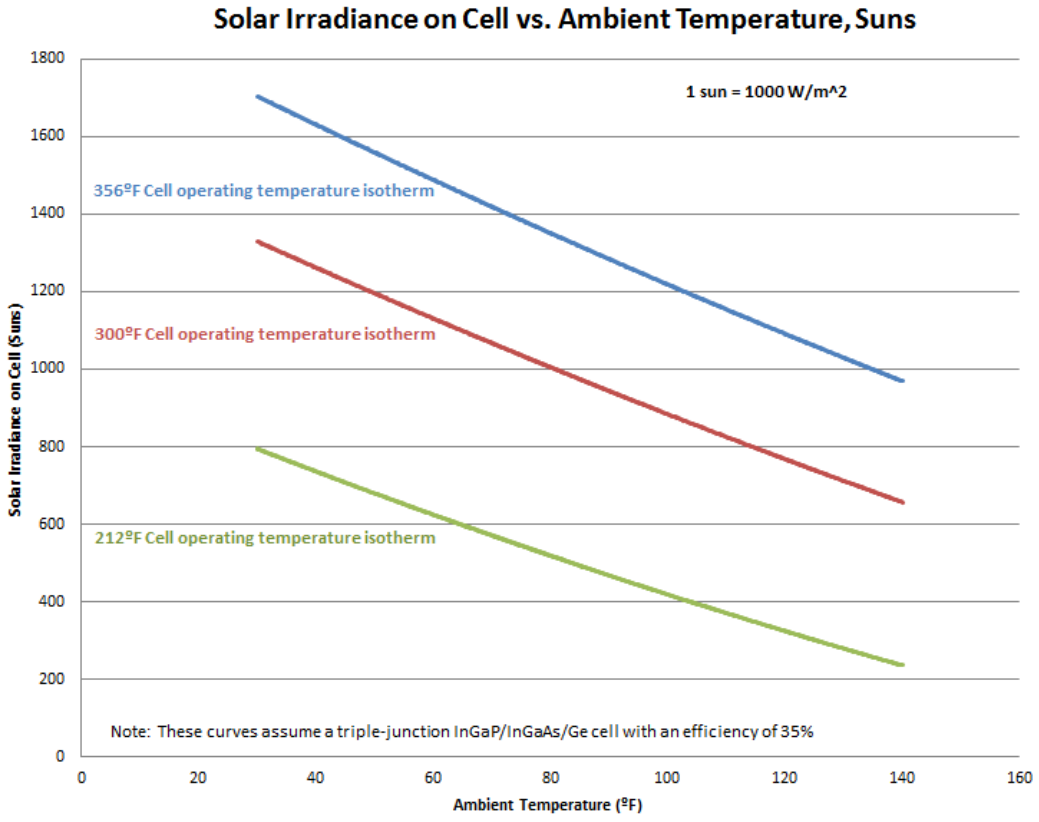

Figure 57. Solar Irradiance on Cell vs. Ambient Temperature, Suns for Various Cell Operating Temperatures

In the above figure, we created three isotherms relating the amount of radiation on the cell in suns and the ambient temperature. One sun is equal to 1000 W/m^2. The top curve shows the maximum amount of suns it is possible to focus onto our cell so that the cell has an operating temperature of 356ºF, for a given ambient temperature. The next two curves show the same relation for an operating temperature of 300ºF and 212ºF respectively. By back solving equation 4.2.14, these isotherms can be found for any given

operating temperature and can be used independently of the size of the cell. However, these above curves are only applicable to a triple-junction InGaP/InGaAs/Ge cell with an efficiency of 35%.

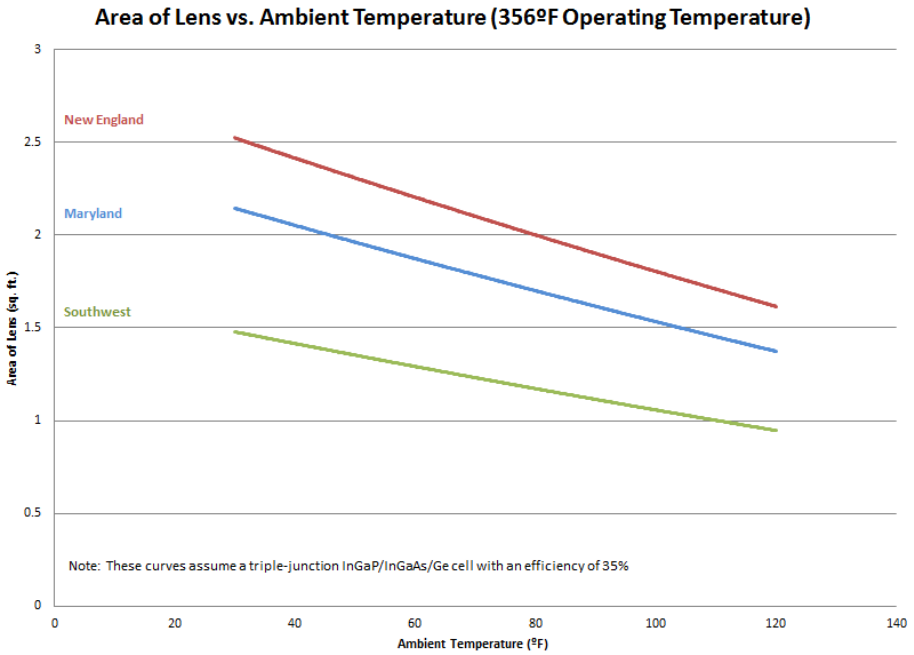

Figure 58. Area of Lens vs. Ambient Temperature (356ºF Operating Temperature)

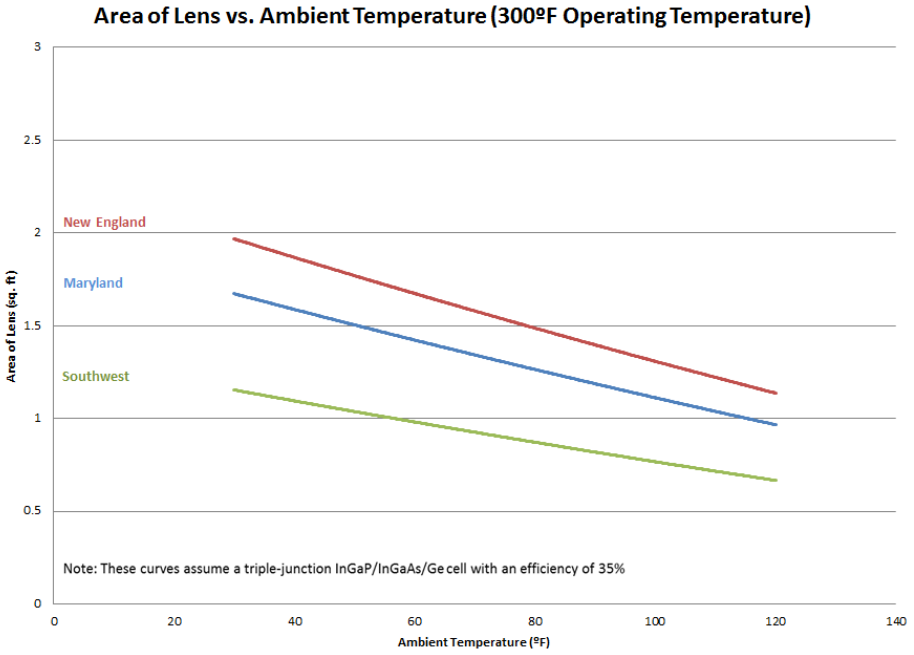

Figure 59. Area of Lens vs. Ambient Temperature (300ºF Operating Temperature)

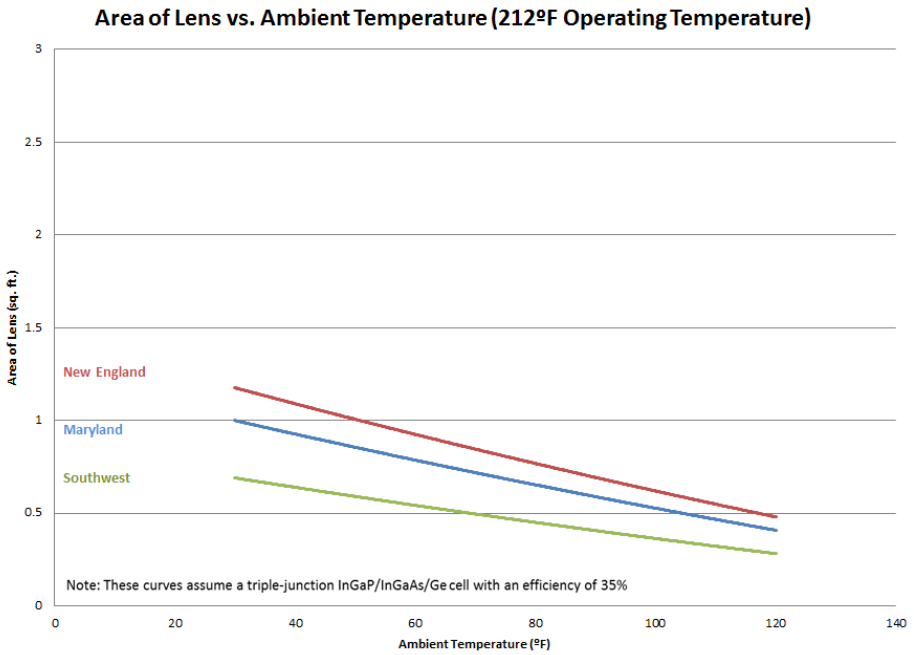

Figure 60. Area of Lens vs. Ambient Temperature (212ºF Operating Temperature)

The above three charts show the relationship between the area of the lens and the ambient temperature in our three specified regions for a specified ambient temperature. As can be seen in the above charts, the lens area is dependent on both the operating temperature and the ambient temperature. With a lower ambient temperature, it is possible to use a larger lens to focus more light onto the cell before it reaches the set operating temperature. These charts show that a CPV system in New England can be just as effective as a CPV system in the Southwest, the only difference between the systems is the size of the lens and Figure 61 depicts our calculated surface that can be used to design a CPV system anywhere in the world.

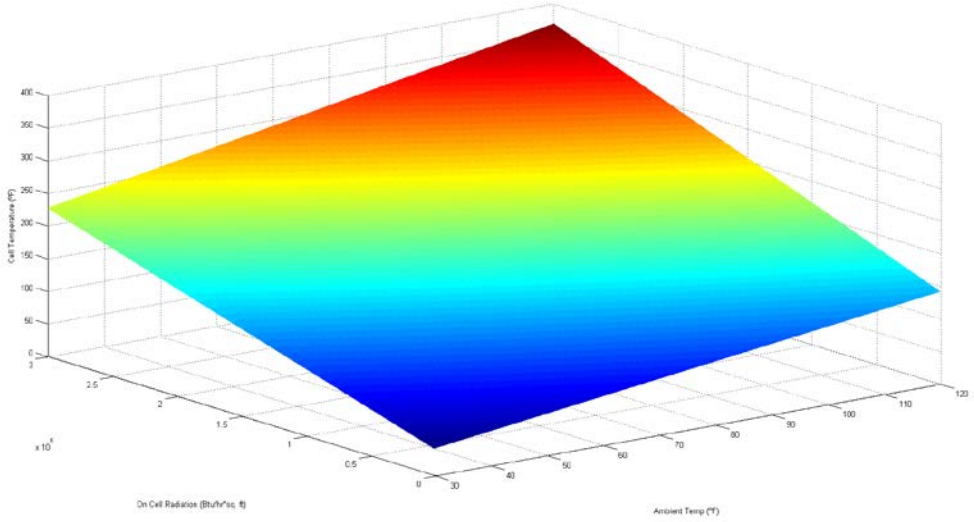

Figure 61. Final MATLAB Surface

5.3 - Further Research

Our model will hopefully make room for great advancements in the CPV industry. There are a number of potential routes that may be taken to either improve or expand upon the research our team has performed over the past three years.

Firstly, as outlined earlier, there were a number of reasons for the variance in our data. Another research project may seek to replicate this experiment while correcting for some of our errors. This could be done by creating a shield that blocks out the wind on all sides, shielding the heat sink so that the only radiation reaching the plate is on the cell, using a more accurate method for measuring the cell temperature, finding an improved way to more accurately measure the concentration, or a combination of the above.

Another project might seek to investigate the validity of our model by comparing it to other existing models for heat flux on a vertical plate. Sparrow's model is not the only existing model, but simply one of the most cited and most established ones. By

comparing results with other models and validating each with experimental data, one might find that another model is better suited for this application.

A project might also seek to determine the proper factor to reduce the heat flux by in our model. As stated earlier, the factor we used of 6.668 is the factor that minimized the residual sum of squares. This is not necessarily the proper way of reducing the heat flux, however our team deemed it to be the best way given what data we had at hand.

A team may want to look at how cell temperature is affected by humidity, cell size, circuit configuration, or any number of other variables. Cell temperature is by no means only impacted by ambient temperature and insolation, so it may be worthwhile to investigate these other variables and the correlation between them and any change in cell temperature.

As discussed in the literature review, temperature can have a huge impact on efficiency. Further research may want to study this relationship more in a field setting and determine whether it is actually worth pushing the cell beyond an operating temperature of 212 °F. This study may find that anything beyond this results in huge losses in output. Efficiency is expected to drop off and most likely be less than the value of 35% that we assumed, but if output still keeps increasing then it may be deemed worth it to keep pushing the cell to higher temperatures.

Finally, and most importantly, it is necessary to validate our model's extrapolations by actually building modules to the sizes outlined earlier and testing them in the southwest, mid-Atlantic, and northeast. In doing so, it may be found that our model does not apply beyond a certain threshold, or that our assumed efficiency was too high and the cells burned out at lower concentrations.

5.4 - Final Words

Concentrated photovoltaic energy has the potential to be a major contributor to power production around the world. Before this can happen, it is necessary to better understand all the issues surrounding it. This includes understanding the energy balance and heat dissipation away from the cells. Team Solar Campus hopes that, with this work, CPV is one step closer to becoming a viable small-scale option in the coming years. Our research has shown that CPV systems can be viable and can be designed to be used anywhere in the world, not just areas with a high incident solar radiation. We hope that this research can be the basis for further research in CPV technology.

Glossary

Absorption

interaction which occurs when p-n junction absorbs a photon

Amorphous

non-crystalline, has small variations in the angles between bonds, usually formed from deposition of gases

Anisotropic Etching

different etch rates in different directions in the material

Aspect Ratio

the proportional relationship between an object's width and its height

Band gap

the amount of energy required to free an electron from its most outer valence shell in order for it to be a mobile electron. A major factor in determining electron conductivity. Also determines what spectrum of light solar cells are able to absorb

Black Body

an ideal thermal radiator

Brownian Motion

the random motion of particles in a fluid resulting from collisions with fast-moving atoms or molecules in the fluid

Carrier (Charge Carrier)

an electron or hole

Carrier Generation

process by which holes are created when electrons gain energy, moving to the conduction band from the valance band

Chromatic Aberration

distortion in which a lens fails to focus all light spectrums onto the same focal point

Composition-graded Buffer

buffer used to lower the dislocation density of lattice-mismatched cells

Conduction

the transfer of energy from high temperature regions to low temperature regions when a temperature gradient exists in a body

Conduction Band

the energy levels at which an electron, upon absorbing this energy, will free itself from its binding atom and move through the atomic lattice

Convection

heat transfer within a fluid due to random Brownian motion and currents within the fluid

Detailed Balance Model

a model by which cell efficiency can be measured

Diffusion Length

the average length a carrier moves between generation and recombination

Diode

a semiconductor device with two terminals, usually allowing the flow of current in one direction only

Doping

to introduce impurities into a pure semiconductor in order to adjust its electrical properties

Electrode

an element in semiconductors that emits, collects and controls the movement of electrons or holes

Electron

subatomic particle with negative electric charge

Electrostatic Potential

the potential difference between two points (i.e. the work needed to move an electron from one point to the other)

Emissivity

ability to release absorbed heat

Energy Level

discrete energy value which a subatomic particle can take on

Fill Factor

the ratio of maximum power output to the product of the open-circuit voltage and short-circuit current

Flash Testing

exposing a solar panel to light for a fraction of a second for purposes of determining the output of the cell. Under Standard Test Conditions, the cell is exposed to 1 sun (1000 W/m^2) at 25ºC and an airmass of 1.5

Grain Boundary

boundaries formed by imperfect crystalline structures

Heat Sink

a passive heat exchanger that aids in dissipating thermal energy to the surrounding fluid by increasing the surface area over which convective heat transfer can occur

Hole

concept describing a position lacking an electron which could have one, thus taking on positive properties

Hydrogenation

the process of adding hydrogen atoms to a molecule usually through plasma deposition which is essential to the improvement of electronic properties of the material a-Si:H = hydrogenated amorphous silicon

Impurity Gettering

the process of removing device-degrading impurities from the active circuit region of a silicon wafer

Insolation

the amount of solar radiation energy a given surface area receives over a specified time

Isoefficiency

method of quantifying efficiency so that it can be scaled and applied to parallel systems

Lattice Matched

cell structure where lattice constants of subcells do matter

Lattice Mismatched

cell structure where lattice constants of subcells do not matter

Metamorphic

cell with lattice-mismatched structure

Multi-junction

cell type that has multiple p-n junctions

One-Dimensional Transport Model

most common model by which cell efficiency can be measured

Open-Circuit Voltage

the maximum voltage attainable by a solar cell, occurring when there is no current

p-n junction

a structure usually found in semi-conducting devices in which a region where most of the electron action takes place; it is formed when two semiconducting materials, one n doped, other p doped are put next to each other

Passivation

the process of adding a coating or shielding to protect a material from corrosion which in turn helps reduce surface recombination

Peltier Effect

the generation of heat as electrical current passes from one material to another; the temperature gradient occurs in the same direction as the electrical current

Photoelectric Effect

the emission of electrons from a material as a result of being struck by photons; it occurs in solar cells, creating an electrical potential.

Photolithography

the etching of special geometries on solar cell surfaces

Photon

the elementary particle that explains how light can act as a particle

Photovoltaic Effect

the creation of an electric current when a material is exposed to light

Planck Radiation Law

law used to describe the radiation emitted by a black body

Polycrystalline

solids composed of multiple crystal structures

Quasi-Fermi Level

number of charge carriers when not at equilibrium

Radiation

the transfer of heat through regions where a perfect vacuum exists (Holman)

Recombination

process by which an electron and hole are eliminated when an electron drops from the conduction band to occupy the spot formerly held by a hole in the valence band

Semiconductor

material with electrical conductivity between that of an insulator and a conductor, basis of modern electronics

Shockley-Read-Hall (SRH)

important type of carrier recombination and generation process

Short-Circuit Current

the current through a solar cell when there is no voltage. For most cells, this is equivalent to light-induced current (i.e. no matter how much light is on the cell, the current remains constant)

Shunting

short circuiting between the front and back surface contacts of a solar cell

Silicon Deposition

a process in which silicon is layered by decomposing silane gas (SiH4), used in thin film silicon solar cells

Spontaneous Emission

interaction which occurs when an electron spontaneously drops to a lower energy level and emits a photon

Staebler-Wronski Effect

the phenomenon in which there is a decline in efficiency in silicon amorphous cells during the first few hundred hours of illumination and then stabilizes, scientists believe it to be caused from density defects in the structure of silicon amorphous cells

Standard Model

see **One-Dimensional Transport Model**

Stimulated Emission

interaction which occurs when an electromagnetic field causes an electron to drop in energy level and take on all properties of the field

Subcell

reference to the individual layers of a multi-junction photovoltaic cell

Substrate

refers to a surface in which materials are layered on, (coatings on a surface)

Sun

unit of insolation, equivalent to 1000 W/m^2 according to Standard Test Condition

Thermalization

process by which subatomic particles reach thermal equilibrium

Thomson Effect

when heat is converted to electrical energy or vice versa, depending on the direction of the electrical current and the direction of the temperature gradient

Transparent conducting oxides (TCO)

degenerate semiconductors with good electrical conductivity and high transparency in the visible light spectrum

Valence Band

the range of energies at which electrons are bound to an atom; exists at a lower energy state than the conduction band

Wave-Particle Duality

the theory that light (and all particles) can behave as both a wave and a particle

Appendix A - Data Tables

Table A1(a) – Distance from Cell: 19in. (Measured Values)

Ambient Temperature (°F)	Insolation (W/m^2)	Voltage (V)	Cell Temperature (°F)
36	990	0.3	167
37	1035	0.28	112
61	1017	0.226	179
43	1030	0.46	60
44	249	0.39	56
50	1042	0.195	78
48	1052	0.25	84.6
50	1067	0.129	73
49	1055	0.134	75
39	1073	0.114	83.5
41	1078	0.168	87
66	1019	0.131	106
42	1037	0.154	88
53	1039	0.143	82
58	980	0.115	97
68	980	0.147	99
73	1005	0.153	99
46	1080	0.181	98
47	1092	0.158	96
62	767	0.052	86
63	1053	0.201	117
62	1143	0.18	108
60	1055	0.157	111
74	1043	0.143	108
66	1125	0.161	126.6
66	985	0.142	110
36	990	0.3	167

Table A1(b) – Distance from Cell 19in. (Calculated Values)

Insolation on Cell (W/m^2)	Power Output (W)	Efficiency (%)
19516	0.09	4.6
20403	0.08	3.8
20048	0.05	2.5
20304	0.21	10.4
4909	0.15	31.0
20541	0.04	1.9
20738	0.06	3.0
21034	0.03	1.6
20797	0.04	1.7
21152	0.03	1.2
21251	0.06	2.7
20088	0.03	1.7
20442	0.05	2.3
20482	0.04	2.0
19319	0.03	1.4
19319	0.04	2.2
19812	0.05	2.4
21290	0.07	3.1
21527	0.05	2.3
15120	0.01	0.4
20758	0.08	3.9
22532	0.06	2.9
20797	0.05	2.4
20561	0.04	2.0
22177	0.05	2.3
19417	0.04	2.1
20502	0.04	1.9

Table A1(c) - Distance from Cell: 19in. (Modeled Values)

Ambient Temperature (°F)	Insolation on Cell (W/m^2)	Measured Cell Temperature (°F)	Predicted Cell Temperature (°F)	Error (%)
36	19516	167	47.48	-71.6
37	20403	112	49.12	-56.1
61	20048	179	74.00	-58.7
43	20304	60	55.58	-7.4
44	4909	56	48.04	-14.2
50	20541	78	63.05	-19.2
48	20738	85	61.02	-27.9
50	21034	73	63.31	-13.3
49	20797	75	62.14	-17.2
39	21152	84	51.70	-38.1
41	21251	87	53.86	-38.1
66	20088	106	79.46	-25.0
42	20442	88	54.52	-38.0
53	20482	82	66.16	-19.3
58	19319	97	70.74	-27.1
68	19319	99	81.15	-18.0
73	19812	99	86.60	-12.5
46	21290	98	59.14	-39.7
47	21527	96	60.32	-37.2
62	15120	86	72.64	-15.5
63	20758	117	76.65	-34.5
62	22532	108	76.56	-29.1
60	20797	111	73.56	-33.7
74	20561	108	88.02	-18.5
66	22177	127	80.50	-36.4
66	19417	110	79.09	-28.1

Table A2(a) - Distance from Cell: 19.5in (Measured Values)

Ambient Temperature (°F)	Insolation (W/m^2)	Voltage (V)	Cell Temperature (°F)
61	1006	0.257	162
50	1038	0.5	57.8
43	980	0.48	73
44	237	0.46	62
50	1011	0.285	81
48	1063	0.28	87.1
51	1055	0.166	80
49	1059	0.172	85
39	1070	0.136	90.1
66	1030	0.168	115
42	1038	0.213	96
53	1045	0.182	84
58	980	0.148	93.6
69	996	0.205	107
73	985	0.209	107
61	1056	0.125	91.6
46	1094	0.224	100
47	1086	0.202	98
65	805	0.12	97
59	1095	0.242	120
61	1205	0.227	112
60	1044	0.215	115.5
77	1005	0.178	116

Table A3(b) – Distance from Cell: 19.5in. (Calculated Values)

Insolation on Cell (W/m^2)	Power Output (W)	Efficiency (%)
24483	0.07	2.7
25262	0.25	9.9
23850	0.23	9.7
5768	0.21	36.7
24605	0.08	3.3
25870	0.08	3.0
25676	0.06	2.1
25773	0.06	2.3
26041	0.04	1.4
25067	0.06	2.3
25262	0.09	3.6
25432	0.07	2.6
23850	0.04	1.8
24240	0.08	3.5
23972	0.09	3.6
25700	0.03	1.2
26625	0.10	3.8
26430	0.08	3.1
19591	0.03	1.5
26649	0.12	4.4
29326	0.10	3.5
25408	0.09	3.6
24459	0.06	2.6
29131	0.06	2.2
23923	0.06	2.7
25384	0.07	2.8

Table A2(c) - Distance from Cell: 19.5in. (Modeled Values)

Ambient Temperature (°F)	Insolation on Cell (W/m^2)	Measured Cell Temperature (°F)	Predicted Cell Temperature (°F)	Error (%)
61	24483	162	75.99	-53.1
50	25262	58	65.12	12.7
43	23850	73	56.96	-22.0
44	5768	62	48.49	-21.8
50	24605	81	64.74	-20.1
48	25870	87	63.20	-27.4
51	25676	80	66.32	-17.1
49	25773	85	64.23	-24.4
39	26041	90	53.66	-40.4
66	25067	115	81.70	-29.0
42	25262	96	56.49	-41.2
53	25432	84	68.31	-18.7
58	23850	94	72.78	-22.2
69	24240	107	84.44	-21.1
73	23972	107	88.48	-17.3
61	25700	92	76.86	-16.1
46	26625	100	61.37	-38.6
47	26430	98	62.36	-36.4
65	19591	97	77.91	-19.7
59	26649	120	75.09	-37.4
61	29326	112	78.53	-29.9
60	25408	116	75.56	-34.6
77	24459	116	92.87	-19.9
66	29131	126	83.65	-33.8
66	23923	114	81.12	-28.8

Table A3(a) - Distance from Cell: 20in. (Measured Values)

Ambient Temperature (°F)	Insolation (W/m^2)	Voltage (V)	Cell Temperature (°F)
35	988	0.6	162
37	1045	0.47	182
54	575	0.12	89
59	620	0.114	98
54	1051	0.343	228
61	995	0.365	117
43	1038	0.425	110
50	1045		55.7
52	1023	0.648	89.2
43	960	0.805	75
50	1116	0.36	90
48	1053	0.39	87.2
51	1053	0.208	75.6
49	1067	0.226	81
39	1078	0.171	103
40	1080	0.28	94.1
66	1035	0.215	117
42	1043	0.285	92
52	1045	0.272	89
59	1011	0.2	96.5
69	999	0.263	115
73	1008	0.273	107
61	1067	0.158	97.8
46	1093	0.288	98
47	1092	0.277	104
65	901	0.13	88
59	1060	0.445	123
61	1238	0.28	115
60	1063	0.294	122.4
76	1016	0.228	118
66	1169	0.22	132.2

Table A4(b) - Distance from Cell: 20in. (Calculated Values)

Insolation on Cell (W/m^2)	Power Output (W)	Efficiency (%)
30,432	0.36	11.8
32,188	0.22	6.9
17,711	0.01	0.8
19,097	0.01	0.7
32,372	0.12	3.6
30,648	0.13	4.3
31,972	0.18	5.6
32,188	0.00	0.0
31,510	0.42	13.3
29,570	0.65	21.9
34,375	0.13	3.8
32,434	0.15	4.7
32,434	0.09	2.7
32,865	0.10	3.1
33,204	0.06	1.8
33,266	0.16	4.7
31,880	0.09	2.9
32,126	0.16	5.1
32,188	0.15	4.6
31,140	0.08	2.6
30,771	0.14	4.5
31,048	0.15	4.8
32,865	0.05	1.5
33,666	0.17	4.9
33,635	0.15	4.6
27,752	0.03	1.2
32,650	0.40	12.1
38,132	0.16	4.1
32,742	0.17	5.3
31,294	0.10	3.3
36,007	0.10	2.7
30,740	0.12	3.9
32,095	0.10	3.2

Table A3(c) – Distance from Cell: 20in. (Modeled Values)

Ambient Temperature (°F)	Insolation on Cell (W/m^2)	Measured Cell Temperature (°F)	Predicted Cell Temperature (°F)	Error (%)
35	30432	162	50.55	-68.8
37	32188	182	53.40	-70.7
54	17711	89	65.23	-26.7
59	19097	98	71.11	-27.4
54	32372	228	71.60	-68.6
61	30648	117	78.70	-32.7
43	31972	110	60.10	-45.4
52	31510	89	69.60	-22.0
43	29570	75	59.11	-21.2
50	34375	90	68.77	-23.6
48	32434	87	65.78	-24.6
51	32434	76	69.06	-8.7
49	32865	81	67.08	-17.2
39	33204	103	56.33	-45.3
40	33266	94	57.47	-38.9
66	31880	117	84.57	-27.7
42	32126	92	59.16	-35.7
52	32188	89	69.95	-21.4
59	31140	97	76.91	-20.3
69	30771	115	87.21	-24.2
73	31048	107	91.58	-14.4
61	32865	98	79.82	-18.4
46	33666	98	64.12	-34.6
47	33635	104	65.16	-37.4
65	27752	88	81.69	-7.2
59	32650	123	77.43	-37.1
61	38132	115	82.10	-28.6
60	32742	122	78.57	-35.8
76	31294	118	94.81	-19.7
66	36007	132	86.40	-34.6
66	30740	118	84.03	-28.8

Table A4(a) - Distance from Cell: 20.5in (Measured Values)

Ambient Temperature (°F)	Insolation (W/m^2)	Voltage (V)	Cell Temperature (°F)
54	575	0.14	100
59	710	0.275	120
54	1010	0.43	251
43	1033	0.638	117
50	1047	1.172	60
52	1055	0.878	89.5
43	971	0.97	59
50	1071	0.46	79
48	1064	0.53	97.5
52	1057	0.29	90
49	1087	0.312	86
39	1075	0.26	101.2
66	1036	0.349	118
42	1042	0.405	93
52	1047	0.356	87
59	940	0.228	98.6
69	1000	0.364	117
73	1013	0.374	111
61	1062	0.226	101.3
46	1098	0.326	96
47	1092	0.411	101
59	1089	0.464	127
61	1274	0.42	108
60	1060	0.415	128.8
78	1101	0.401	123
66	1166	0.311	132.7
66	996	0.356	124
63	1049	0.308	132.7

Table A5(b) - Distance from Cell: 20.5in. (Calculated Values)

Insolation on Cell (W/m^2)	Power Output (W)	Efficiency (%)
23,133	0.02	0.8
28,564	0.08	2.6
40,633	0.18	4.6
39,989	0.16	3.9
41,558	0.41	9.8
42,122	1.37	32.6
42,443	0.77	18.2
39,064	0.94	24.1
43,087	0.21	4.9
42,805	0.28	6.6
42,524	0.17	4.0
43,731	0.19	4.5
43,248	0.14	3.1
41,679	0.24	5.8
41,920	0.33	7.8
42,122	0.25	6.0
37,817	0.10	2.7
40,231	0.26	6.6
40,754	0.28	6.9
42,725	0.10	2.4
44,173	0.21	4.8
43,932	0.34	7.7
43,811	0.43	9.8
51,254	0.35	6.9
42,645	0.34	8.1
44,294	0.32	7.3
46,909	0.19	4.1
40,070	0.25	6.3
42,202	0.19	4.5

Table A4(c) - Distance from Cell: 20.5in. (Modeled Values)

Ambient Temperature (°F)	Insolation on Cell (W/m^2)	Measured Cell Temperature (°F)	Predicted Cell Temperature (°F)	Error (%)
54	23133	100	67.50	-32.5
59	28564	120	75.18	-37.4
54	40633	251	74.44	-70.3
43	41558	117	63.45	-45.8
50	42122	60	71.39	19.0
52	42443	90	73.67	-17.7
43	39064	59	62.62	6.1
50	43087	79	71.94	-8.9
48	42805	98	69.53	-28.7
52	42524	90	73.83	-18.0
49	43731	86	71.08	-17.4
39	43248	101	59.84	-40.9
66	41679	118	88.36	-25.1
42	41920	93	62.63	-32.7
52	42122	87	73.66	-15.3
59	37817	99	79.35	-19.5
69	40231	117	90.93	-22.3
73	40754	111	95.44	-14.0
61	42725	101	83.58	-17.5
46	44173	96	67.92	-29.3
47	43932	101	68.87	-31.8
59	43811	127	81.67	-35.7
61	51254	108	87.03	-19.4
60	42645	129	82.27	-36.1
78	44294	123	102.23	-16.9
66	46909	133	90.51	-31.8
66	40070	124	87.64	-29.3

Table A5(a) - Distance from the Cell: 21in. (Measured Values)

Ambient Temperature (°F)	Insolation (W/m^2)	Voltage (V)	Cell Temperature (°F)
68	955	0.61	116
34	980	1.08	208
36	1039	0.91	177
54	610	0.24	102
59	690	0.41	137
54	384	0.112	143
43	1044	0.75	133
50	1049	1.685	57.6
52	1044	1.61	92.4
43	950	1.3	68
53	1024	0.585	94
48	1071	0.77	93.5
52	1050	0.369	110
49	1086	0.509	96
39	1069	0.366	102.7
66	1036	0.544	120
42	1045	0.597	95
54	1046	0.502	90
59	950	0.308	101
69	1000	0.505	113
74	995	0.527	120
61	1054	0.328	102
46	1093	0.535	99
47	1093	0.606	105
59	1095	0.765	130.5
62	1267	0.52	112
60	1061	0.602	132.1
80	945	0.433	130
66	1105	0.4	130.3
66	993	0.474	125
63	1045	0.42	132.6

Table A6(b) - Distance from Cell: 21in. (Calculated Values)

Insolation on Cell (W/m^2)	Power Output (W)	Efficiency (%)
52,294	0.37	7.1
53,663	1.17	21.7
56,894	0.83	14.6
33,403	0.06	1.7
37,783	0.17	4.4
21,027	0.01	0.6
57,168	0.56	9.8
57,442	2.84	49.4
57,168	2.59	45.3
52,020	1.69	32.5
56,073	0.34	6.1
58,646	0.59	10.1
57,496	0.27	4.7
59,468	0.52	8.7
58,537	0.27	4.6
56,730	0.59	10.4
57,223	0.71	12.5
57,277	0.50	8.8
52,020	0.19	3.6
54,758	0.51	9.3
54,485	0.56	10.2
57,715	0.22	3.7
59,851	0.57	9.6
59,851	0.73	12.3
59,960	1.17	19.5
69,379	0.54	7.8
58,099	0.72	12.5
51,747	0.37	7.2
60,508	0.32	5.3
54,375	0.45	8.3
57,223	0.35	6.2

Table A5(c) - Distance from Cell: 21in. (Modeled Values)

Ambient Temperature (°F)	Insolation on Cell (W/m^2)	Measured Cell Temperature (°F)	Predicted Cell Temperature (°F)	Error (%)
34	53663	208	56.55	-72.8
36	56894	177	60.16	-66.0
54	33403	102	71.54	-29.9
59	37783	137	78.51	-42.7
54	21027	143	66.00	-53.8
43	57168	133	68.46	-48.5
50	57442	58	76.22	32.3
52	57168	92	78.17	-15.4
43	52020	68	66.67	-2.0
53	56073	94	79.44	-15.5
48	58646	94	74.81	-20.0
52	57496	110	78.79	-28.4
49	59468	96	76.23	-20.6
39	58537	103	64.70	-37.0
66	56730	120	93.64	-22.0
42	57223	95	67.55	-28.9
54	57277	90	80.98	-10.0
59	52020	101	84.43	-16.4
69	54758	113	96.17	-14.9
74	54485	120	101.39	-15.5
61	57715	102	88.81	-12.9
46	59851	99	72.99	-26.3
47	59851	105	74.03	-29.5
59	59960	131	87.04	-33.3
62	69379	112	94.18	-15.9
60	58099	132	87.53	-33.7
80	51747	130	106.67	-17.9
66	60508	130	95.12	-27.0
66	54375	125	92.72	-25.8

Table A6(a) - Distance from the Cell: 21.5in. (Measured Values)

Ambient Temperature (°F)	Insolation (W/m^2)	Voltage (V)	Cell Temperature (°F)
54	609	0.335	122
59	860	0.6	150
54	274	0.184	172
43	1057	1.173	126
50	1046	2.6	60
52	1046	2.61	104.2
43	960	2.1	73
53	1098	0.751	88
48	1093	0.88	86.6
52	1040	0.546	112
49	1087	0.703	93
39	1072	0.478	107
40	1068	0.74	94
66	1042	0.8	121
42	1050	0.91	94
54	872	0.666	89
59	1016	0.6	103.3
69	1008	0.762	121
74	1016	0.841	116
61	1108	0.416	110
47	1092	0.892	105
47	1092	0.913	105
59	1096	1.045	133
62	1185	0.91	125
60	1073	0.955	133
80	1125	0.76	139
66	1122	0.562	133.3
66	1005	0.764	130
63	1047	0.582	130.8

Table A7(b) - Distance from Cell: 21.5in. (Calculated Values)

Insolation on Cell (W/m^2)	Power Output (W)	Efficiency (%)
48,021	0.11	2.3
67,813	0.36	5.3
21,605	0.03	1.6
83,347	1.38	16.5
82,479	6.76	82.0
82,479	6.81	82.6
75,698	4.41	58.3
86,580	0.56	6.5
86,185	0.77	9.0
82,006	0.60	7.3
85,712	0.99	11.5
84,529	0.46	5.4
84,214	1.10	13.0
82,164	1.28	15.6
82,795	1.66	20.0
68,759	0.89	12.9
80,114	0.72	9.0
79,483	1.16	14.6
80,114	1.41	17.7
87,368	0.35	4.0
86,106	1.59	18.5
86,106	1.67	19.4
86,422	2.18	25.3
93,440	1.66	17.7
84,608	1.82	21.6
88,709	1.16	13.0
88,472	0.63	7.1
79,246	1.17	14.7
82,558	0.68	8.2

Table A6(c) - Distance from Cell: 21.5in. (Modeled Values)

Ambient Temperature (°F)	Insolation on Cell (W/m^2)	Measured Cell Temperature (°F)	Predicted Cell Temperature (°F)	Error (%)
54	48021	122	76.49	-37.3
59	67813	150	88.90	-40.7
54	21605	172	65.74	-61.8
43	83347	126	75.99	-39.7
50	82479	60	82.42	37.4
52	82479	104	84.32	-19.1
43	75698	73	72.88	-0.2
53	86580	88	89.07	1.2
48	86185	87	83.17	-4.0
52	82006	112	86.19	-23.0
49	85712	93	84.04	-9.6
39	84529	107	72.16	-32.6
40	84214	94	73.13	-22.2
66	82164	121	101.60	-16.0
42	82795	94	74.82	-20.4
54	68759	89	83.95	-5.7
59	80114	103	93.44	-9.5
69	79483	121	104.00	-14.0
74	80114	116	109.68	-5.5
61	87368	110	98.25	-10.7
47	86106	105	81.58	-22.3
47	86106	105	81.56	-22.3
59	86422	133	94.86	-28.7
62	93440	125	100.86	-19.3
60	84608	133	95.48	-28.2
80	88709	139	119.25	-14.2
66	88472	133	103.92	-22.0
66	79246	130	100.53	-22.7

Table A7(a) - Distance from the Cell: 22in. (Measured Values)

Ambient Temperature (°F)	Insolation (W/m^2)	Voltage (V)	Cell Temperature (°F)
65	1053	2.25	120
33	986	2.24	174
36	1028	2.06	209
54	615	0.44	123
59	726	1.2	170
54	312	1.13	130
43	1043	1.78	130
50	1043	2.65	60
52	1032	2.64	109.8
43	880	2.21	87
53	1020	1.13	82
48	1047	1.87	99.7
52	1045	0.844	115
49	887	0.73	95
39	1076	0.704	103
66	1043	1.26	118
42	1042	1.361	102
54	958	1.11	97
70	1004	1.23	118
74	1012	1.41	115
61	1112	0.611	107
47	1093	1.732	107
47	1090	1.22	107
59	1099	1.51	134.8
60	1137	1.455	130.8
78	1069	1.2	143
66	1160	0.8	136
66	1004	1.11	137
63	1038	0.878	140.7

Table A8(b) - Distance from Cell: 22in. (Calculated Values)

Insolation on Cell (W/m^2)	Power Output (W)	Efficiency (%)
129,736	5.06	39.0
121,482	5.02	41.3
126,656	4.24	33.5
75,772	0.19	2.6
89,448	1.44	16.1
38,440	1.28	33.2
128,504	3.17	24.7
128,504	7.02	54.6
127,149	6.97	54.8
108,422	4.88	45.0
125,671	1.28	10.2
128,997	3.50	27.1
128,751	1.42	11.1
109,284	1.07	9.8
132,570	0.99	7.5
128,504	3.18	24.7
128,381	3.70	28.9
118,032	2.46	20.9
123,699	3.03	24.5
124,685	3.98	31.9
137,006	0.75	5.4
134,665	6.00	44.6
134,295	2.98	22.2
135,404	4.56	33.7
140,086	4.23	30.2
131,708	2.88	21.9
142,919	1.28	9.0
123,699	2.46	19.9
127,888	1.54	12.1

Table A7(c) - Distance from Cell: 22in. (Modeled Values)

Ambient Temperature (°F)	Insolation on Cell (W/m^2)	Measured Cell Temperature (°F)	Predicted Cell Temperature (°F)	Error (%)
33	121482	174	71.44	-58.9
36	126656	209	76.54	-63.4
54	75772	123	84.93	-31.0
59	89448	170	93.95	-44.7
54	38440	130	71.25	-45.2
43	128504	130	86.77	-33.3
50	128504	60	94.08	56.8
52	127149	110	95.53	-13.0
43	108422	87	80.58	-7.4
53	125671	82	99.19	21.0
48	128997	100	93.06	-6.7
52	128751	115	98.50	-14.4
49	109284	95	89.56	-5.7
39	132570	103	84.27	-18.2
66	128504	118	113.82	-3.5
42	128381	102	85.58	-16.1
54	118032	97	97.35	0.4
70	123699	118	116.95	-0.9
74	124685	115	121.35	5.5
61	137006	107	111.91	4.6
47	134665	107	92.31	-13.7
47	134295	107	93.56	-12.6
59	135404	135	107.00	-20.6
60	140086	131	109.76	-16.1
78	131708	143	128.31	-10.3
66	142919	136	118.89	-12.6
66	123699	137	112.46	-17.9

Table A8(a) - Distance from the Cell: 22.5in (Measured Values)

Ambient Temperature (°F)	Insolation (W/m^2)	Voltage (V)	Cell Temperature (°F)
51	1030	2.35	96
68	925	2.35	130
54	633	0.81	132
59	934	1.8	185
54	298	0.22	227
50	1042	2.65	60
54	1043	2.66	111.4
43	957	2.23	89
53	1025	2.26	103
48	1043	2.2	101.1
52	1050	1.282	114
49	1087	1.16	100
39	1068	1.18	105.6
39	1064	1.39	107.7
66	1033	1.77	121
42	1050	1.843	103
54	996	1.41	98
70	1000	1.57	121
75	1017	1.71	119
47	1098	1.88	108
47	1095	1.9	109
59	1094	2.1	135.6
78	1064	1.56	143
66	1200	1.438	136.8
66	1001	1.62	141
63	1047	1.37	138

Table A9(b) - Distance from Cell: 22.5in. (Calculated Values)

Insolation on Cell (W/m^2)	Power Output (W)	Efficiency (%)
225,605	5.52	24.5
202,606	5.52	27.3
138,648	0.66	4.7
204,577	3.24	15.8
65,272	0.05	0.7
228,233	7.02	30.8
228,452	7.08	31.0
209,615	4.97	23.7
224,509	5.11	22.8
228,452	4.84	21.2
229,985	3.29	14.3
238,090	2.69	11.3
233,928	2.78	11.9
233,052	3.86	16.6
226,262	6.27	27.7
229,985	6.79	29.5
218,157	3.98	18.2
219,034	4.93	22.5
222,757	5.85	26.3
240,499	7.07	29.4
239,842	7.22	30.1
239,623	8.82	36.8
233,052	4.87	20.9
262,840	4.14	15.7
219,253	5.25	23.9
229,328	3.75	16.4

Table A8(c) - Distance from Cell: 22.5in. (Modeled Values)

Ambient Temperature (°F)	Insolation on Cell (W/m^2)	Measured Cell Temperature (°F)	Predicted Cell Temperature (°F)	Error (%)
54	138648	132	100.90	-23.6
59	204577	185	121.77	-34.2
54	65272	227	79.35	-65.0
50	228233	60	115.89	93.1
54	228452	111	120.12	7.8
43	209615	89	103.32	16.1
53	224509	103	119.38	15.9
48	228452	101	114.26	13.0
52	229985	114	120.57	5.8
49	238090	100	119.38	19.4
39	233928	106	105.12	-0.5
39	233052	108	104.18	-3.3
66	226262	121	134.68	11.3
42	229985	103	105.56	2.5
54	218157	98	119.89	22.3
70	219034	121	138.55	14.5
75	222757	119	144.86	21.7
47	240499	108	114.32	5.9
47	239842	109	114.04	4.6
59	239623	136	127.54	-5.9
78	233052	143	151.51	6.0
66	262840	137	145.34	6.2
66	219253	141	133.26	-5.5

Table A9(a) - Distance from the Cell: 23in. (Measured Values)

Ambient Temperature (°F)	Insolation (W/m^2)	Voltage (V)	Cell Temperature (°F)
65	1051	2.31	150
33	963	2.28	139
36	1029	2.15	248
54	691	1.09	136
59	1012	2.1	230
54	1033	1.98	133.8
50	1045	2.65	60.5
54	1067	2.64	113.1
43	820	2.16	84
53	1018	2.48	98
48	1031	2.63	98.9
52	1032	1.675	110
49	1040	1.79	104
39	1073	1.62	104.5
39	1060	1.97	104.6
66	1036	2.21	119
42	1048	2.19	97
56	904	1.47	94
70	1005	2.1	120
74	1064	2.21	120
47	1088	2.23	108
47	1095	2.3	108
59	1119	2.37	136.9
78	1072	2.25	142
66	1089	1.8	128.5
66	1008	1.93	143

Table A10(b) - Distance from Cell: 23in. (Calculated Values)

Insolation on Cell (W/m^2)	Power Output (W)	Efficiency (%)
517,960	5.34	10.3
474,591	5.20	11.0
507,118	4.62	9.1
340,542	1.19	3.5
498,740	4.41	8.8
509,089	3.92	7.7
515,003	7.02	13.6
525,845	6.97	13.3
404,117	4.67	11.5
501,696	6.15	12.3
508,103	6.92	13.6
508,596	5.61	11.0
512,539	6.41	12.5
528,802	5.25	9.9
522,395	7.76	14.9
510,567	9.77	19.1
516,481	9.59	18.6
445,514	4.32	9.7
495,290	8.82	17.8
524,366	9.77	18.6
536,194	9.95	18.5
539,644	10.58	19.6
551,472	11.23	20.4
528,309	10.13	19.2
536,687	6.48	12.1
496,768	7.45	15.0

Table A9(c) - Distance from Cell: 23in. (Modeled Values)

Ambient Temperature (°F)	Insolation on Cell (W/m^2)	Measured Cell Temperature (°F)	Predicted Cell Temperature (°F)	Error (%)
33	474591	139	133.02	-4.3
36	507118	248	141.77	-42.8
54	340542	136	142.04	4.4
59	498740	230	174.81	-24.0
54	509089	134	172.91	29.2
50	515003	61	166.51	175.2
54	525845	113	173.07	53.0
43	404117	84	136.65	62.7
53	501696	98	168.27	71.7
48	508103	99	161.31	63.1
52	508596	110	168.53	53.2
49	512539	104	164.12	57.8
39	528802	105	153.31	46.7
39	522395	105	149.24	42.7
66	510567	119	183.03	53.8
42	516481	97	150.81	55.5
56	445514	94	163.54	74.0
70	495290	120	186.41	55.3
74	524366	120	196.64	63.9
47	536194	108	161.39	49.4
47	539644	108	161.30	49.3
59	551472	137	179.35	31.0
78	528309	142	201.66	42.0
66	536687	129	192.33	49.7
66	496768	143	182.49	27.6

Table A11(a) - Limits for Maryland (1000 W/m^2) at 356°F

Ambient Temperature (°F)	Insolation on Cell (suns)	Size of Mirror (ft^2)
50	1559	1.962
55	1524	1.917
60	1489	1.873
65	1454	1.829
70	1419	1.785
75	1385	1.742
80	1351	1.700
85	1318	1.658
90	1284	1.616
85	1318	1.658
100	1219	1.533

Table A10(b) - Limits for Maryland (1000 W/m^2) at 300°F

Ambient Temperature (°F)	Insolation on Cell (suns)	Size of Mirror (ft^2)
50	1196	1.505
55	1163	1.464
60	1131	1.423
65	1099	1.383
70	1067	1.343
75	1036	1.303
80	1005	1.264
85	974	1.226
90	944	1.187
85	914	1.149
100	884	1.112

Table A10(c) - Limits for Maryland (1000 W/m^2) at 212°F

Ambient Temperature (°F)	Insolation on Cell (suns)	Size of Mirror (ft^2)
50	680	0.855
55	652	0.820
60	625	0.786
65	598	0.752
70	571	0.718
75	545	0.685
80	519	0.653
85	493	0.621
90	468	0.589
85	443	0.558
100	419	0.527

Table A12(a) - Limits for New England (850 W/m^2) at 356°F

Ambient Temperature (°F)	Insolation on Cell (suns)	Size of Mirror (ft^2)
50	1559	2.308
55	1524	2.255
60	1489	2.203
65	1454	2.152
70	1419	2.100
75	1385	2.050
80	1351	2.000
85	1318	1.950
90	1284	1.901
85	1251	1.852
100	1219	1.804

Table A11(b) - Limits for New England (850 W/m^2) at 300°F

Ambient Temperature (°F)	Insolation on Cell (suns)	Size of Mirror (ft^2)
50	1196	1.770
55	1163	1.722
60	1131	1.674
65	1099	1.627
70	1067	1.580
75	1036	1.533
80	1005	1.487
85	974	1.442
90	944	1.397
85	914	1.352
100	884	1.308

Table A11(c) - Limits for New England (850 W/m^2) at 212°F

Ambient Temperature (°F)	Insolation on Cell (suns)	Size of Mirror (ft^2)
50	680	1.006
55	652	0.965
60	625	0.925
65	598	0.885
70	571	0.845
75	545	0.806
80	519	0.768
85	493	0.730
90	468	0.693
85	443	0.656
100	419	0.620

Table A13(a) - Limits for Southwest (1450 W/m^2) at 356°F

Ambient Temperature (°F)	Insolation on Cell (suns)	Size of Mirror (ft^2)
70	1419	1.231
75	1385	1.202
80	1351	1.172
85	1318	1.143
90	1284	1.114
95	1251	1.086
100	1219	1.057
105	1186	1.029
110	1154	1.002
115	1123	0.974
120	1091	0.947

Table A12(b) - Limits for Southwest (1450 W/m^2) at 300°F

Ambient Temperature (°F)	Insolation on Cell (suns)	Size of Mirror (ft^2)
70	1067	0.926
75	1036	0.899
80	1005	0.872
85	974	0.845
90	944	0.819
95	914	0.793
100	884	0.767
105	855	0.741
110	825	0.716
115	797	0.691
120	768	0.666

Table A12(c) - Limits for Southwest (1450 W/m^2) at 212°F

Ambient Temperature (°F)	Insolation on Cell (suns)	Size of Mirror (ft^2)
70	571	0.496
75	545	0.473
80	519	0.450
85	493	0.428
90	468	0.406
95	443	0.385
100	419	0.363
105	395	0.342
110	371	0.322
115	348	0.302
120	325	0.282

Appendix B - Data Collection Procedure

Procedure for Data Collection

Data was collected using our device several times per day over several months. To ensure the validity of the data collection, a multi-step procedure was implemented. One data collection session took roughly 45 minutes. The individual steps are detailed here:

1. The apparatus is brought outside from the storage area
2. The apparatus is placed on the ground, with the mirror oriented towards the sun
3. The data spreadsheet is brought up on a computer, or a table is written down to record the values to be input later
4. Voltmeter probes are placed on photovoltaic cell leads in order to record output voltage
5. The back face of the lens is adjusted to be 19 inches from the face of the cell. Adjustment is done by hand, with the distance measured using a tape measure
6. Wait 4 to 6 minutes to allow for the cell to reach a stable temperature.
7. When it is time to take measurements, the following steps are taken:
    a. Distance from cell recorded
    b. Time recorded
    c. Ambient temperature and wind speed recorded using data from weather.com
    d. Cell temperature recorded using an infrared thermometer
        i. The gun emits a visible laser beam, which is moved across the cell and its immediate surrounding area in order to find the highest temperature in this region. The highest temperature is chosen

because it gives an indication of the maximum effect light concentration can have on temperature

e Incident solar radiation recorded using a pyranometer. The pyranometer is pointed in the same direction as the mirror and then tilted upward. The highest value is recorded for consistency with other collected data

f Output voltage recorded using voltmeter

8 The inputted data is used to calculate the concentration, total radiation on the cell, power output, and efficiency

a Concentration is calculated by using the following equation: $(\frac{24}{24-\text{distance from cell}})^2$. Knowing that the focal length of the lens is 24 inches, this equation can be derived through the use of similar triangles

b Total radiation on the cell is determined by multiplying the measured insolation by the concentration

c The power output is determined by using the equation: $P = V^2R$ where V is the voltage and R is the resistance

d The efficiency is determined by converting the total radiation on the cell from W/m^2 to W/cm^2 by dividing by 10,000. This value is then divided into the measured power output and multiplied by 100 to determine the efficiency

9 The lens is moved back by half an inch (.5in)

10 The apparatus is reoriented as necessary for best alignment with sun

11 Steps 6-10 are repeated until the lens is 23 inches from the cell

12 The materials are packed up carefully so as to prevent any damaged

13 The apparatus is returned to storage

Appendix C - Solar Cell Data Sheet

CTJ Photovoltaic Cell

Triple-Junction Solar Cell for Terrestrial Applications

emcore
empower with light™

TERRESTRIAL PHOTOVOLTAICS

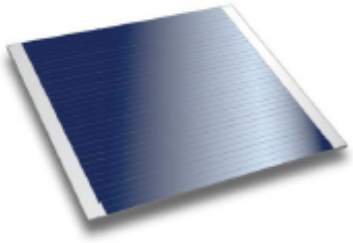

Standard CTJ Cell Dimensions

External Dimensions	10.68 x 10.075 mm
Designed Aperture Area	10 x 10 mm
Total Nominal Active Area	100 mm²
Bondable Perimeter Busbar	0.235 mm
Total Cell Thickness	~0.2 mm

39% Efficiency under Concentrated Illumination

Features & Characteristics

- Triple-Junction High-Efficiency Solar Cells on Germanium Substrate for Terrestrial Concentrated Photovoltaic Applications
- Multi-Layer Antireflective Coating Providing Low Reflectance over Wavelength Range 0.3 to 1.8µm
- Characterized for Terrestrial Applications Under Concentrated Illumination (Over 1500 Suns)
- Weldable or Solderable Contacts, Front and Back
- Standard 1x1 cm2 (Designated Aperture Area)
- Customer Specific Sizes Available
- Available in Cell and Application-Specific Configurations
- Application-Specific Grid Design Service to Optimize Power Output
- 4" Ge Manufacturing Operation with >300MW Annual Capacity

Performance Data

Solar cell electrical output parameters
@ AM1.5D, Low-AOD Illumination, 25°C

	1X Concentration	503X Concentration	1182X Concentration
Efficiency	31.4%	39.0%	36.3%
V_{oc}	2.605 V	3.193 V	3.251 V
J_{sc}	13.85 mA / cm²	6.96 A/cm²	16.37 A/cm²
V_{mp}	2.33 V	2.84 V	2.68 V
J_{mp}	13.4 mA / cm²	6.8 A/cm²	16.04 A/cm²
P_{mp}	31.4 mW / cm²	19.3 W/cm²	42.9 W/cm²

P 505 332 5000 F 505 332 5100 E photovoltaic-sales@emcore.com W www.emcore.com

CTJ Photovoltaic Cell

Triple-Junction Solar Cell for Terrestrial Applications

emcore
empower with light™

TERRESTRIAL PHOTOVOLTAICS

Quantum Efficiency

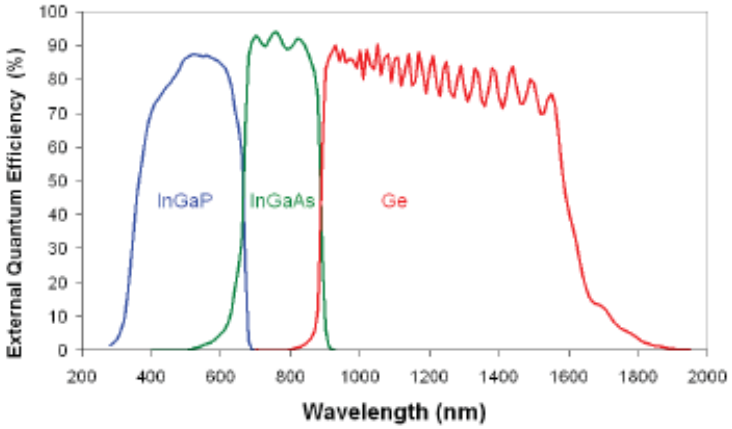

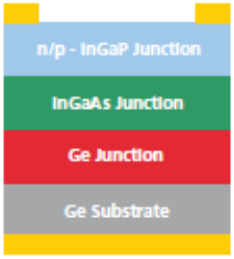

Cell Structure Diagram
(Tunnel diodes not shown)

Temperature Dependence at 800 Suns (20°C - 70°C)

ΔVoc = - 4 mV/°C
ΔJsc = 7.2 mA/°C
Δefficiency = -0.06% (absolute)/°C

Efficiency vs. Concentration

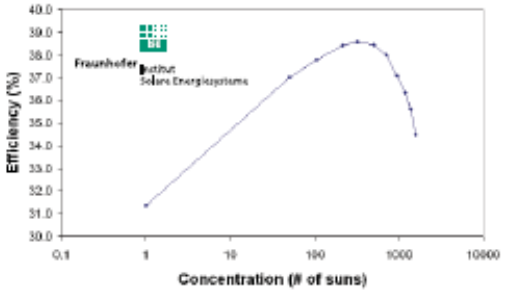

Typical IV Curves at Varying Concentration Levels, 25° C

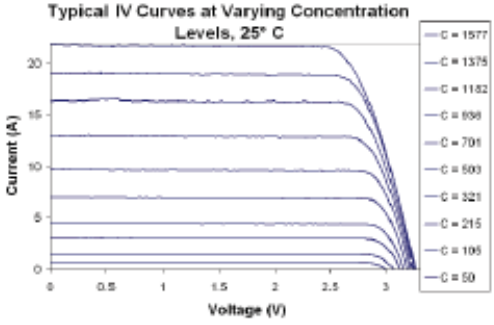

P 505 332 5000 F 505 332 5100 E photovoltaic-sales@emcore.com W www.emcore.com

Appendix D - Mirror Film Data Sheet

ReflecTech Mirror Film

Simply Brilliant

Technical Data

ReflecTech® Mirror Film

Performance Characteristics

Specular Reflectance[1]	94%	At 25 mrad, 660 nm
Solar-Weighted Hemispherical Reflectance[2]	93%	DIN 5036-1, 3
		ASTM E891

(1) At 1.4° acceptance angle measured on Devices & Services 15R Specular Reflectometer
(2) Integrated over direct normal air mass 1.5 solar spectrum.

Product/Physical Characteristics

	Machine Direction	Transverse Direction	
Tensile Strength (MPa)	61	64	ASTM D882
Elongation at Break (%)	88	72	ASTM D882
Yield Strength at 2% Offset (MPa)	40	36	ASTM D882
Yield Elongation at 2% Offset (%)	4.7	4.6	ASTM D882
Modulus (MPa)	1430	1566	ASTM D882

Nominal Thickness	0.004 in	*(4 mils, 0.1 mm)*	
Coefficient of Thermal Expansion (cm/cm/°C)	5.5 x 10-5		ASTM E831

Application Characteristics

Adhesion to Aluminum[3]	Initial 11.4	ASTM D903
180° Peel Strength (N/25mm)	Fully Cured 19.9	ASTM D903

(3) Adhesion depends on the nature of the surface. The indicated values are for reference only.

Storage and Operation

Shelf Life[4]	1 year	
Maximum Operating Temperature	60°C	*(140°F)*
Cleaning	Brushless pressure wash with de-mineralized or de-ionized water only	

(4) Store in clean and dry environment that is not in direct sunlight in a location with an ambient temperature of 100°F (38°C) or less.

www.ReflecTechSolar.com

Appendix E - Lens Data Sheet

11.0" X 11.0", 24" Focal Length, Fresnel Lens

Stock No. #32-691 **In Stock:**

$105.00

Quantity 1 ADD TO CART REQUEST QUOTE

See All Products | Live Chat | Add to Wish List

Specifications

Groove Density (grooves/inch)	200
Dimensions (inches)	11.0 x 11.0
Effective Size (inches)	10.5 x 10.5
Effective Focal Length EFL (inches)	24.00
Center Thickness CT (inches)	0.09
Focal Length Tolerance (%)	±5
Dimensional Tolerance (inches)	±0.05
Thickness Tolerance (%)	±40
Transmission (%)	92 (from 400-1100nm)
Index of Refraction n_d	1.49
Operating Temperature (°C)	80 (Maximum)
RoHS	Compliant

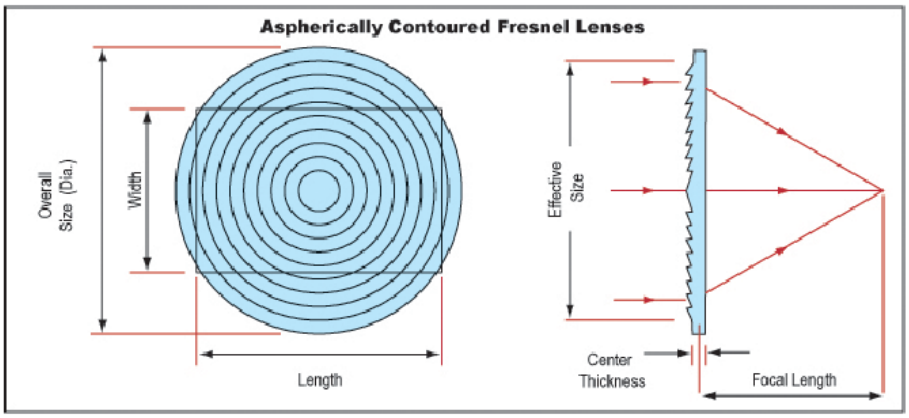
Aspherically Contoured Fresnel Lenses
Overall Size (Dia.)
Width
Length
Effective Size
Center Thickness
Focal Length

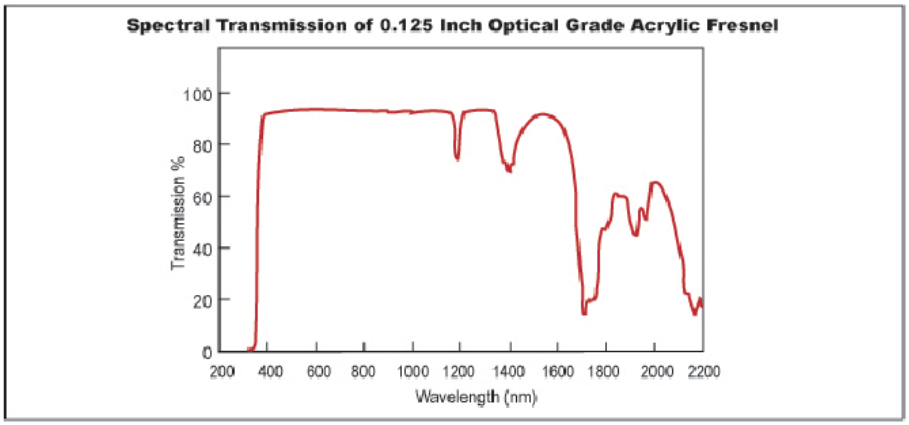
Spectral Transmission of 0.125 Inch Optical Grade Acrylic Fresnel
Transmission %
100
80
60
40
20
0
200
400
600
800
1000
1200
1400
1600
1800
2000
2200
Wavelength (nm)

Appendix F - Pyranometer Data Sheet

Pyranometer Meter

MP-100 & 200 Series

Pyranometer Meter

This sensor is calibrated to measure total shortwave radiation. The evaporation of water from soil and transpiration of water from plant leaves are partly determined by the intensity of shortwave radiation, which is measured in Joules per meters squared per second or Watts per meters squared.

2

Cleaning

Debris on the meter is a common cause of low readings. Salt deposits can accumulate on a sensor from evaporation of sprinkler irrigation water and dust, which can accumulate during periods of low rainfall. Salt deposits should be dissolved and removed with vinegar and a soft cloth or q-tip. Dust and other organic deposits are best removed with water, rubbing alcohol or window cleaner. *Never use an abrasive cleaner on the lens.*

3

Mounting the Sensor

Nylon Screw:
10-32x3/8

Mount the sensor to a solid surface with the nylon mounting screw.

The sensor should be mounted level for the most accurate measurements. We recommend using our leveling plate (AL-100). The sensor should be mounted with the cable pointing toward true north in the northern hemisphere or true south in the southern hemisphere to minimize azimuth error. The azimuth error is typically less than 1%.

Model AL-100

Orientation

4

Spectral Response and Calibration

An ideal pyranometer measures the entire solar spectrum, 280 to 2800 nm. However, about 90% of sunlight energy is between 300 and 11000 nm. Models MP-100 and MP-200 are calibrated to estimate all of the shortwave energy from sunlight. Apogee pyranometers are calibrated under sunlight over a multiple day period to a heated and ventilated Kipp & Zonen model CM21 precision reference radiometer.

Spectral Response of the Apogee Pyranometer

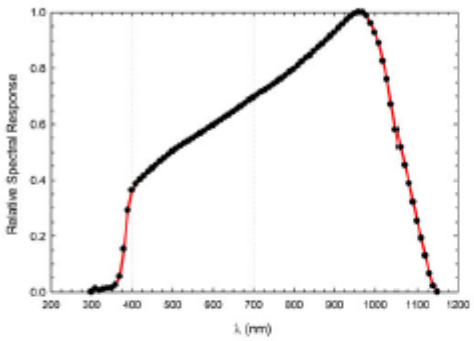

Using the Meter

1) Press the power button to start. The meter will turn itself off 2 minutes after button is pushed to conserve battery.

2) Choose Mode: To choose between SMPL and LOG modes push mode twice and use up/down to make choice. Once desired mode is blinking press mode two more times to begin.

For Automatic Measurements: Use LOG mode. Meter will power on/off to record a measurement every thirty seconds.

For Manual Measurements: Use SMPL mode. Press sample when you want to take a measurement. Store up to 99 manual measurements.

3) To Reset Meter: From LOG or SMPL mode, press mode twice (RUN should be blinking), then while pressing down, press mode once.

CAUTION—Resetting will erase ALL measurements.

4) Review data: press up/down. To exit and return to present conditions and the capability to take measurements, press sample.

5) In LOG mode, every 30 minutes the meter will average sixty 30-second measurements taken and store the average. Ninety-nine 30-minute averaged measurements can be stored. Every forty-eight measurements (making a 24-hour period) the meter will also store a daily total. In addition, 99 daily averages can be stored and are available for download only. These measurements are not viewable on the meter LCD. All measurements taken in LOG mode will continue to be stored, eliminating the oldest measurement. To keep data, switch out of log mode.

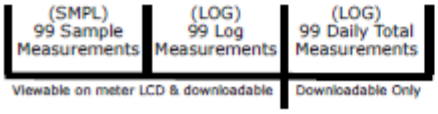

Clear Sky CALCULATOR

The Clear Sky Calculator is designed to determine the need for radiation sensor recalibration. It determines the intensity of radiation falling on a horizontal surface at any time of the day in any location in the world. It is most accurate when used near solar noon in the summer months.

The calculator is found at www.clearskycalculator.com and is used by typing conditions into the Clear Sky model and comparing measured values with the calculated value for a clear sky. If the output of the sensor over multiple days at solar noon is consistently less than the model value (by more than 8%), the sensor should be cleaned and re-leveled. If the output is still low after a second test, email calibration@apogeeinstruments.com to discuss test results and the possible return of sensors. When used near solar noon over multiple clear, unpolluted days during the spring and summer months, it is estimated that the accuracy of the model can be ± 4% in all climates and locations around the world.

Example of Model Output

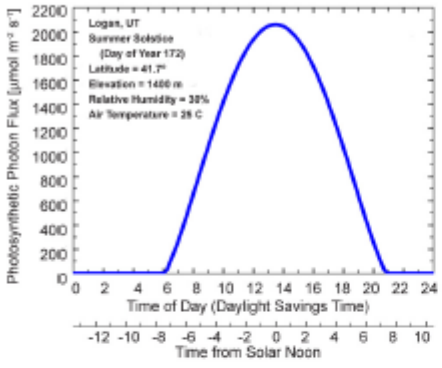

Characteristics

Cosine Response

Some of the radiation coming into a sensor at low angles is reflected, which causes low readings. The convex optical disc found on meters and sensors is designed to capture radiation at low angles and minimize cosine response errors. The cosine error for typical applications is less than 2%.

Temperature Response

The temperature response is less than 0.1% per degree C. This temperature error is not significant in most applications.

Long-Term Stability

Our research indicates that the average output increases approximately 1% per year because of changes in the optical transparency of the diffusion disk. We recommend returning the meter for recalibration every 2 years.

Error Codes

The most common error code is Error 4. The meter will display this error code on the screen if the battery voltage is too low.

To replace the battery, unscrew the back area on the meter. Then use a pair of tweezers to gently remove the battery and replace it with a new one. Screw the back cover back on the meter, but be careful not to over-tighten as it can affect the LCD screen.

Specifications

Memory
- 99 manually stored data points
- Automatically store 99 consecutive 30 minute averages
- 99 daily averages

Cosine Response
- 45º zenith angle: ± 1%
- 75º zenith angle: ± 4%

Absolute Accuracy
- ± 5%

Repeatability
- ± 1%

Uniformity
- ± 3%

Sensitivity
- Custom calibrated to exactly 5.0 W m^{-2} per mV

Operating Environment
- 0 to 50 C
- Less than 90% non-condensing, relative humidity up to 30 C
- Less than 70% relative humidity from 30 to 50 C
- Sensor is waterproof, meter is splash resistant

Input Power
- CR2320 3 V coin cell battery

Range
- 0 - 1999 W m^{-2}

Display
- 4.2 by 2.8 cm

Materials
- Anodized aluminum with cast acrylic lens

Cable (MP-200 Series)
- 2 meters of twisted-pair wire
- Foil shield
- Santoprene jacket
- Longer cable lengths are available in multiples of 5 meters

Dimensions
- 2.4 cm diameter by 2.75 cm height

Mass
- MP-100: 150 g
- MP-200: 180 g

Warranty
- 1 year against defects in materials and workmanship

apogee

www.apogeeinstruments.com
techsupport@apogeeinstruments.com
435.792.4700
Fax: 435.787.8268

Appendix G - Infrared Thermometer Data Sheet

FLUKE.

Fluke 566 and 568 Thermometers

Technical Data

Two-in-one infrared and contact thermometers with an innovative dot matrix display.

Just when you thought advanced IR temperature measurement should be easier! With a straight-forward user interface and soft-key menus, the Fluke 566 and 568 make even complex measurements easy. Quickly navigate and adjust emissivity, start data logging, or turn on and off alarms, with just a few pushes of a button.

With a rugged, easy-to-use, ergonomic design, the Fluke 566 and 568 can stand up to tough industrial, electrical, and mechanical environments.

- Measure -40 °C to 800 °C /-40 °F to 1472 °F (568) or -40 °C to 650 °C/-40 °F to 1202 °F (566)
- Easily access advanced features with the soft-key buttons and graphical display
- Measure smaller objects from further away, with a distance-to-spot ratio of 50:1 (568) or 30:1 (566)
- Compatibility with all standard miniconnector K-type thermocouples allows you to preserve your thermocouple investments
- Confidently measure a wide variety of surfaces with the adjustable emissivity feature, including a built-in material table
- Capture up to 99 points (568) or 20 point (566) of data, for downloading and recalling later
- Easily trend and analyze data with included FlukeView® Forms software (568)
- See your data right away without leaving the site, using the USB (568) and your laptop for "Hands-free" datalogging
- Confidently troubleshoot equipment with 1 % measurement accuracy
- Versatile interface with six languages from which to choose
- Two-year warranty

FLUKE®

Product specifications

	566	568
Infrared temperature range	-40 °C to 650 °C (-40 °F to 1202 °F)	-40 °C to 800 °C (-40 °F to 1472 °F)
Infrared accuracy	< 0 °C (32 °F): ± (1.0 °C (± 2.0 °F) + 0.1 °/1 °C or °F); > 0 °C (32 °F): ± 1 % or ± 1.0 °C (± 2.0 °F), whichever is greater	
Display resolution	0.1 °C / 0.1 °F	
Infrared spectral response	8 µm to 14 µm	
Infrared response time	< 500 msec	
Thermocouple Type-K input temperature range	-270 °C to 1372 °C (-454 °F to 2501 °F)	
Thermocouple Type-K input accuracy	-270 °C to -40 °C: ± (1 °C + 0.2 °/1 °C) (-454 °F to -40 °F: ± (2 °F + 0.2 °/1 °F)) -40 °C to 1372 °C: ± 1 % or 1 °C (-40 °F to 2501 °F: ± 1 % or 2 °F), whichever is greater	
D:S (distance to measurement spot size)	30:1	50:1
Laser sighting	Single-point laser < 1 mw output Class 2 (II) operation, 630 nm to 670 nm	
Minimum spot size	19 mm (0.75 in)	
Emissivity adjustment	By built-in table of common materials or digitally adjustable from 0.10 to 1.00 by 0.01	
Data storage with Date/Time stamp	20 points	99 points
PC Interface and cable	None	USB 2.0 with FlukeView® Forms software
Hi/Low alarms	Audible and two-color visual	
Min/Max/Avg/Dif	Yes	
Display	Dot matrix 98 x 96 pixels with function menus	
Backlight	Two levels, normal and extra bright for darker environments	
Trigger lock	Yes	
Switchable Celsius and Fahrenheit	Yes	
Power	2 AA/LR6 Batteries	2 AA/LR6 Batteries and USB when used with a PC
Battery life	If used continuously: laser and backlight on,12 hours; laser and backlight off, 100 hours	
Operating temperature	0 °C to 50 °C (32 °F to 122 °F)	
Storage temperature	-20 °C to 60 °C (-40 °F to 140 °F)	
Bead thermocouple Type-K range	-40 °C to 260 °C (-40 °F to 500 °F)	
Bead thermocouple Type-K accuracy	± 1.1 °C (2.0 °F) from 0 °C to 260 °C (32 °F to 500 °F), typically within 1.1 °C (2.0 °F) from -40 °C to 0 °C (-40 °F to 32 °F)	

Ordering Information

Fluke-566 Infrared thermometer
Fluke-568 Infrared thermometer

Includes: Infrared thermometer with contact thermometer capabilities, FlukeView® Forms software (568 only), USB cable (568 only), K-type thermocouple bead probe, hard carrying case, quick start guide, and users manual.

Fluke. *Keeping your world up and running.®*

Fluke Corporation
PO Box 9090, Everett, WA 98206 U.S.A.

Fluke Europe B.V.
PO Box 1186, 5602 BD
Eindhoven, The Netherlands

For more information call:
In the U.S.A. (800) 443-5853 or
Fax (425) 446-5116
In Europe/M-East/Africa +31 (0) 40 2675 200 or
Fax +31 (0) 40 2675 222
In Canada (800)-36-FLUKE or
Fax (905) 890-6866
From other countries +1 (425) 446-5500 or
Fax +1 (425) 446-5116
Web access: http://www.fluke.com

Printed in U.S.A. 6/2007 3065001 D-EN-N Rev A

References

[1] U. S. E. I. Administration. (2011, 4/26/2012). *Annual Energy Review 2010*. Available: http://205.254.135.24/totalenergy/data/annual/pdf/aer.pdf

[2] S. Kurtz, "Opportunities and Challenges for Development of a Mature Concentrating Photovoltaic Power Industry," National Renewable Energy Laboratory2009.

[3] N. Lewis and D. Nocera, "Powering the planet: Chemical challenges in solar energy utilization," *Proceedings of the National Academy of Sciences of the United States of America*, vol. 103, pp. 15729-15735, OCT 24 2006 2006.

[4] M. Green, "Photovoltaic principles," *Physica E-Low-Dimensional Systems & Nanostructures*, vol. 14, pp. 11-17, APR 2002 2002.

[5] "Vast Power of the Sun Is Tapped By Battery Using Sand Ingredient," in *New York Times*, ed. New York, New York, 1954, pp. 1,11.

[6] H. S. Lee, *Thermal design : heat sinks, thermoelectric generators and coolers, heat pipes, and heat exchangers*. Hoboken, NJ: Wiley, 2010.

[7] X. Deng and E. A. Schiff, "Amorphous Silicon-based Solar Cells," in *Handbook of Photovoltaic Science and Engineering*, A. Luque and S. Hegedus, Eds., ed Colchester: John Wiley & Sons, 2003, pp. 505-565.

[8] N. Yastrebova, "High-efficiency multi-junction solar cells:Current status and future potential," ed, 2007.

[9] M. A. Green, "Silicon solar cells: evolution, high-efficiency design and efficiency enhancements," *Semiconductor Science Technology*, vol. 8, pp. 1-12, 1993.

[10] M. A. Green, "Silicon solar cells: evolution, highefficiency design and efficiency enhancements," *Semiconductor Science and Technology*, vol. 8, pp. 1-12, 1992.

[11] J. Lindmayer and J. Allison, "Dotted Contact Fine Geometry Solar Cell," United States Patent, 1975.

[12] M. A. Green, "Crystalline Silicon Solar Cells," *Progress in Photovoltaics Research and Applications*, vol. 12, pp. 1-49, 2001.

[13] J. F. Allison, R. A. Arndt, and A. Meulenberg, "A comparison of the COMSAT violet and non-reflective solar cells," Comsat Tehnical Review, Washington/ DC1975.

[14] J. Lindameyer and J. F. Allison, "The violet cell: an improved silicon solar cell " *Solar Cells*, vol. 29, pp. 151-166, 1990.

[15] M. A. Green. (2009, The Path to 25% Silicon Solar Cell Efficiency: History of Silicon Cell Evolution. *17(3)*, 183-189. Available: http://onlinelibrary.wiley.com/doi/10.1002/pip.892/pdf

[16] M. A. Green, "Characterization of high efficiency silicon solar cells," *Journal of Applied Physics*, vol. 58, pp. 4402-4408, 1985.

[17] J. Zhao, A. Wang, M. A. Green, and F. Ferrazza, "19.8% efficient "honeycomb" textured multicrystalline and 24.4% monocrystalline silicon solar cells," *Journal of Applied Physics Letters*, vol. 73, pp. 1991-1993, 1998.

[18] V. Budhraja, D. Misra, and N. M. Ravindra, "Advancements in PV multicrystalline silicon solar cells from 1980 to 2010- an overview," presented at the 37th Photovoltaic Specialists Conference (PVSC), Golden, CO, 2011.

[19] J. Lindmayer, "Semi-crystalline silicon solar cells," in *Photovoltaic Specialists Conference 12th*, Baton Rouge, LA, 1976, pp. 82-85.
[20] H. Fischer and W. Pschunder, "Low cost solar cells based on large area unconventional silicon " *IEEE Transactions on Electronic Devices,* vol. 24, pp. 438-442, 1977.
[21] S. Narayanan, "17.8 percent efficiency polycrystalline silicon solar cells," *IEEE Transactions on Electronic Devices,* vol. 37, pp. 382-384, 1990.
[22] Z. Chen, "Defect passivation in multicrystalline-Si materials by plasma-enhanced chemical vapor deposition of SiO2/SiN coatings," *Applied Physics Letters,* vol. 65, pp. 2078-2080, 1994.
[23] Z. Chen, "Method for low temperature plasma enhanced chemical vapor deposition (PECVD) of an oxide and nitride antireflection coating on silicon," United States Patent, 1994.
[24] A. Rohatgi, S. Narasimha, S. Kamra, P. Doshi, P. Khattak, K. Emery, *et al.*, "Record High 18.6% efficient solar cell on HEM multicrytalline material," presented at the 25th Photovoltaic Specialists Conference, Washington D.C., 1996.
[25] O. Schultz, S. W. Glunz, and G. P. Willeke, "Multicrystalline Silicon Solar Cells Exceeding 20% Efficiency," *Progress in Photovoltaics,* vol. 12, pp. 553-558, 2004.
[26] T. Mishmia, M. Taguchi, H. Sakata, and E. Maruyama, "Development status of high-efficiency HIT solar cells," *Solar Energy Materials & Solar Cells,* vol. 95, pp. 18-21, 2010.
[27] K. L. Chopra, P. D. Paulson, and V. Dutta, "Thin Film Solar Cells: An Overview," *Progress in Photovoltaics: Research and Applications,* vol. 12, pp. 69-92, 2004.
[28] M. Tanaka, M. Taguchi, T. Matsuyama, T. Sawada, S. Tsuda, S. Nakano, *et al.*, "Development of New a-Si/c-Si Heterojunction Solar Cells: ACJ-HIT (Artificially Constructed Junction-Heterjunction with Intrinsic Thin-Layer)," *Japan Journal of Applied Physics,* vol. 31, pp. 3518-3522, 1992.
[29] H. Kanno, D. Ide, S. Taira, and T. Baba, "Over 22% efficient HIT solar cell," in *23rd European Photovoltaic Solar Energy Conference and Exhibition*, Valenica, Spain, 2008, pp. 1136-1139.
[30] Y. Tsunomura, Y. Yoshimine, M. Taguchi, T. Baba, and H. Kanno, "Twenty-two percent efficiency HIT solar cell," *Solar Energy Materials and Solar Cells,* vol. 93, pp. 670-673, 2009.
[31] A. V. Shah, H. Schade, M. Vanecek, and J. Meier, "Thin-film silicon solar cell technology," *Progress in Photovoltaics: Research and Applications,* vol. 12, pp. 113-142, 2004.
[32] C. R. Wronski, "Amorphous Silicon Technology: Coming of Age," *Solar Energy Materials and Solar Cells,* vol. 41-42, pp. 427-439, 1996.
[33] A. Catalano, "Attainment of 10% conversion efficiency in amorphous silicon solar cells," presented at the Photovoltaic Specialists Conference, San Diego, CA, 1982.
[34] R. Arya, " Superlattice doped layers for amorphous silicon photovoltaic cells," United States Patent, 1988.

[35] J. Yang, "Double-junction amorphous silicon-based solar cells with 11% stable efficiency," *Applied Physics Letters,* vol. 61, pp. 2917-2919, 1992.
[36] J. Yang, "Triple-junction amorphous silicon alloy solar cell with 14.6% initial and 13.0% stable conversion efficiencies," *Applied Physics Letters,* vol. 70, pp. 2975-2977, 1997.
[37] J. Yang, "Status and future perspective of a-Si:H, a-SiGe:H, and nc-Si:H thin film photovoltaic technology," in *Proceedings of the SPIE*, 2009, pp. 74090C-74090C-14.
[38] L. L. Kazmerski, F. R. White, and G. K. Morgan, "Thin-film CuInSe2/CdS Heterojunction Solar Cells," *Applied Physics Letters,* vol. 29, pp. 268-270, 1976.
[39] R. Birkmire and E. Eser, "Polycrystalline Thin Film Solar Cells: Present Status and Future Potential," *Annual Review of Material Science,* vol. 27, pp. 625-653, 1997.
[40] S. Kurtz, D. Myers, W. E. McMahon, J. Geisz, and M. Steiner, "A Comparison of Theoretical Efficiencies of Multi-junction Concentrator Solar Cells " *Progress in Photovoltaics: Research and Applications,* vol. 16, pp. 537-546, 2008.
[41] (27 March). *Section 2.3: Principles of Lasers — Spontaneous Emission, Stimulated Absorption and Emission*. Available: http://www.mrl.columbia.edu/ntm/level2/ch02/html/l2c02s03.html
[42] (27 March). *Cool Roofs and Emissivity*. Available: http://www.energystar.gov/index.cfm?c=roof_prods.pr_roof_emissivity
[43] (27 February). *Radiation Laws*. Available: http://csep10.phys.utk.edu/astr162/lect/light/radiation.html
[44] R. R. King, "40% efficient metamorphic GaInP/GaInAs/Ge multijunction solar cells," vol. Appl. Phys. Lett. 90, 183516 (2007); doi: 10.1063/1.2734507, K. M. E. D. C. Law, C. M. Fetzer, G. S. Kinsey et al., Ed., ed: American Institute of Physics, 2007.
[45] M. W. Wanlass, A. S.P., R. K. Ahrenkiel, D. S. Albin, J. J. Carapella, A. Duda, *et al.*, "Lattice-Mismatched Approaches for High-Performance, III-V Photovoltaic Energy Converters," presented at the IEEE Photovoltaics Specialists Conference and Exhibition, Lake Buena Vista, Florida, 2005.
[46] (2004, 27 February). *Lattice Constants*. Available: http://www.siliconfareast.com/lattice_constants.htm
[47] A. Y. Grama, "Isoefficiency: Measuring the Scalability of Parallel Algorithms and Architectures," vol. 1, A. Gupta, Ed., ed: IEEE, 1993, pp. 12-21.
[48] (27 February). *Isoefficiency Function*. Available: http://www.cse.msstate.edu/~ioana/Courses/CS6163/scalability/sld036.htm
[49] C. Reynolds. (1997, 27 February). *Radiative recombination*. Available: http://www.astro.umd.edu/~chris/publications/thesis/node147.html
[50] S. Sasson. (2007, 27 February). *We Had No Idea*. Available: http://pluggedin.kodak.com/pluggedin/post/?id=687843
[51] J. Perlin, "The Silicon Solar Cell Turns 50," N. R. E. Laboratory, Ed., ed: NREL Report No. BR-520-33947, 2004.
[52] M. F. Tompsett, G. F. Amelio, W. J. Bertram, Jr., R. R. Buckley, W. J. McNamara, J. C. Mikkelsen, Jr., *et al.*, "Charge-coupled imaging devices:

Experimental results," vol. 18, ed. *Electron Devices, IEEE Transactions on*: IEEE, 1971, pp. 992-996.
[53] K. Matsumoto, T. Nakamura, A. Yusa, and S. Nagai, "A New MOS Phototransistor Operating in a Non-Destructive Readout Mode," ed. Japanese Journal of Applied Physics, 1985.
[54] E. R. Fossum, "Active pixel sensors: are CCDs dinosaurs?," vol. 1900, ed. SPIE: spie.org, 1993, pp. 2-14.
[55] C. S. Solanki, *Solar Photovoltaics: Fundamentals, Technologies, and Applications*: Phi Learning Pvt. Ltd., 2009.
[56] R. M. Swanson, "The Promise of Concentrators," *Progress in Photovoltaics: Research and Applications*, pp. 93-111, 2000.
[57] A. Luque and V. M. Andreev. (2007). *Concentrator photovoltaics*.
[58] S. H. Alawaji, "Evaluation of Solar Energy Research and its Applications in Saudi Arabia - 20 Years of Experience," *Renewable and Sustainable Energy Reviews*, pp. 59-77, 2001.
[59] J. M. Gee, "Status of Concentrator Collector and High-Efficiency Concentrator Cell development," *Solar Energy Materials*, pp. 347-355, 1991.
[60] R. McConnell, "Concentrator Photovoltaic Technologies: Review and Market Prospects," *Refocus*, vol. 6, pp. 35-39, 2005.
[61] H. Baig, "Non-uniform Illumination in Concentrating Solar Cells," *Renewable and Sustainable Energy Reviews*, vol. 16, pp. 589-590, 2012.
[62] S. Kurtz and J. Geisz, "Multijunction Solar Cells for Conversion of Concentrated Sunlight to Electricity," *Optical Express*, vol. 18, pp. A73-A78, 2010.
[63] D. Chemisana, M. Ibanez, and J. Barrau, "Comparison of Fresnal Concentrators for Building Integrated Photovoltaics," *Energy Conversion and Management*, pp. 1079-1084, 2009.
[64] W. T. Xie, Y. J. Dai, R. Z. Wang, and K. Sumathy, "Concentrated Solar Energy Applications Using Fresnel Lenses: A Review," *Renewable and Sustainable Energy Reviews*, pp. 2588-2606, 2011.
[65] D. Kruger, Y. Pandian, K. Hennecke, and M. Schmitz, "Parabolic Trough Collector Testing in the Frame of the REACt Project," *Desalination*, pp. 612-618, 2008.
[66] L. Lifang and S. Dubowsky, "A New Design Approach for Solar Concentrating Parabolic Dish Based on Optimized Flexible Petals," *Mechanism and Machine Theory*, vol. 46, pp. 1536-1548, 2011.
[67] W. G. J. H. M. Van Sark, K. W. J. Barnham, L. H. Sloof, A. J. Chatten, A. Buchtemann, A. Meyer, *et al.*, "Luminescent Solar Concentrators - A Review of Recent Results," *Optics Express*, vol. 16, pp. 21773-21792, 2008.
[68] M. J. Moran, H. N. Shapiro, D. D. Boettner, and M. B. Bailey, *Fundamentals of Engineering Thermodynamics*, 7th ed. Hoboken, NJ: John Wiley & Sons, Inc., 2011.
[69] A. Royne, C. Dey, and D. Mills, "Cooling of photovoltaic cells under concentrated illumination: a critical review," *Solar Energy Materials and Solar Cells*, vol. 86, pp. 451-483, APR 1 2005 2005.

[70] K. Araki, H. Uozumi, and M. Yamaguchi, "A Simple Passive Cooling Structure and its Heat Analysis for 500X Concentrator PV Module," in *29th IEEE PVSC*, 2002, pp. 1568-1571.
[71] S. Padovani, A. Del Negro, M. Antonipieri, S. Sinesi, R. Campesato, M. C. Casale, *et al.*, "Triple junction InGaP/InGaAs/Ge solar cells for high concentration photovoltaics application: Degradation tests of solar receivers " *Microelectronics Reliability*, vol. 50, pp. 1894-1898, 2010.
[72] Y. Kemmoku, T. Egami, M. Hiramatsu, Y. Miyazaki, M. Araki, N. J. Ekins-Daukes, *et al.*, "Modelling of Module Temperature of a Concentrator PV System," Ministry of Economy, Trade, and Industry, Japan.
[73] J. J. Wysocki and P. Rappaport, "Effect of Temperature on Photovoltaic Solar Energy Conversion," *Journal of Applied Physics*, vol. 31, pp. 571-578, 1960.
[74] T. Takamotob, T. Aguib, M. Kaneiwab, Y. Uraokaa, and T. Fuyukia, "Annual output estimation of concentrator photovoltaic systems using high-efficiency InGaP/InGaAs/Ge triple-junction solar cells based on experimental solar cell's characteristics and field-test meteorological data," *Solar Energy Materials & Solar Cells*, vol. 90, pp. 57-67, 2006.
[75] H. S. Lee, N. J. Ekins-Daukes, K. Araki, Y. Kemmoku, and M. Yamaguchi, "Field Test and Analysis: The Behavior of 3-J Concentrator Cells Under the Control of Cell Temperature," ed. Nagoya, Japan: Toyota Technological Institute, 2005.
[76] N. Ari and A. Kribus, "Impact of theThomson effect on concentrating photovoltaic cells," *Solar Energy Materials & Solar Cells*, vol. 94, pp. 1421-1425, 2010.
[77] N. Ari and A. Kribus, "Impact of the Peltier effect on concentrating photovoltaic cells," *Solar Energy Materials and Solar Cells*, vol. 94, pp. 2446-2450, 2010.
[78] H. Cotal, R. Sherif, and S. Inc., "Temperature Dependence of the IV Parameters from Triple Junction GaInP/InGaAs/Ge Concentrator Solar Cells " presented at the IEEE 4th World Conference on Photovoltaic Energy Conversion, 2006.
[79] E. Corporation, "CTJ Photovoltaic Cell: Triple-Junction Solar Cell for Terrestrial Applications," ed. Albuquerque, NM: Emcore Corporation, 2008.
[80] "Focal Length," ed.
[81] J. D. Anderson Jr., *Fundamentals of Aerodynamics*. New York: McGraw-Hill, 1991.
[82] B. Thwaites, *Incompressible Aerodynamics: An Account of the Theory and Observation of the Steady Flow of Incompressible Fluid past Aerofoils, Wings, and Other Bodies*. Oxford: The Clarendon Press, 1960.
[83] E. M. Sparrow and J. L. Gregg, "Laminar Free Convection From a Vertical Plate With Uniform Surface Heat Flux," *Transactions of the ASME*, pp. 435-440, 1956.
[84] A. Faghri, Y. Zhang, and J. R. Howell, *Advance Heat and Mass Transfer*. Columbia, MO: Global Digital Press, 2010.
[85] J. P. Holman, *Heat Transfer*, 9th ed.: McGraw-Hill, 2001.
[86] A. Instruments, "Pyranometer Meter MP-100 & 200 Series," ed, 2013.
[87] "Solar Radiation Spectrum," ed.